To Mutsch

Financial support for the publication of this thesis was provided by:
Oldelft Ultrasound
Philips Healthcare
Erasmus Medical Center

Financial support by the Dutch Heart Foundation for the publication of this thesis is gratefully acknowledged.

Cover design by:
Alexander Haak. Heart model was provided by Coert Metz and Nora Baka [91].

Printed by:
Gildeprint, Enschende, Netherlands

ISBN: 978-94-6233-045-0

Augmenting Electrophysiology Interventions with Advanced 3D Transesophageal Echocardiography

Geavanceerde 3D transoesofagale echocardiografie voor betere visualisatie van electrofysiologie-interventies

Proefschrift

ter verkrijging van de graad van doctor aan de
Erasmus Universiteit Rotterdam
op gezag van de rector magnificus

prof.dr. H.A.P. Pols

en volgens het besluit van het College voor Promoties.

De openbare verdediging zal plaatsvinden op
woensdag 2 september 2015 om 11:30 uur

door

Alexander Haak

geboren te Halle (Saale), Duitsland

Erasmus University Rotterdam

Erasmus

Promotiecommissie

Promotor:	Prof. dr. ir. A.F.W. van der Steen
Overige leden:	Prof. dr. ir. N. de Jong Dr. ir. T. van Walsum Prof. dr. J. D'hooge
Copromotor:	Dr. ir. J.G. Bosch

The work in this thesis was conducted at the Department of Biomedical Engineering part of the Thorax Center of the Erasmus Medical Center, Rotterdam The Netherlands.

The publication of this thesis was financially supported by the Dutch Technology Foundation STW (project 10847), which is the applied science division of NWO, and the Technology Programme of the Ministry of Economic Affairs.

Contents

1 Introduction **1**
1.1 The heart . . . 1
1.2 Atrial fibrillation . . . 2
1.3 Challenges in Electrophysiology . . . 4
1.4 Miniaturized Ultrasound . . . 6
1.5 In this Thesis . . . 9

2 Image reconstructions from sparse and irregular sampled 2D transesophageal images **11**
2.1 Introduction . . . 13
2.2 Methodology . . . 14
2.2.1 Creation of 2D Data . . . 14
2.2.2 Reconstruction Filter . . . 16
2.2.3 Error Metric . . . 17
2.2.4 Optimization of NC Kernel Parameter . . . 18
2.3 Results . . . 19
2.4 Discussion . . . 20
2.5 Conclusion . . . 25

3 Segmentation of multiple heart cavities in 3D transesophageal ultrasound images **29**
3.1 Introduction . . . 31
3.2 Methodology . . . 33
3.2.1 Gamma Mixture Model . . . 33
3.2.2 Active shape model . . . 34
3.2.3 Segmentation scheme . . . 37
3.3 Experiments . . . 38

3.3.1 Data . . . 38
3.3.2 Gold standard and Evaluation of Ground Truth . . . 39
3.3.3 Evaluation measures . . . 41
3.4 Results . . . 44
3.5 Discussion . . . 46
3.6 Conclusion . . . 48

4 Fully automatic detection of salient features in 3D transesophageal images 49
4.1 Introduction . . . 51
4.2 Materials and Methods . . . 53
4.3 Results . . . 62
4.4 Discussion . . . 64
4.5 Conclusions . . . 65

5 A transoesophageal echocardiographic image acquisition protocol for wide-view fusion of three-dimensional datasets to support the atrial fibrillation catheter ablation 75
5.1 Introduction . . . 77
5.2 Methods . . . 77
5.3 Results . . . 80
5.4 Discussion . . . 83
5.5 Conclusion . . . 85

6 Fusion of Three-dimensional Transesophageal Echocardiographic Images of Left Atrium for Supporting Catheter Ablation Procedures: Comparison with Computed Tomography 87
6.1 Introduction . . . 89
6.2 Patients and methods . . . 89
6.3 Results . . . 92
6.4 Discussion . . . 92
6.5 Conclusion . . . 100

7 Improved segmentation of multiple cavities of the heart in wide-view 3D transesophageal echocardiograms 101
7.1 Introduction . . . 103
7.2 Materials and Methods . . . 104
7.3 Experiments . . . 111
7.4 Results . . . 112

7.5 Discussion . . . 113
7.6 Conclusions . . . 118

8 Catheter shape estimation using tracked ultrasound imaging and Kalman filters 119
8.1 Introduction . . . 121
8.2 Methods . . . 123
8.2.1 Modelling . . . 123
8.2.2 Unscented Kalman Filter . . . 125
8.2.3 Image Acquisition . . . 129
8.2.4 Catheter Detection in Image . . . 130
8.3 Experiments . . . 130
8.4 Results . . . 133
8.5 Discussion . . . 134
8.6 Conclusion . . . 141

9 Discussion and Conclusion 143
9.1 Discussion . . . 144
9.2 Conclusion . . . 150

Summary 171

Samenvatting 175

Curriculum Vitae 179

Publications 181

PhD Portfolio 185

Acknowledgment 187

Sponsoring 191

Chapter 1

Introduction

1.1 The heart

The heart is a muscular organ which pumps blood through the human body. It consists of four main chambers: the left and right atrium (LA and RA, respectively); and the left and right ventricle (LV and RV, respectively). Low oxygenated blood from the systemic system enters the RA via the superior and inferior *vena cava* and is passed to the RV. The RV contracts and the blood is pumped into the pulmonary circulation while back flow to the RA is prevented by the tricuspid valve (TV). The oxygenated blood returns from the lungs and enters the LA via the pulmonary veins (PV) and passes through the mitral valve (MV) to the LV, which pumps the blood into the systemic circulation via the aortic valve (AV).

Cardiac muscle cells have the unique property of autorhythmicity, which is the ability of spontaneous depolarization. The bulk part of the heart muscle is made up of cardiomyocytes (99%) which easily contract as a response to impulses (action potentials) generated by pacemaker cells. Any disturbance in the electrical activation can lead to a disturbed contraction pattern of the heart, resulting in symptoms ranging from benign up to immediately life threatening conditions.

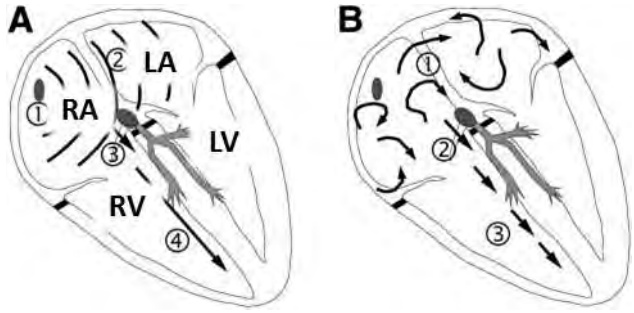

Figure 1.1: Courtesy of Waktare [155], **A**: The left atrium, the right atrium , the left ventricle and the right ventricle are indicated with LA, RA, LV, and RV, respectively. Normal propagation pattern of the electrical activation of the heart muscle. The impulse originates from the SA node (1) and spreads across the atria (2), and via the AV node (3) to the ventricle (4). **B**: In the case of atrial fibrillation chaotic activation cause the atria to beat with 400 to 600 contractions per minute (1). The AV node (2) filters out most of the high frequency signals but nevertheless these signals may cause elevated ventricular heart rates (3).

1.2 Atrial fibrillation

Background

Waktare's patient page for atrial fibrillation from 2002 starts with *"Atrial fibrillation (AF) is the most common heart rhythm disturbance in the United States affecting over 2 million individuals"*[155]. Approximately, 4 % of the population over 65 years are affected by AF and this will increase to about 11 % of the people over 80 years old [131]. Therefore, AF becomes a more and more challenging disease for our health care system especially for the western world with their aging population.

Normal heart beat and atrial fibrillation

Normally, the heart beat is initiated by the sinoatrial (SA) node and the electrical activation spreads over the atria causing the contraction of the atria in a specific pattern [155]. The ventricles are electrical isolated from the atria by the valve plane which consists mostly of fibrous tissue. The electrical activa-

tion then travels via the atrioventricular (AV) node (which has some filtering characteristic) and the Purkinje system to the apex of the ventricles (see Fig. 1.1-**A**).

AF is defined by an irregular and rapid contraction of the atria with rates up to 400 to 600 contractions per minute [155]. The AV node filters most of the extra signals but some still propagate to the ventricles causing the heart rate to rise [155] (see Fig. 1.1-**B**). The causes of AF are not fully understood yet and still under investigation [131]. In some cases, AF might be due to wandering, disorganized electrical waves that circulate through the atria [131]. In other cases, AF may be triggered by single rapidly firing electrical sources which are quite often in one of the pulmonary veins (PV) [131]. This irregular heartbeat can be diagnosed by checking the patient's pulse or with an electrocardiogram (ECG).

Symptoms and treatment options

Symptoms vary between patients and can range from fatigue, difficulty breathing, shortness of breath, palpitations, irregular heart beat, chest pain up to heart failure [131]. Some patients are immediately aware of these fibrillations, while others are unaware of the change in their heart's rhythm. Although AF is not directly life threatening, it has been shown that there is an increased risk of stroke and heart failure associated with it [131].

There is a wide clinical spectrum of AF ranging from *paroxysmal* AF, *persistent* AF, to *permanent* AF [155]. In paroxysmal AF, episodes can last anywhere from seconds to days but the heart switches back spontaneously to sinus rhythm. On the contrary, persistent AF does not stop spontaneously and can only be restored by medical intervention in the form of medication or cardio-version. Hearts with permanent AF are always in fibrillation and restoration of sinus rhythm is not possible.

Three common pharmacological options are available for treating AF [155, 3, 131]. Most patients are on anticoagulation to reduce the risk of stroke due to blood clots formed in the atria. Depending on the type of AF, heart rate control medication is given to reduce the ventricular heart rate to an acceptable level. Also, antiarrhythmic drugs are used to stabilize the electrical activation pattern in the heart.

Another way of stopping erroneous activation in the atria is the Cox-Maze-III procedure [31]. The idea behind this open heart surgery is to compartmentalize the atrium through incisions to generate scar tissue which will electrically isolate certain areas of the atrium and therefore stop erroneous activation. This pro-

cedure has been found quite effective in curing AF with success rates above 90 % but it is quite risky and invasive and therefore not suitable for a large group of patients [115]. However, over the last 25 years minimal invasive catheter ablations have emerged which are nowadays commonly used to treat AF.

1.3 Challenges in Electrophysiology

Current Status

Developments in Electrophysiology (EP) over the last 25 years led to the treatment of AF in a minimally invasive catheter-based way which makes it suitable for a larger group of patients. Erroneous activation of the atria is stopped by creating lesions with ablation catheters (usually RF-ablation). Procedures can be done with the patient sedated or under general anaesthesia [3]. Catheters are usually inserted via the groin and *vena cava* into the right atrium and via a septal puncture into the left atrium where most of the ablations are done [3]. Catheters are observed on X-ray fluoroscopy [3, 133] and lately also intra cardiac echo is used for guidance[62, 121]. Electrical activation pattern within the atria are mapped by measuring the ECG on many positions at the atrial wall with special catheters creating a so-called electro-anatomical map (EAM) [133, 47] (see Fig. 1.2). The 3D position of the catheter tip is estimated using electromagnetic or resistance based tracking systems. For better visualization of the anatomy the EAM can be registered to segmentations of the patient's heart generated from magnetic resonance imaging (MRI) or computed tomography angiography (CTA) [48] (see Fig. 1.2b). Such a 3D map can also be projected on the 2D x-ray image. This is especially important when ablating the PVs since their anatomy is quite variable [108, 107]. When erroneous activation sites are identified from the EAM or local catheter measurements, these can be isolated by creating ablation lesions in spot or line like fashion. Those procedures are complex and very lengthy, taking usually about 3 to 6 hours. However, despite the efforts already put into providing a better visualization of the catheters by augmented reality techniques, there are still quite some shortcomings due to the sparse sampling of the EAM and the possible anatomical changes at the time of the intervention. Furthermore, the CTA/MRI image acquisition is usually done weeks in advance. This may further lead to decreased precision because of changes in physiological state.

Catheter ablations are complex and long procedures and currently success rates are only modest and quite variable between patients and hospitals [155].

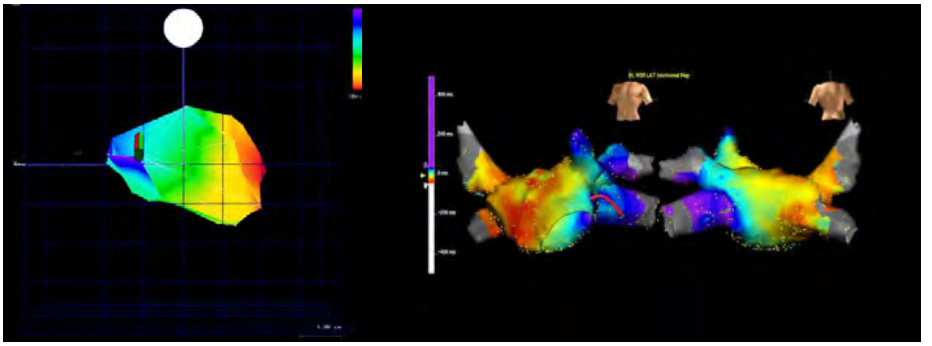

(a) (b)

Figure 1.2: **1.2a**, electro-anatomical map (EAM) of a porcine left ventricle (courtesy of L. Gepstein *et al.* [47].) **1.2b**: EAM registered to a CT derived segmentation (Courtesy of St. Jude Medical [1]). Color represents arrival time of electrical activation.

A more invasive and risky procedure such as COX-Maze-III has better long term success rates than AV ablations. Cox-Maze-III is successful in 90% of the patients while EP ablations are reported to have very variable success [24]. In a recent big meta-study [17] were found to be successful in 11% up to about 74% of single interventions. When multiple interventions and antiarrhythmic drugs post intervention were used 28% up to 94% of the patients were reported to remain AF free. This included different intervention techniques [24, 17].

Improving EP

Improving efficacy, reducing costs, and understanding the underlying physiological mechanism of AF are the main challenges EP is currently facing. There are several points of attack to improve EP from an biomedical engineering point of view.

- **Improve Outcome:** Raise the success rate to similar values than Cox-Maze-III (e.g. around 90%) and reduce the number of necessary redo procedures.
- **Reduce dependence on operator skills:** There is quite a large variance in the outcome of AF ablation between centers and patients. This

suggests also that the outcome highly depends on operator skills. A better visualization may improve outcome and reduces the demands on operator skills.

- **Shorter procedure times:** Patient throughput can be increased by shorter procedure times per patient. Shorter procedure times will also reduce the radiation exposure of patients and personnel.

- **Lower costs:** Cost will be reduced if less procedures per patient are needed. Also, the number of single use devices and the number of preoperative images can be reduced.

Solution by intraoperative 3D imaging

One possible solution for improving on some of the above mentioned points would be a better 3D visualization of the catheters in the anatomical context during the intervention so that navigation and control is improved. This would require an intra-operative 3D imaging modality which is able to visualize catheter and soft tissue. Furthermore, showing a surface model of the patient's heart anatomy and visualizing the current catheter position relative to it may be of great help for the physician. This augmented reality of the heart and especially of the atria and the catheters might be advantageous in patients with abnormal anatomy and may also be less demanding on the operator skill. Furthermore, lower x-ray exposure and simplified logistics through lesser use of preoperative imaging may be desirable.

1.4 Miniaturized Ultrasound

Ultrasound Imaging

The development of medical ultrasound (US) imaging started after world war II inspired by developments in radar (RAdio Detection And Ranging) and sonar systems [25]. Range imaging is the underlying image formation principle. Usually, in medical applications an acoustic pulse is generated by a transducer and propagates through the body with a speed of sound of about 1540 m/s. Sound is reflected at density and compressibility changes in the medium which can be caused macroscopic structures such as tissue boundaries as well as micro structures within the tissue and even on a cellular level (scattering). The reflected sound (echo) is received, usually with the same transducer which generated

the excitation pulse, and commonly the echo amplitude is detected and can be displayed on a screen (A-line). The time an echo was received corresponds to the depth of the corresponding structure. A 2D image (B-mode imaging) is constructed by either mechanically or electronically steering the US beam and successively constructing the image from several A-lines, where the echo amplitude is displayed as a brightness image. The interference of scattered echo generates the typical speckle patterns in US images.

Transesophageal Echocardiography

Ultrasound imaging is the image modality which was developed partly by the demands of cardiology to be able to image the beating heart. The first transthoracic echocardiograms (TTE) with an electronically translated US beam were acquired by Bom et al. [13]. Nowadays, transesophageal echocardiography (TEE) probes are available which allow a view of the heart from the esophagus, less compromised by artifacts due to the lungs and the rib cage. Before and during EP interventions TEE imaging is used to diagnose blood clots which may have formed in the atrium. Since the last 15 years three-dimensional (3D) echo is available in cardiology (see Fig. 1.3b). It is intensively used and in many applications superior to two-dimensional (2D) echo. A few years ago a miniaturized TEE (μTEE) probe (MicroMulti TEE, Oldelft Ultrasound, The Netherlands) was introduced mainly for neonatal and pediatric applications. Because of its small size, it can also be very useful in adults for monitoring minimally-invasive interventions. A transnasal introduction of the probe has been shown and it was reported that patients could tolerate the probe for up to 24 hours [160, 137]. The probe has a 32 element phased array generating a 2D image with an opening angle of about 90 degrees. The image plane can be rotated by 180 degrees, covering a conical volume (see Fig. 1.3). Scanning such a volume by rotating the array while acquiring 2D images and the ECG signal makes reconstruction of the beating heart in 3D possible [153]. These 4D reconstructions and also the set of individual 2D images could be a means of imaging the beating heart and the catheters in an EP intervention situation.

4D Image reconstruction from 2D images

Typically, during such an rotational acquisition the image plane is rotated manually and the imaging is not triggered or synchronized to the heart beat. Therefore, the 2D image set is irregularly and sparsely sampled in the time domain (cardiac phase) and the spatial domain (rotation angle of the image plane).

Standard interpolation schemes like nearest neighbor and linear interpolation do not perform well on this type of data.

Heart Segmentation

The atrial anatomy such as the pulmonary veins, the atrial appendages, and the atrial septum are of importance for AF ablations. It has been shown that these landmarks can be visualized with 3D TEE [41]. However, the anatomy of interest is quite variable between patients and important landmarks such as the pulmonary veins may not always be visible. Secondly, the atria are in the near field of the TEE probe and especially the left atrium is impossible to image entirely with a single 3D view. Image fusion of several views covering the whole LA can be used to create a panoramic wide view. This wide view image can then be used to segment the LA.

Segmentation involves separating different structures in the image (e.g. blood pool and myocardial tissue) while constraining the surface of the organ with some type of model. In our case we want to separate the surfaces of LA, LV and other cavities from the blood pool. This generates a surface model of the patient's heart which can provide the anatomical context necessary for AF ablations. This could replace the preoperative CT-derived segmentations and can be combined with the EAM.

Segmentation can be done based on image intensities (blood is dark and tissue is brighter in US images) but also on US speckle characteristics. The scattering of US depends highly on the frequency of the used pulse and the size, shape, and spatial distribution of the scatterers. The interference of the scattered echos creates a specific speckle pattern which can be used to estimate tissue characteristics and segment organs [154, 87].

Segmentation in the wide-view image will be easier since most of the organ is captured. However, while ablating it is necessary to concentrate the imaging on the ablation area only and not the entire atrium. This necessitates that the anatomical model can also be fitted to a partial view of the LA.

Catheter Tracking

The position and orientation of the catheters used during the AF ablation procedure relative to the anatomy of the atria is important for successful ablations and the currently used electromagnetic and resistance based tracking methods are not always accurate enough. The catheter position, orientation and shape can be estimated more accurately using the ultrasound images, the information

derived from the tracking data generated from the used AF ablation equipment, and a catheter model.

1.5 In this Thesis

To show that μTEE imaging combined with advanced image processing could be used to help the outcome of AF ablation procedures is the objective of this thesis. First, we evaluate the quality of 4D reconstructions generated using an interpolation method, called normalized convolution (NC), which is suitable for irregular and sparsely sampled data such as the data we expect from the μTEE probe. In chapter 2 the work concerning reconstructing images from μTEE data acquired in an irregular and sparse fashion is presented.

Secondly, we evaluate if (or to what extend) the LA can be entirely imaged by a wide view image fusion and if all important anatomical features of the LA can be captured. In chapter 5 and 6 we investigate the possibility of imaging the LA with wide-view image-fusion and if anatomical landmarks can be identified reliably.

Thirdly, we investigate how 3D TEE data can be used for multi-cavity image segmentation and to what extend the partial field of view (FoV) will affect segmentation quality. The possibility of accurate image segmentation from partial and wide-view 3D TEE data is presented in chapter 3 and 7. We developed an automatic landmark detection scheme for TEE images which we use for model initialization which we present in chapter 4.

Fourthly, we look into how catheter shape and location could be estimated from tracked ultrasound images combined with a catheter model. Our work on catheter tracking is described in chapter 8.

In chapter 9 we discuss our findings and future work.

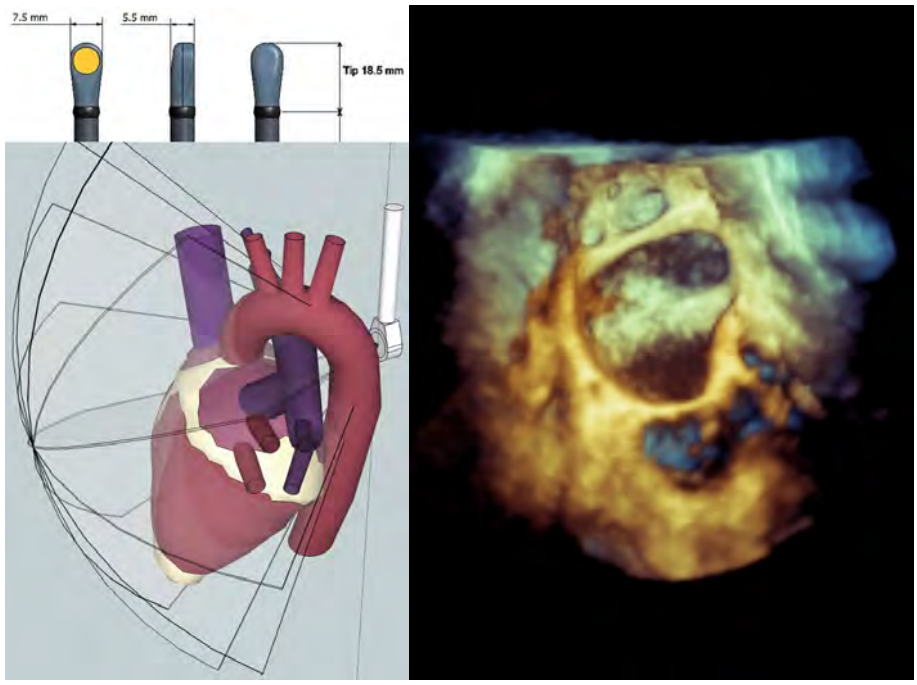

(a) (b)

Figure 1.3: **1.3a**, Dimension of the μTEE probe tip (courtesy of Oldelft Ultrasound, Netherlands) and the conical volume that can be scanned by rotating the 2D image plane by 180 degrees. **1.3b:** An example 3D rendering of a 3D TEE probe. The anatomy of the left atrium with the mitral valve, atrial appendage, and the left pulmonary veins are visible.

Chapter 2

Image reconstructions from sparse and irregular sampled 2D transesophageal images

This chapter has been compiled from:
A. Haak, M. van Stralen, G. van Burken, S. Klein, J. P. W. Pluim, N. de Jong, A. F. W. van der Steen, J. G. Bosch, Comparison of spatiotemporal interpolators for 4D image reconstruction from 2D transesophageal ultrasound, *Proc SPIE Med Imaging*, Vol. 8320, pp. 832007-832007-11 (2012).
and
A. Haak, S. Klein, M. van Stralen, G. van Burken, J. P. W. Pluim, N. de Jong, A.F.W. van der Steen, J.G. Bosch, Optimal kernel sizes for 4D image reconstruction using normalized convolution from sparse fast-rotating transesophageal 2D ultrasound images, *Proc. Ultrasonic Symposium (IUS)*, pp. 703-706, (2012).

Abstract
For electrophysiology intervention monitoring, we intend to reconstruct 4D ultrasound (US) of structures in the beating heart from 2D transesophageal US by scanplane rotation. The image acquisition is continuous but unsynchronized to the heart rate, which results in a sparsely and irregularly sampled dataset and a spatiotemporal interpolation method is desired. Previously, we showed the potential of normalized convolution (NC) for interpolating such datasets. We explored 4D interpolation by 3 different methods: NC, nearest neighbor (NN), and temporal binning followed by linear interpolation (LTB). The test datasets were derived by slicing three 4D echocardiography datasets at random rotation angles (θ, range: 0-180°) and random normalized cardiac phase (τ, range: 0-1). Four different distributions of rotated 2D images with 600, 900, 1350, and 1800 2D input images were created from all TEE sets. A 2D Gaussian kernel was used for NC and optimal kernel sizes (σ_θ and σ_τ) were found by performing an exhaustive search. The RMS gray value error (RMSE) of the reconstructed images was computed for all interpolation methods. The estimated optimal kernels were in the range of σ_θ = 3.24 - 3.69°/ σ_τ = 0.045 - 0.048, σ_θ = 2.79°/ σ_τ = 0.031 - 0.038, σ_θ = 2.34°/ σ_τ = 0.023 - 0.026, and σ_θ = 1.89°/ σ_τ = 0.021 - 0.023 for 600, 900, 1350, and 1800 input images respectively. We showed that NC outperforms NN and LTB. For a small number of input images the advantage of NC is more pronounced.

2.1 Introduction

The focus in cardiology is increasingly shifting towards heart rhythm disorders (arrhythmias) such as atrial fibrillations (AF). Arrhythmias are caused by abnormalities in the electrical signal conduction and activation of the heart. Approximately one third of arrhythmias concern AF [122] making it the most common cardiac arrhythmia [43, 49]. AF causes a reduced contraction of the atria, irregular conduction of impulses to the ventricle, and irregular heart beats. The presence of AF is associated with an increased mortality and a higher risk of stroke due to thrombo-embolism, heart failure, and impaired cognitive function [43, 49, 58, 23, 122].

Electrophysiology (EP) interventions are used to treat a range of arrhythmias by ablating tissue in specific parts of the heart such as the areas around the pulmonary veins in the left atrium [23]. The ablation region can vary from simple points to complex geometries such as lines and circles (e.g. the modified Cox maze procedure)[23]. Typically, the pulmonary veins (PV) are isolated and the atrial surface divided into several regions by creation of a series of ablation lesions (1-2mm apart), forming continuous lines. The isolation may fail if the lines are not continuous. The creation of these 3D lesions is further complicated by the motion of the atrial wall due to the heartbeat and breathing. Direct 3D imaging of the anatomical structure and the ablation catheters would be of great help. Currently, X-ray fluoroscopy is mostly used for ablation catheter guidance, which delivers naturally only 2D images, has a weak blood-tissue contrast, and exposes the patient and medical personnel to harmful ionizing radiation.

Transesophageal echocardiography (TEE) is an excellent method to visualize the anatomical structure of the heart in 3D. Preliminary studies showed a good contrast of the ablation catheters in the ultrasound images. However, the current 3D TEE probes, are relatively large and cannot remain for a long time in the patient (see left of Fig. 2.1-A). A newly developed transnasal TEE probe (MicroMulti TEE, Oldelft Ultrasound, The Netherlands) with a tip size of $7.5\times5.5\times18.5$ mm is well tolerated by the patient and studies showed that the probe can remain in the body for up to 24 hours [160, 137]. A comparison of the MicroMultiTEE (microTEE) probe and a conventional 4D matrixTEE (X7-2t, Philips Healthcare, The Netherlands) probe is given in Fig. 2.1-A. The microTEE probe consists of a 32 element phased array that delivers 2D ultrasound images. The array can be internally rotated over 180°. Therefore, 4D (3D+time) images can be obtained by stepwise rotation of the image plane and acquiring a full heart beat for each rotation step (see Fig. 2.1). The 4D image is reconstructed by interpolating the acquired 2D images. This type of image acquisition will be rather slow. Another approach is fast rotation of the phased array while continuously acquiring 2D images [153]. This leads to fast image acquisition but results in a sparse and irregularly sampled set (see Fig. 2.3-B) and advanced reconstruction methods are necessary.

We showed in previous work [14, 98] that normalized convolution (NC) is well

suited for interpolating such sparse and irregularly sampled data. The quality of the reconstructed image depends on the chosen convolution kernel and its parameters. Narrower kernels may be beneficial in densely sampled regions whereas wider kernels may have advantages in sparsely sampled regions. An example of different sizes of a 2D Gaussian kernel is given in Fig. 2.2. The convolution kernel, depending on its size, alters (blurs) the image contents such as edges or image details like valves. Therefore, it can be assumed that there exists an optimal kernel size which will create an reconstructed image with the least deviation from a 'true' image. This kernel comprises the best compromise between smoothing and preserving edges.

We previously introduced a method to simulate the microTEE data acquisition and established a realistic ground truth for optimizing NC kernel sizes [51]. This method uses conventional 4D TEE cardiograms, acquired using a matrix TEE probe, as a ground truth. Rotated 2D images sampled at a random angle and frame time were obtained from the 4D TEE set. These 2D images were used to reconstruct a 4D image by NC. The quality of the reconstructions was assessed by computing the error with the original 4D TEE set. In this work we evaluate:

- If NC reconstructions are superior to other interpolation methods such as nearest neighbor (NN) and linear interpolation with temporal binning (LTB).
- If NC kernel can be optimized using a exhaustive search scheme and a quasi Newton optimizer.
- If optimal kernel parameters can be reliably modeled and by how much NC reconstructions fall back if they used model kernel compared to optimal kernels.

We tested the method on five different matrix TEE data sets acquired from different patients. We ran reconstructions on a number of different sizes of input data ranging from 400 to 1800 2D images.

2.2 Methodology

All image processing tasks were realized in C++ using the ITK [158] toolbox.

2.2.1 Creation of 2D Data

The 2D input images for the reconstruction filter (see figure 2.4) were derived from five 4D (3D+time) matrixTEE data sets (224×208×208 voxel, 26 to 42 time frames) which contained one complete cardiac cycle. The different 4D TEE sets were obtained from different patients, containing similar views covering most parts of the left atrium, the mitral valve, and the basal part of the left ventricle. TEE acquisitions with a low image quality were excluded from analysis. The matrixTEE sets were smoothed in the spatial dimensions by convolution with a Gaussian kernel (variance = 3 voxel) and afterwards downsampled to 108×100×100 voxel with an isotropic voxel size of

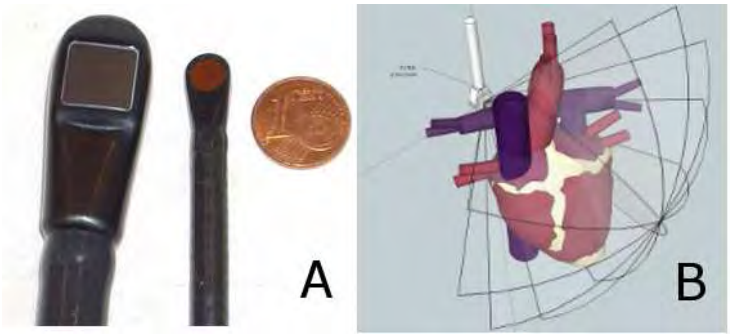

Figure 2.1: Comparison of the matrixTEE (A, left) and the microTEE (A, right) probe heads. The rotated scan planes, which can be obtained with the microTEE probe, are illustrated in B.

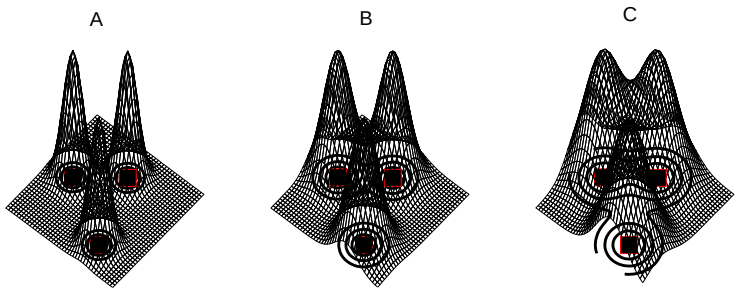

Figure 2.2: Schematic example of interpolating three data points (indicated by squares) with 2D Gaussian kernels. The kernel used in B has a 50 % larger width than the kernel used in A. C shows a kernel which has twice the width of the kernel used in A. It can be appreciated that wider kernels lead to more overlap between given sample points.

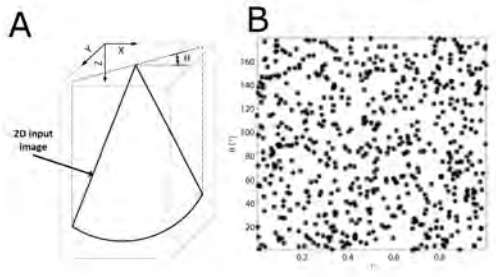

Figure 2.3: Location of a rotated 2D input image within a reconstructed 3D time frame (A). An schematic example of an 2D input image data distribution in the $\theta\tau$-space (B).

Figure 2.4: The 4D image reconstruction scheme. The input 2D image set with angle and cardiac phase information is fed into the reconstruction filter which creates a series of 3D time frames by using either normalized convolution (NC), nearest neighbor (NN) or linear interpolation with temporal binning (LTB).

1.25 mm to decrease computational demands. Data sets with a varying number (N) of rotated 2D image slices (I_{2D}) were taken from the smoothed 4D data sets at a random rotation angle ($\theta \in [0.0, ..., 180.0)$) and a random normalized cardiac phase (time frame). An example of a rotated 2D image within a 3D time frame is given in Fig. 2.3-A. The off-grid points of the rotated 2D images were determined using nearest neighbor interpolation. The rotation axis was parallel to the z-axis and at the center of the xy-image plane. Sets of 2D input images were created from all three 4D TEE data sets containing a different number of 2D images (400, 600, 900, 1350, and 1800).

2.2.2 Reconstruction Filter

We used three different interpolation methods for the reconstruction filter (middle block of Fig. 2.4) to create a series of 3D time frames with a spatial dimension of 108×100×100 voxel. The reconstructions had half of the temporal resolution than the original 4D TEE images. The reconstruction filter used NC, NN, and LTB as interpolators which will be explained in the following sections.

4D Data reconstruction using Normalized Convolution

The NC algorithm[75, 14] and the implementation[51] used in this work, are described elsewhere. However, for completeness we would like to give a small review of the NC algorithm.

A time series of 3D images was reconstructed by interpolating in the spatiotemporal $\theta\tau$-space utilizing NC [14]. The image intensity of the reconstructed image, I_{NC}, in

cylindrical coordinates using NC is given by

$$I_{NC}(\theta, r, z, \tau) = \frac{(I_{2D}(r, z)\, C * G)(\theta, \tau)}{(C * G)(\theta, \tau)}, \tag{2.1}$$

where C is the certainty map of the sampled data, and G is the interpolation kernel. The $*$ denotes the convolution operation. Note that the interpolation is only done in the spatiotemporal $\theta\tau$-space since r and z are fully sampled. We set the certainty map to one at the input image (I_{2D}) location and zero elsewhere (see Fig. 2.3-B). Therefore, we can parameterize the $\theta\tau$-space over the input images which gives for I_{NC} at the query point $q(\theta_q, r, z, \tau_q)$ (see Fig. 2.5)

$$I_{NC}(\theta_q, r, z, \tau_q) = \frac{\sum_{n=0}^{N-1} I_{2D}(\theta_n, r, z, \tau_n) G\big(\theta_n - \theta_q, \tau_n - \tau_q\big)}{\sum_{n=0}^{N-1} G\big(\theta_n - \theta_q, \tau_n - \tau_q\big)}. \tag{2.2}$$

A 2D Gaussian function was used as interpolation kernel (equation 2.3).

$$G(\theta, \tau) = \exp\left[-\left(\frac{\theta}{\sigma_\theta}\right)^2 - \left(\frac{\tau}{\sigma_\tau}\right)^2\right] \tag{2.3}$$

The width of the Gaussian kernel is defined by the two parameters σ_θ and σ_τ which can be optimized to obtain best possible reconstructions (see section 2.2.3).

Nearest Neighbor Reconstruction

NC was compared to a nearest neighbor (NN) interpolation which was also performed in the $\theta\tau$-space. The approximate nearest neighbor library was used [6]. The neighbor with the minimum normalized squared Euclidean distance $min_{\forall n \in N}\left((d\theta_n/180^\circ)^2 + d\tau_n^2\right)$ is used to assign an intensity value to a voxel in the reconstructed image.

Linear Interpolation with Temporal Binning

For the LTB interpolation scheme 2D images were first temporally sorted into bins with a size of two frame periods which results into 15 time frames. Afterwards from each time bin a time frame was reconstructed by linear interpolation of the two nearest neighbors in the angular θ-dimension only. This results in a 4D image.

2.2.3 Error Metric

The NC kernel parameters σ_θ and σ_τ (see equation 2.3) were optimized in order to obtain optimal NC reconstructions. We used the root mean squared error as a metric

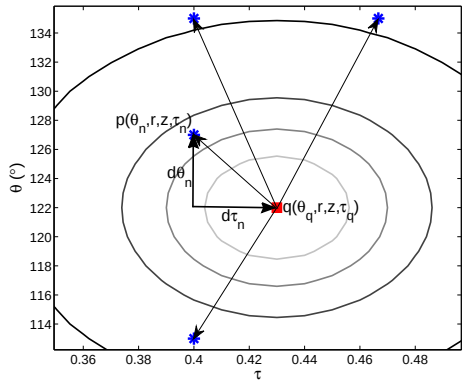

Figure 2.5: Exemplary sketch of a query point $(q(\theta_q, r, z, \tau_q))$ in the $\theta\tau$-plane. The neighboring 2D images are indicated by blue asterisks. The certainty map C is one at the 2D image locations and zero elsewhere. The contour of the Gaussian interpolation kernel is depicted by the concentric rings around the query point.

to judge the similarity of the reconstructed image (I_{recon}) and the ground truth image (I_{GT}). The RMSE was defined as

$$RMSE = \sqrt{\frac{1}{N_{voxel}} \sum_{n=0}^{N_{voxel}-1} \left(I_{recon}[n] - I_{GT}[n]\right)^2}, \tag{2.4}$$

where N_{voxel} represents the total number of voxels for one 4D image. We also used the RMSE to compare the different interpolation methods. Figure 2.6 gives an overview of how the RMSE was computed.

2.2.4 Optimization of NC Kernel Parameter

We used an exhaustive search and a quasi-Newton (QN) optimizer [83, 74] to find the optimal kernel parameters for NC. First we ran an exhaustive search on a sub data set of three 4D TEE images (TEE I, II, III) from the same patient to validate the convexity and smoothness of the RMSE and to validate the QN optimizer. Depending on the number of 2D input images we used different limits for the exhaustive search space. These limits are shown in Table 2.1. The faster QN optimizer was used on the full five patient data set to find optimal kernel parameters.

Table 2.1: Limits of exhaustive search

num. of 2D images	600	900	1350	1800
σ_τ	0.0005-0.073	0.0005-0.048	0.0005-0.048	0.0005-0.048
number of steps σ_τ	30	20	20	20
σ_θ	0.09°-8.64°	0.09°-8.64°	0.09°-8.64°	0.09°-8.64°
number of steps σ_θ	20	20	20	20

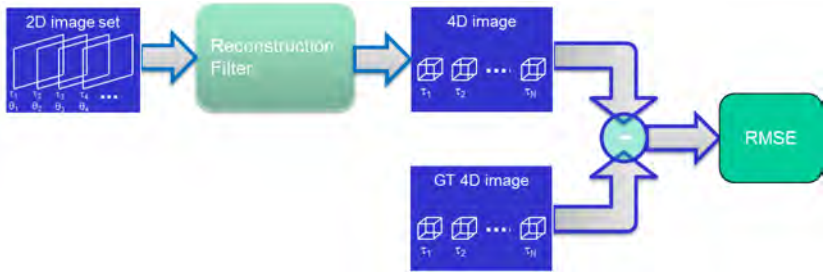

Figure 2.6: Overview of computing the root mean square error (RMSE) metric for the reconstructed images.

2.3 Results

A qualitative example of one 3D time frame of the TEE II set and all tested reconstructions (NC, NN, LTB) computed from 600 2D input images is shown in Fig. 2.7. The RMSE for the different TEE sets for optimized NC, NN, and LTB is shown in Fig. 2.8 and in table 2.3, 2.4, 2.5 for the sub data sets. For the sub data sets (TEE I, II, III) the NC kernels were optimized utilizing a exhaustive search. The RMSE with respect to the parameter space is shown in Fig. 2.9. Note that the minimum RMSE is indicated by the magenta squares and that the RMSE is smooth and convex. In Fig. 2.10 some example QN optimizations are overlaid with the exhaustive search results. Note that the QN optimization converges within 9±3 iterations to the minimum (magenta square) of the cost function which is a significant speed up of the optimization. The QN optimization was then employed to all five TEE data sets. The average optimal kernel sizes σ_θ and σ_τ of the whole test data sets as a function of the number of input images (n) are given in Fig. 2.11. The bars indicate the standard deviations. The dashed lines represent a power law fit of the form $y(n) = Cn^\alpha$. The model parameters are given in Fig. 2.11 as well. The average NC reconstruction errors using optimal and model kernels are shown in Fig. 2.12. Note the similar performance between optimal and model derived NC reconstruction kernels. The average difference

in the error between reconstructions using model kernels and optimal kernels is shown in Fig. 2.13.

2.4 Discussion

Fig. 2.8 shows the obtained average RMSE for the tested reconstruction methods (NC, NN, LTB) for the sub data sets. It can be seen that NC has for all sub sets the lowest RMSE compared to NN and LTB.

In order to assess the temporal consistency of the reconstructed images, we computed the standard deviation of the individual RMSE obtained for each 3D time frame of the sub data set (see Tab. 2.3, 2.4, 2.5). When looking at the standard deviation of the RMSE it can be seen that for the densely sampled data sets (1350 and 1800) NC has the lowest standard deviation of the RMSE (stdRMSE). It is also apparent that the stdRMSE is highest and relative constant for LTB for all cases.

Table 2.2: Mean intensity ± standard deviation of the TEE images

	TEE I	TEE II	TEE III
mean Intensity±std	77.07±52.83	46.10±56.74	32.37±44.68

When looking at Fig. 2.8 or Tab. 2.3, 2.4, 2.5 it can be seen that the RMSE is highest for all reconstructions of TEE I and decreases successively for TEE II and TEE III. This may be explained by looking at the mean intensities of the different TEE images (see Tab. 2.2). The TEE I image has the highest mean intensity followed by TEE II and TEE III images. If there is a similar artifact in the reconstructions, this will result in a higher RMSE for TEE I image compared to TEE II and III images. Also note that the relative performance of the interpolators is the same for all TEE images.

The LTB reconstructions have a consistent high RMSE which indicates, that the temporal binning leads to more temporal image artifacts than NN or NC. However, for the sparsely sampled sets (with 600 input images), LTB has a lower RMSE than NN, which can also be qualitatively observed in Fig. 2.7. The NN reconstruction shows blocky artifacts which are not present in the NC and LTB reconstructions. If the number of 2D images is raised these artifacts of the NN reconstruction were less pronounced which is also indicated by the lower RMSE for sets with 1350 and 1800 input images (see Tab. 2.3, 2.4, and 2.5).

From Fig. 2.9 it can be seen that the RMSE metric is smooth, convex and has a distinct minimum for all tested TEE images. For a higher number of 2D images (1350, 1800) the cost function becomes steeper (see Fig. 2.9). The RMSE for the optimal NC reconstruction is the highest for the sparsely sampled sets with 600 2D images and decreases successively for sets with 900, 1350 and 1800 input images. This is expected

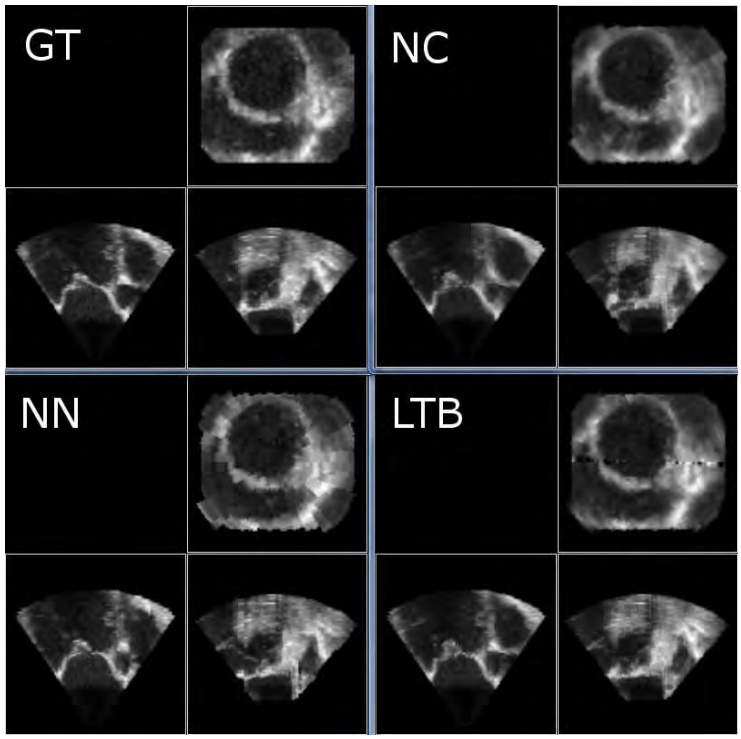

Figure 2.7: Qualitative example of a 3D time frame of the original TEE II image (GT, upper left quadrant) and the reconstructions using NC with optimized kernel parameters, (upper right), nearest neighbor (NN, bottom left), and linear interpolation wit temporal binning (LTB, bottom right). Each quadrant shows three orthogonal views through the 3D images at identical positions.

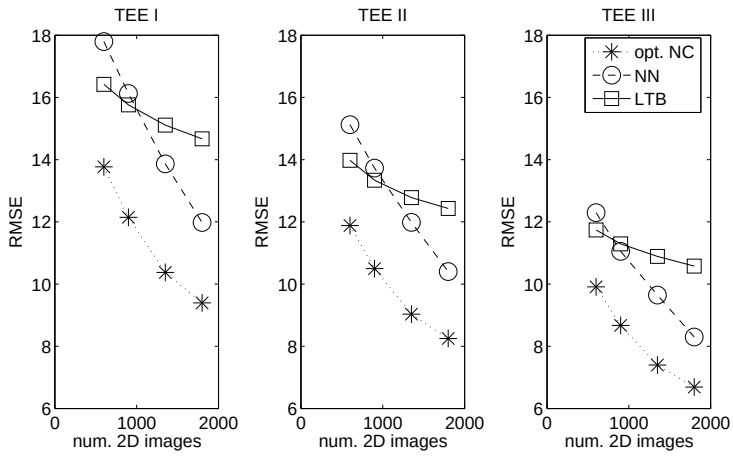

Figure 2.8: RMSE for the different interpolators (NC, NN, LTB) for the three different sub TEE datasets.

since firstly, for a denser sampled sets more original 2D data is available and secondly narrower kernels were found which preserve more image detail. This can also be seen by the decreasing kernel sizes found for the different sets (see Fig. 2.8).

Another important observation is that the kernel sizes do not seem to depend on the chosen TEE image but rather on the number of input images (see Fig. 2.11)

The RMSE for reconstructions using NC kernel sizes predicted by the model is only marginally higher than the RMSE for reconstructions using optimal kernels (Fig. 2.12 and 2.13). Images reconstructed from 400 2D images had the highest increase in RMSE when model NC kernel sizes were used (Fig. 2.13). We believe this is due to a higher spread in the optimal kernel sizes when 400 2D input images were used (see Fig. 2.12). Due to the 'extreme' sparse sampling the optimal kernel size may be more dictated by noise resulting in a more random location of the optima. Therefore, the model kernel sizes do not predict well the individual optima of the different patients. The increasing difference in RMSE between model and optimal kernel sizes for 1350 and 1800 2D input images may be due to the steeper error metric around the optimum (see Fig. 2.9). Small deviations from the optimum will result into a higher RMSE than for reconstructions using 600 or 900 2D input images.

The fitted power law function correlates well with the optimal NC kernel sizes (R=0.88 and R=0.91 for σ_θ and σ_τ respectively).

The QN-optimizer converges on average within 10 iterations which corresponds to 40 image reconstructions since we used a finite difference to compute the gradient

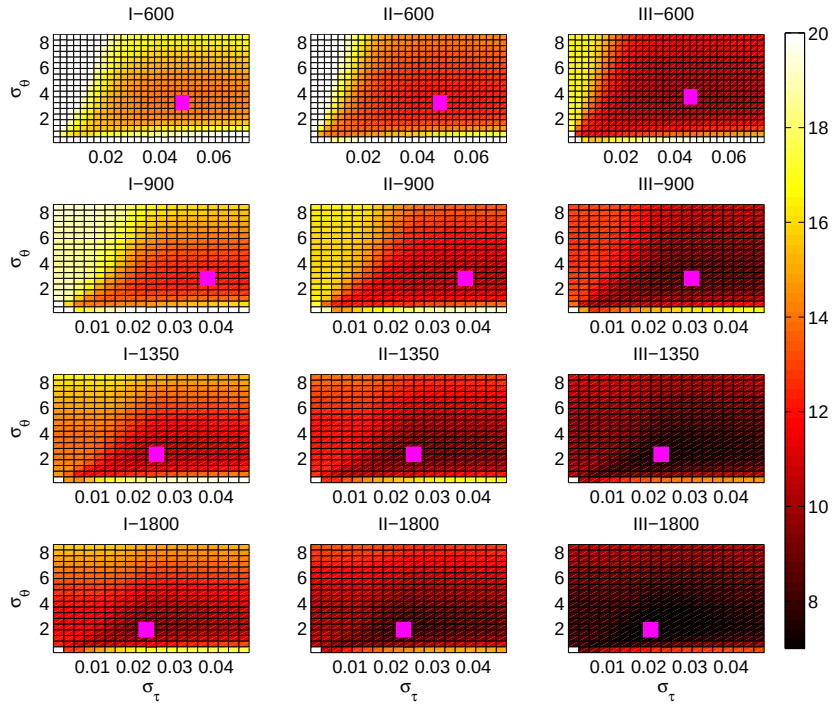

Figure 2.9: Results of the exhaustive search for the two NC kernel parameters σ_θ and σ_τ for all tested input data sets. The magenta squares indicate the minimum RMSE and hence the estimated kernel parameters.

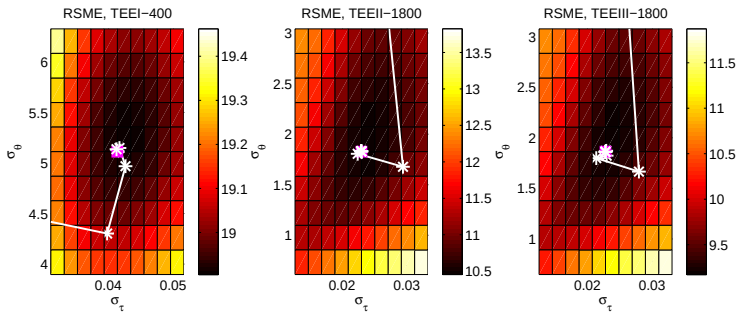

Figure 2.10: RMSE for TEEI, TEEII, and TEEIII reconstructed with 400 and 1800 2D images. The QN iterations are indicated by white line.

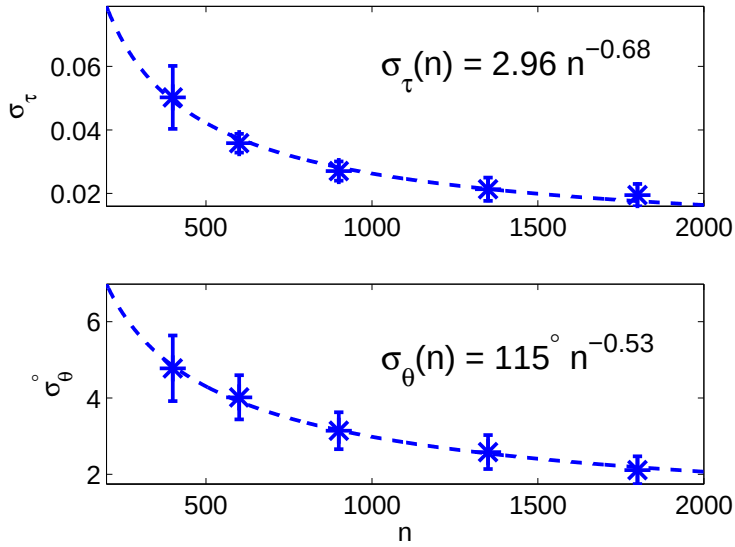

Figure 2.11: Average estimated optimal kernel sizes (σ_θ and σ_τ) of the entire data set. The error bars represent the standard deviation. The dashed line represents the power law fits. The model parameters are given in the plots.

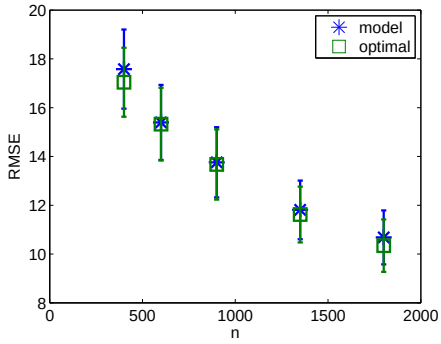

Figure 2.12: RMSE for reconstructions using optimal and predicted (model) NC kernel sizes as a function of the number of 2D images. The error bars represent the standard deviation.

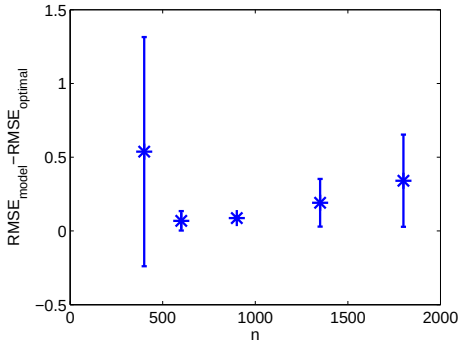

Figure 2.13: Difference in RMSE between reconstructions using optimal ($RMSE_{optimal}$) and model kernel sizes ($RMSE_{model}$).

with respect to the kernel sizes. This translates into a speed up of more than 3 since 121 computations were needed for the exhaustive search shown in Fig. 1. The QN-optimizer reaches within 3 to 4 iterations one step size of the optimum obtained by the exhaustive search. We believe that we could relax the stopping criteria of the QN-optimizer and speed up the optimization even more.

2.5 Conclusion

In this work we showed that NC with optimized kernel sizes outperforms NN and LTB consistently for all three tested TEE images as well as for the 2D input image distributions. We could show that the optimal kernel parameters depend more on the input data distribution than on the image content. We could show that the previously established method [51] of finding the optimal kernel sizes for NC works well on different TEE data sets obtained from the same patient. We used three original 4D echocardiographic data sets as ground truth and showed that RMSE provided a smooth cost function for all sub TEE sets. With this we were able to run a QN optimizer and find successful optimal NC kernel sizes which can be successful predicted by a power law model. With this model any number of 2D input images can optimally being reconstructed.

Table 2.3: Average RMSE ± standard deviation of 15 3D time frames for different reconstruction methods of set TEE I

set	I-600	I-900	I-1350	I-1800
avg. RMSE opt. NC	13.8 ± 1.32	12.2 ± 1.07	10.4 ± 0.60	9.4 ± 0.60
avg. RMSE NN	17.8 ± 1.68	16.1 ± 1.44	13.9 ± 1.27	12.0 ± 0.95
avg. RMSE LTB	16.4 ± 2.23	15.8 ± 2.70	15.1 ± 2.82	14.7 ± 2.64

Table 2.4: Average RMSE ± standard deviation of 15 3D time frames for different reconstruction methods of set TEE II

set	II-600	II-900	II-1350	II-1800
avg. RMSE opt. NC	11.9 ± 1.65	10.5 ± 1.27	9.0 ± 0.68	8.3 ± 0.72
avg. RMSE NN	15.1 ± 1.56	13.7 ± 1.23	12.0 ± 1.13	10.4 ± 0.81
avg. RMSE LTB	14.0 ± 2.23	13.3 ± 2.35	12.8 ± 2.36	12.4 ± 2.29

Table 2.5: Average RMSE ± standard deviation of 15 3D time frames for different reconstruction methods of set TEE III

set	III-600	III-900	III-1350	III-1800
avg. RMSE opt. NC	9.9 ± 1.42	8.7 ± 0.94	7.4 ± 0.51	6.7 ± 0.55
avg. RMSE NN	12.3 ± 1.22	11.1 ± 1.01	9.6 ± 0.91	8.3 ± 0.64
avg. RMSE LTB	11.7 ± 1.90	11.3 ± 2.05	10.9 ± 2.05	10.6 ± 1.99

Acknowledgment

We would like to thank our clinical fellows W.B. Vletter, M.L. Geleeijnse, J. Mc Ghie, and B. Ren for acquiring the TEE sets.

This research is supported by the Dutch Technology Foundation STW, which is the applied science division of NWO, and the Technology Programme of the Ministry of Economic Affairs.

Chapter 3

Segmentation of multiple heart cavities in 3D transesophageal ultrasound images

This chapter has been published as:
A. Haak, G. Vegas-Sánchez-Ferrero, H.W. Mulder, B. Ren, H.A. Kirişli,C. Metz, G. van Burken, M. van Stralen, J.P.W. Pluim, A.F.W. van der Steen , T. van Walsum and J.G. Bosch, Segmentation of multiple heart cavities in 3D transesophageal ultrasound images, *IEEE Transaction on Ultrasonics, Ferroelectrics, and Frequency Control* accepted (2015).

Abstract
Three-dimensional transesophageal echocardiography (3D TEE) is an excellent modality for real-time visualization of the heart and monitoring of interventions. To improve the usability of 3D TEE for intervention monitoring and catheter guidance, automated segmentation is desired. However, 3D TEE segmentation is still a challenging task due to the complex anatomy with multiple cavities, the limited TEE field of view, and typical ultrasound artifacts. We propose to segment all cavities within the TEE view with a multi-cavity Active Shape Model (ASM) in conjunction with a tissue/blood classification based on a Gamma Mixture Model (GMM). 3D TEE image data of twenty patients were acquired with a Philips X7-2t matrix TEE probe. Tissue probability maps were estimated by a two-class (blood/tissue) GMM. A statistical shape model containing left ventricle, right ventricle, left atrium, right atrium and aorta (LV, RV, LA, RA, Ao) was derived from Computed Tomography Angiography (CTA) segmentations by Principal Component Analysis. ASMs of the whole heart and individual cavities were generated and consecutively fitted to tissue probability maps. First, an average whole-heart model was aligned with the 3D TEE based on three manually indicated anatomical landmarks. Second, pose and shape of the whole-heart ASM were fitted by a weighted update scheme excluding parts outside of the image sector. Third, pose and shape of ASM for individual heart cavities were initialized by the previous whole heart ASM and updated in a regularized manner to fit the tissue probability maps. The ASM segmentations were validated against manual outlines by two observers and CTA derived segmentations. Dice coefficients and point-to-surface distances were used to determine segmentation accuracy. ASM segmentations were successful in 19 of 20 cases. The median Dice coefficient for all successful segmentations vs. the average observer ranged from 90 to 71 % compared to an inter-observer range of 95 to 84 %. The agreement against the CTA segmentations was slightly lower with a median Dice coefficient between 85 and 57 %. In this work we successfully showed the accuracy and robustness of the proposed multi-cavity segmentation scheme. This is a promising development for intraoperative procedure guidance, e.g. in cardiac electrophysiology.

3.1 Introduction

Three-dimensional (3D) ultrasound is becoming more and more important for monitoring minimally invasive interventions. Currently, 3D ultrasound is the only feasible modality which would allow real-time 3D monitoring of interventions [45]. Compared to transthoracic echocardiography transesophageal echocardiography (TEE) is especially attractive for cardiac interventions, because of its superior image quality and stable, non-obstructive, externally controllable position of the transducer within the esophagus. In particular, 3D TEE allows direct real-time visualization of the complex 3D anatomy of the different heart cavities, valves and the relative position of catheters, and closure devices, etc. The transducer is close to the heart, showing important structures such as valves with high resolution, without image deterioration by the chest wall, ribs and lungs. However, since the transducer is so close, the TEE field of view (FoV) is limited, allows only a partial image of several heart cavities and is highly dependent on probe manipulation. TEE imaging of the whole heart is mostly impossible. Therefore, image interpretation requires expertise and automated segmentation of 3D TEE data which is still challenging [22]. For procedure guidance, the 3D TEE image should ideally be placed within a model of the heart, allowing navigational help at a multitude of intervention sites. To this end, we propose a cardiac 3D multi-cavity model automatically fitted within the TEE FoV. This forms the basis for an automatic relative positioning of the image, as well as an automated segmentation of the cavities. This can be used in support of cardiac electrophysiology interventions, e.g. to allow accurate navigation of catheters. Cardiac electrophysiology (EP) concerns the treatment of conduction and rhythm disorders of the heart. It is a field of rapidly increasing importance within cardiology [122, 58]. During EP interventions, the source of the conduction abnormality is located and treated by tissue ablation. First, position-sensing catheters are used to create a 3D electro-anatomical map (EAM) of the surface of a heart cavity, e.g. the left atrium (LA). By positioning the tip at a large number of locations on the cavity wall and recording the local ECG signal and 3D position, a 3D map of the cavity with its conduction pattern is created. This is a lengthy process with imprecise results. The EAM is rendered in an EP guidance system (e.g. Carto 3 (Biosense Webster, Diamond Bar, CA) or Ensite Velocity (St. Jude Medical, St. Paul, MN), with the positions of all tracked catheters, to guide the intervention. Next, an ablation catheter is navigated to the erroneous conduction sites and tissue is ablated to restore a normal conduction pattern. This requires a precise visualization of the anatomical structures. However, the EAM is imprecise and not detailed. Several approaches have been introduced to improve this guidance. Preoperative CT and MR data have been used, from which several heart cavities are segmented and the surfaces imported into the guidance system [85]. However, such preoperative images often fail to improve the EAM since the CT/MR images are generally taken weeks in advance which may lead to considerable changes in the anatomy or physiological state. Moreover, the CT/MR images are in different coordinate frames

which makes a registration necessary. Ideally, the 3D TEE ultrasound data should be segmented and anatomical structures and catheters identified for representation in the interventional guidance system. This could both be done on preoperatively acquired 3D TEE (for creating a preoperative anatomical map without the need for CT or MR) or on live intraoperative 3D TEE, to allow live guidance of the catheter positions with respect to true anatomy and EAM. Our proposed approach is the foundation of such applications.

Segmentation of ultrasound images in general is a challenging task [102]. The characteristic speckle structure of an ultrasound image precludes simple separation of different tissues. The images are anisotropic, inhomogeneous in gray level amplitude and very dependent on probe positioning. Furthermore, ultrasound suffers quite often from artifacts such as echo drop outs and shadowing due to poor probe contact, air bubbles and calcifications.

Many models have been described for the speckle statistics of the backscattered ultrasound RF-data (gray level amplitude) [20], [154]. Most of the theoretical work has been focused on modeling raw RF-data neglecting all the proprietary post processing steps of commercial ultrasound scanners. However, empirical fitting of different distributions to log-compressed [138] and uncompressed [101] gray level data revealed that the Gamma distribution fits such data quite well.

In cardiac ultrasound, segmentation is even more challenging since multiple (incomplete) structures are involved, which have a complex and highly time-variable shape, and there is a substantial anatomical and pathological variability over the population [81, 102]. While many approaches have been presented for automated segmentation of the left ventricle in transthoracic 3D echocardiograms [81, 10, 100], especially for the left ventricle, there are few approaches for 3D TEE segmentations [22, 66]. The segmentation approach we present meets the following requirements: it deals with ultrasound peculiarities, partially missing information, anatomical variability, and multiple complex structures. We propose a multi-object Active Shape Model (ASM) [30] for this. ASMs are based on statistical shape models and describe the shape variation of a population of shapes using Principal Component Analysis (PCA). This allows the model to generate any shape in the population plus any 'plausible' intermediate or extrapolated form. They are also known to handle missing data very well [7]. Multiple interrelated objects and multidimensional shapes are handled in a natural way.

We present and evaluate an Active Shape Model segmentation method for 3D TEE which uses a multi-cavity shape model in conjunction with a blood/tissue classifier based on Gamma Mixture Models (GMM) of gray level amplitudes. To our knowledge, this is the first time a multi-cavity ASM was used in combination with a GMM tissue classifier. For all patients TEE and Computed Tomography Angiography (CTA) images were acquired, and manual outlines were created in the TEE images by two observers. These were compared to the ASM and TEE segmentations. We also automatically segmented the CTA images by a well-established atlas-based

method [73]. We registered the results to the TEE segmentations, to compare the results within the TEE sector and also to investigate extrapolation of the heart chambers outside the sector. Furthermore, comparing the registered CTA segmentations with the manual outlines may give some insight into how well the segmentations from the different modalities agree, which is important since the physical image formation principle, segmentation method, acquisition time and coordinate frame are different. We previously demonstrated a preliminary version of our method on a small data set [53, 52]. In this paper we present our method in detail and evaluate on a data set of twenty patients.

3.2 Methodology

3.2.1 Gamma Mixture Model

Segmentation in echocardiograms is generally complicated by speckle noise. Ultrasound images naturally exhibit local gray level variations (speckle) due to sound scattering by randomly distributed sub-resolution scatterers. This leads to the typical 'noisy' speckle images which may have a locally poor definition of edges. Using only the local gray level information to find the borders of the different heart chambers usually renders inaccurate segmentations.

The ultrasound speckle statistics depend on many parameters of the medium (scatterer size/density, attenuation, heterogeneity etc.) and parameters of the ultrasound system (resolution cell dimension, frequency and bandwidth, interpolation, compression etc.). Classical approaches make use of the assumption of a high number of scatterers per resolution cell which will lead to Rayleigh and Rice distributions. However, modeling the speckle distribution after all processing steps in commercial scanners is difficult since there are many nonlinear processing steps such as adaptive filtering and log-compression. Vendors usually do not disclose the parameters of their processing pipeline. Some researchers have empirically compared the fit of different types of distributions to log-compressed gray level data [138] and to linearly processed RF envelope data [101]. They have shown that the Gamma distribution fits both types of data well. Previously, Vegas-Sanchez-Ferrero et al. [151, 148] showed that a GMM models the gray level distribution of ultrasound images after beam-forming, post-processing, and interpolation in an accurate and effective way.Therefore, we decided to use a Gamma mixture model to describe the speckle distribution of our log-compressed gray level data. [148, 138, 101].

For estimating the likelihood of a region being blood or tissue a two-class mixture model is used. We consider the voxel gray levels of an image region as an identically distributed random variable:

$$\mathbf{X} = \{X_i\}\,,\ 1 \leq i \leq N, \tag{3.1}$$

where N denotes the number of voxels in the region considered. The probability density function[1] p of such a mixture model is given by

$$p\left(x|\mathbf{\Theta}\right) = \sum_{j=1}^{2} \pi_j f_X\left(x|\alpha_j, \beta_j\right), \tag{3.2}$$

where the vector $\mathbf{\Theta}$ holds the parameters for both classes $j = \{1, 2\}$ of the model $(\pi_1, \pi_2, \alpha_1, \beta_1, \alpha_2, \beta_2)$ and f_X denotes the Gamma density function [151] with parameters α and β. The weighting terms π_j stand for the prior probabilities of each class $\pi_j = P\left(Class = j\right)$ and, thus, the condition $\sum_{j=1}^{2} \pi_j = 1$ holds. The parameters in $\mathbf{\Theta}$ can easily be estimated with the Expectation-Maximization algorithm [95].

An example histogram of the gray levels and the fitted GMM with the blood and tissue class are shown in Fig. 3.1. Please note that the GMM models the empirical distribution quite well. On all patient histograms and fitted GMMs we computed a Kolmogorov-Smirnov metric of 0.013±0.004 (mean±standard deviation). Furthermore, we computed the Kullback-Leibler divergence [151, 40] for all data sets which was on average 0.03±0.01 (mean±standard deviation). Both metrics support our assumption that the log-compressed gray level distributions can be modeled adequately with the GMM.

Finally, probability maps of voxels belonging to blood or tissue ($k = 1, 2$, respectively) are computed using Bayes' theorem:

$$p_k\left(x|\mathbf{\Theta}\right) = \frac{\pi_k f_X\left(x|\alpha_k, \beta_k\right)}{\sum_{j=1}^{2} \pi_j f_X\left(x|\alpha_j, \beta_j\right)}. \tag{3.3}$$

An example 3D ultrasound volume and the computed tissue probability map are shown in Fig. 7.4.

3.2.2 Active shape model

An active shape model [29] represents any shape, $\mathbf{s}$, in a population as the average shape $\bar{\mathbf{s}}$ plus a linear combination of the principal modes of variation, which are described by the eigenvector matrix Φ and the corresponding coefficients $\mathbf{b}$

$$\mathbf{s} = \bar{\mathbf{s}} + \Phi\mathbf{b}, \tag{3.4}$$

where $\mathbf{s}$ contains the n 3D vertices of the shape $\mathbf{s} = (x_1, y_1, z_1, \ldots, x_n, y_n, z_n)^T$. Usually, the smaller modes of shape variation are removed from the model to suppress noise and to reduce the dimensionality of the model. The ASM used in this work was derived from 151 CTA segmentations [73, 91] containing the left and right ventricle (LV and RV), left and right atria (LA and RA) and the aorta (Ao). The CTA

[1] Please note that we use lower case p for indicating probability density functions (pdf) and capital P for probabilities.

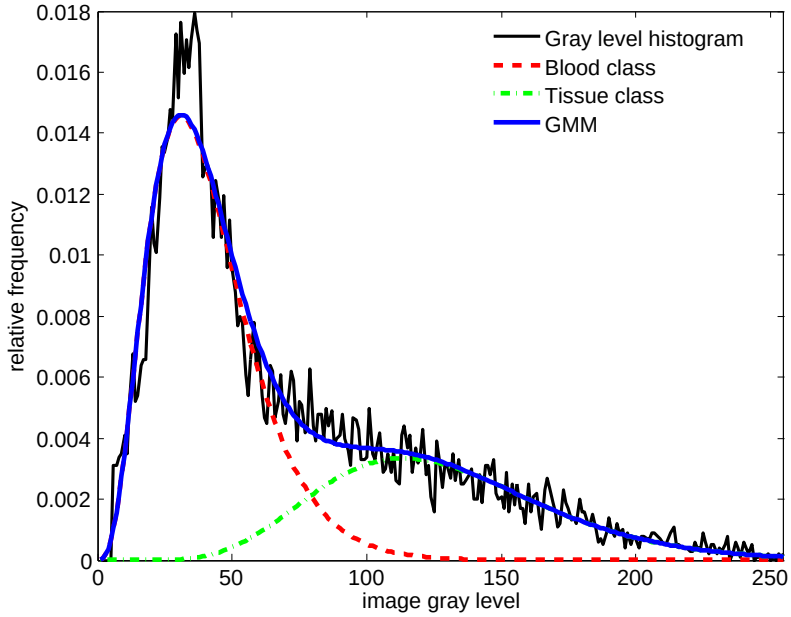

Figure 3.1: The GMM (blue solid line) fitted to the log-compressed gray level histogram (black solid line). Grey levels smaller than 5 were discarded to remove areas outside the imaging cone. A k-means ($k = 2$) classifier was used to initialize the GMM. The blood (red dashed line), and tissue (green dashed line) classes are shown in the plot as well. We computed for this example a Kullback-Leibler divergence of 0.025 and a Kolmogorov-Smirnov metric of 0.015, which both support the suitability of using the GMM to model the log-compressed gray level distributions[151, 40].

scans were made from a mixed population of patients presenting a large variability in anatomy and pathology [91]. The mean shape of the ASM is shown in Fig. 3.3

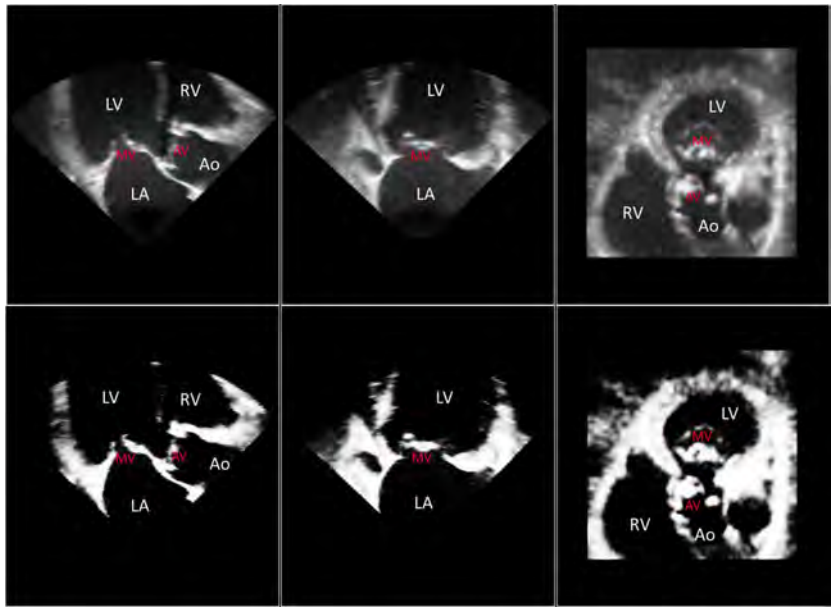

Figure 3.2: Three orthogonal cross sections through a TEE volume (top) and the corresponding tissue probability map (bottom). Note the reduction in speckle of the tissue probability map compared to the gray level map.

and consists of about 10^4 3D vertices. ASM segmentation is achieved by initializing the shape model at a certain position in the image and finding new candidate points in the neighborhood of the shape. The pose and shape of the ASM is then iteratively estimated (by backprojecting the new shape on the model) until the ASM converges. Update points ($\mathbf{r}'$) are found along the surface normals by minimizing an objective function as described by Van Ginneken *et al.* [143], which gives a robust estimator of the blood-tissue transition point. We adopted this approach since we use a CTA-derived ASM and therefore cannot model the TEE gray level or probability map profiles along the surface normals. A weighted least square scheme is used to estimate the pose ($T(a_i, \boldsymbol{\theta}_i, \mathbf{t}_i)$, with a_i being the scale, $\boldsymbol{\theta}_i$ being the Euler angles, and $\mathbf{t}_i$ being the translation at the iteration i) [5, 65] and the shape parameter ($\mathbf{b}'_i$) for each iteration similar as described by Cootes *et al.* [28] which gives for the new shape at iteration i

$$\mathbf{b}'_i = \left(\Phi^T W \Phi\right)^{-1} \Phi^T W \left(\bar{\mathbf{s}} - \mathbf{s}'_i\right), \tag{3.5}$$

where W is a diagonal matrix containing the vertex weights, w, and $\mathbf{s}_i$ is the current shape (e.g. the transformed update points $\mathbf{s'}_i = T(a_i, \boldsymbol{\theta}_i, \mathbf{t}_i)\,\mathbf{r'}$). The newly found pose and the shape parameters are regularized with c (rotation, translation, shape) and c_a (scale) to prevent pose jumps by erroneous edge responses

$$a_i = c_a a_{i-1} + (1 - c_a)\, a'_i, \tag{3.6}$$

$$\boldsymbol{\theta}_i = c\boldsymbol{\theta}_{i-1} + (1 - c)\, \boldsymbol{\theta'}_i, \tag{3.7}$$

$$\mathbf{t}_i = c\mathbf{t}_{i-1} + (1 - c)\, \mathbf{t'}_i, \tag{3.8}$$

and

$$\mathbf{b}_i = c\mathbf{b}_{i-1} + (1 - c)\, \mathbf{b'}_i, \tag{3.9}$$

where dashes ($'$) denote the estimated unregularized pose and shape parameters at the iteration i.

The vertex weighting factor w consists of a GMM based edge probability $w_{GMM}(\mathbf{r'})$, a model distance term $w_{ASM}(\mathbf{r'})$, and a term penalizing points outside or closed to the border of the pyramidal TEE volume $w_{US}(\mathbf{r'})$. The weighting factor is computed as follows:

$$w(\mathbf{r'}) = w_{ASM}(\mathbf{r'})\ w_{US}(\mathbf{r'})\ w_{GMM}(\mathbf{r'}), \tag{3.10}$$

where

$$w_{ASM}(\mathbf{r'}) = \exp\left(-\frac{(||\mathbf{r} - \mathbf{r'}||)^2}{\sigma^2}\right). \tag{3.11}$$

The parameter σ defines the range of the model distance penalty term and $||$ indicates the Euclidian distance.The term $w_{US}(\mathbf{r'})$, is derived by convolving the binary TEE mask with an isotropic Gaussian kernel with a standard deviation of $\sqrt{20}$ voxel. The GMM term, $w_{GMM}(\mathbf{r'})$, enhances update points being close to the blood/tissue transition zone (probability of 0.5) and is defined as

$$w_{GMM}(\mathbf{r'}) = 1 - \frac{|p_2(I(\mathbf{r'})|\boldsymbol{\Theta}) - 0.5|}{0.5}, \tag{3.12}$$

where $I(\mathbf{r'})$ is the local gray level in the TEE image at $\mathbf{r'}$ and $p_2(I(\mathbf{r'})|\boldsymbol{\Theta})$ stands for the tissue pdf.

3.2.3 Segmentation scheme

We use a three-stage segmentation scheme (see Fig. 7.5) where the model pose is increasingly regularized from stage to stage. The scheme comprises the following stages:

First stage. In the first step, the ASM of the entire heart containing all cavities (ASM_{total}) is used. The mean shape ($\bar{\mathbf{s}}_{total}$) of this ASM is initially transformed to the TEE image by a similarity transform T_{init} which was derived by manually indicating

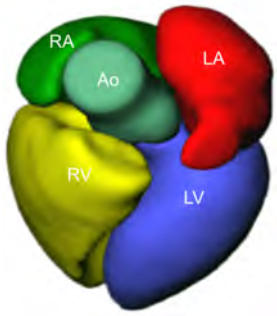

Figure 3.3: Mean shape of multi-cavity statistical shape model [91].

three landmark points in the TEE image (center of mitral valve, center of aortic valve, and LV apex or a point on the LV long axis). The regularization factors, c and c_a, are set to zero.

Second stage. After the initial pose estimation, the pose and shape of ASM_{total} are iteratively updated with intermediate regularization. A shape model covering 90 % of the shape variation is used. New shape parameters, $\mathbf{b}$, are computed from the update points ($\mathbf{r}'$) and $\mathbf{b}$ is limited to a hyper-ellipsoid ($\mathbf{b}_{lim}$) by computing the χ^2 distributions and taking the 98 % percentiles as limit [29].

Third stage. In the last stage of the segmentation, for each cavity, a separate shape model covering 98% of the shape variation is used. The pose and shape updates of each ASM are more strongly regularized by setting c to 0.6. The shape updates are again limited to a hyper-ellipsoid, corresponding to 99.7% percentile.

For all stages, we limit the scale (a_{lim}), the rotation angles ($\boldsymbol{\theta}_{lim}$), and the translation ($\mathbf{t}_{lim}$). All limits for the different stages and all other parameters are shown in table 7.1.

The parameters for the ASM segmentation scheme were empirically chosen based on segmentations of previous data sets.

3.3 Experiments

3.3.1 Data

The segmentation method was validated in 3D TEE data sets obtained from twenty patients (13 male, 7 female; mean age ± standard deviation: 80±7) undergoing a Transcatheter Aortic Valve Implantation (TAVI) in accordance with the hospital ethical regulations. The patients had all severe aortic valve stenosis with different severity of valve regurgitation. This caused for many patients severe pathologies with con-

Table 3.1: Segmentation parameters: σ defines the range of w_{ASM}, c regularizes $\boldsymbol{\theta}, \mathbf{t}, \mathbf{b}$, and c_a regularizes a at each iteration. Upper and lower limits for the pose and shape parameters have the subscript lim.

parameters	stage 1 (S1)	stage 2 (S2)	stage 3 (S3)
c	0.0	0.2	0.6
c_a	0.0	0.2	0.3
σ (voxel)	44	20	20
a_{lim} (%)	$\pm$30 of a_{init}	$\pm$18 of a_{S1}	$\pm$15 of a_{S2}
$\boldsymbol{\theta}_{lim}$ (°)	$\pm$30 of $\boldsymbol{\theta}_{init}$	$\pm$20 of $\boldsymbol{\theta}_{S1}$	$\pm$5 of $\boldsymbol{\theta}_{S2}$
$\mathbf{t}_{lim}$ (mm)	$\pm$30 of $\mathbf{t}_{init}$	$\pm$20 of $\mathbf{t}_{S1}$	$\pm$5 of $\mathbf{t}_{S2}$
$\mathbf{b}_{lim}$(%)	0.0	98.0	99.7

siderable left ventricular and atrial enlargement and hypertrophy. All TAVI patients had 3D TEE data acquired with a matrixTEE probe (X7-2t, Philips Healthcare, The Netherlands) during the preparation of the intervention. The patients were anesthetized and in supine position. Conventional log-compressed gray level data was used in the study.The sonographer used a preset but was free to adapt the machine parameters image depth (10$\pm$2 cm), focus, gain (47$\pm$5 dB), compression (49$\pm$1 %), and time-gain curve to yield the best and most homogeneous image quality for the specific patient. One heart cycle was acquired in "Live 3D" mode (no stitching of sub-volumes acquired over several cardiac cycles) yielding a frame rate of about 4 $\pm$ 1 volumes/sec. The power settings were fixed yielding an MI of 0.5 and a TI of 0.1. All patients also underwent a gated CTA for preoperative planning. Usually, 19 time frames were acquired and the ED time frame was selected. The CTA volumes were cropped so that only the heart was in the image volume.

3.3.2 Gold standard and Evaluation of Ground Truth

To provide a segmentation ground truth, 2D contours of all visible cavities in multiple short and long axis views were manually annotated by two independent observers in all end-diastolic (ED) TEE images. The ED time-frame was manually selected by visual inspection of the mitral valve (closed) and the LV (largest volume). To speed up the manual outline we used the roughly aligned mean shape ($\bar{\mathbf{s}}_{total}$) as starting point for the observer outlines. First, one observer indicated four landmark points on the mitral valve (MV) annulus, one on the aortic valve (AV), and one at the apex of the left ventricle. The center of the four MV points, AV, and apex point were then used to compute an initial similarity transform for the mean shape of the total heart model ($\bar{\mathbf{s}}_{total}$). The mean shape was overlaid on the TEE image and small adjustments could be made to the landmark points to obtain an optimal initial pose

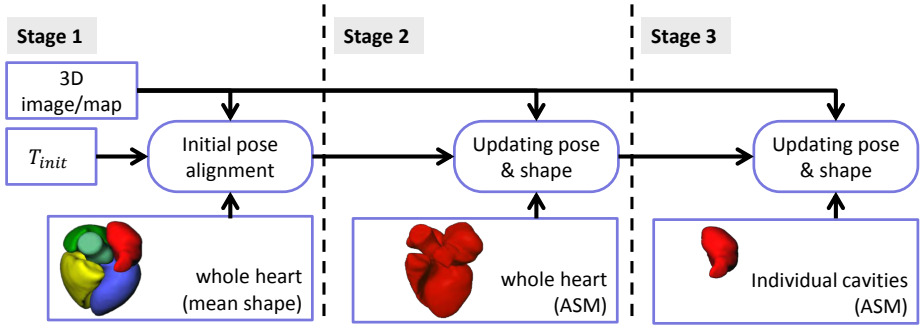

Figure 3.4: Three stage segmentation scheme which adjusts the pose and shape of the model from stage to stage. In the first stage the mean shape of the entire heart model ($\bar{\mathbf{s}}_{total}$) is aligned to the TEE volume and the found pose is passed to stage 2. Secondly, the pose and shape of the complete heart (ASM_{total}) is updated. In the third stage, individual ASM's for each cavity are fitted to the TEE volume.

of the model. Using this transformation as a starting point, the manual outlining was performed independently by two observers, in eleven 2D short axis views and 4 collinear long axis views, obtained by slicing the TEE image and the mean shape model. The 2D contours of $\bar{\mathbf{s}}_{total}$ were interpolated by B-splines and the control points were interactively manipulated by the observers to adapt the contours to the correct borders of the different cavities. Crossing points of contours from the different short- and long-axis planes were displayed in the respective perpendicular planes to ensure 3D consistency in the manual outlines. Please note that outlines outside the FoV are leftovers from the initialization with the mean model and are not used in any way.Papillary muscles and trabeculations were included in the cavities (excluded from myocardium) as recommended in the ASE guidelines [78]. An example TEE volume with the outlines of one observer is shown in Fig. 3.5. From the two manual segmentations, an 'Average Observer' segmentation was constructed as the ground truth segmentation. The Average Observer contour was created by computing for each plane the signed distance map for both observer contours and adding these maps. This produces a map where the average contour is represented by the zero pixel values. The resulting map was thresholded and the average observer contour points were detected by a fast marching squares scheme [84]. Additionally, CTA images were obtained from the same twenty patients and were segmented in 3D using the multi-atlas based approach introduced in [73]. Please note that the used ASM did not include any of these CTA segmentations. For one patient the segmentation failed due to severe pathology. Therefore, we excluded this CTA segmentation from our analyses. The

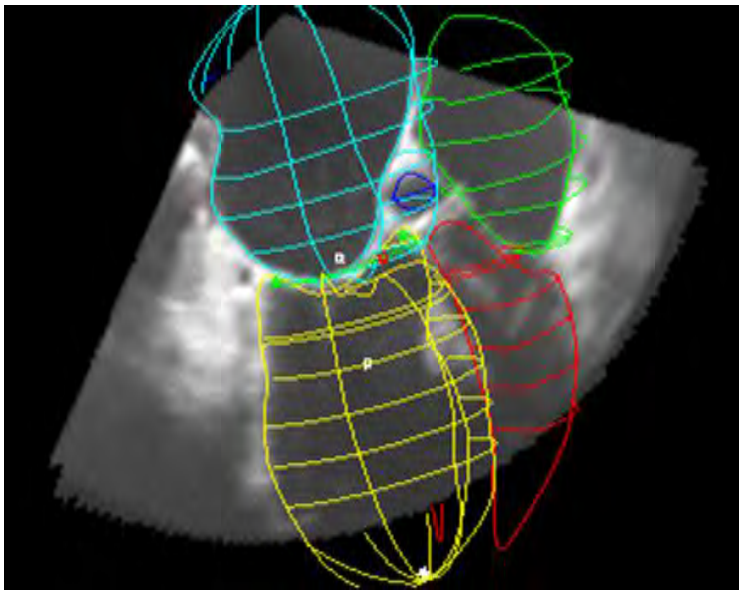

Figure 3.5: Example of manual annotation of the heart cavities in 15 slices of a TEE volume.

CTA segmentations provide an independent ground truth of the cavity outline. In contrast to the manual TEE segmentations, these are fully 3D and not limited to the TEE sector. The statistical shape model was derived earlier from 151 CTAs of other patients of mixed pathology [91]. For the evaluation, ASM segmentations were compared to the manually defined average observer contours and to the CTA segmentations. Since the CTA is in a different coordinate system from the TEE, the two need to be registered first. The obtained CTA and TEE segmentations were rigidly registered using surface-based iterative closest point (ICP, see [11] for more details) alignment, after initial coarse alignment of the heart by registration of the center of gravities of the corresponding cavities.

3.3.3 Evaluation measures

For comparing the different segmentations, overlap in area or volume for each cavity was expressed as a Dice coefficient in 2D or 3D, as applicable [35]. The distance between corresponding segmentations was computed as average Euclidean point-to-surface distance. The Dice coefficients of segmented TEE and CTA volumes and the

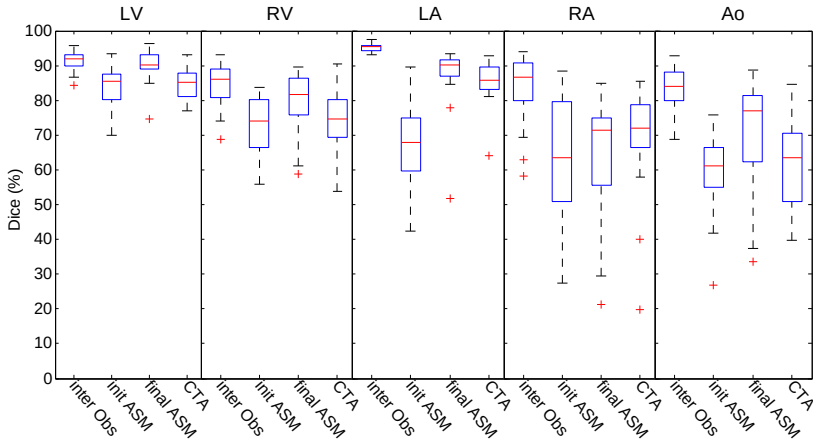

Figure 3.6: Dice coefficients for all five heart cavities between average observer (avg Obs) and different segmentations, averaged over all patients. From left to right: observer one vs. observer two (inter Obs); avg Obs vs. initial model (init ASM), avg Obs vs. final ASM TEE segmentation (final ASM), and avg Obs vs. the CTA segmentation (CTA). Please note that the Dice coefficient was computed only within the FoV.

mean point-to-surface distances ($P2S_{mean}$) were calculated within the pyramidal TEE image sector (cropped) as well as for the entire heart volume (complete). Several comparisons were made: first, the comparison of both manual observers to each other gave a measure of interobserver variability (inter Obs). This served as a baseline for the segmentation performance of the ASM. Second, the comparison of CTA to the average manual observer (ground truth) provided a measure of intermodality differences, registration, and segmentation inaccuracies. Third, the ASM TEE segmentations can be compared to the manual ground truth and to the CTA segmentations points lying within the TEE sector, to evaluate its performance. Fourth, by comparing the ASM cavity parts outside the sector to CTA, one can evaluate the extrapolation capabilities of the ASM. Fifth, by comparing the final ASM segmentation to the initial result, one can evaluate the value of the segmentation scheme. Please note that any evaluation measure using the manual outlines was only computed within the FoV.

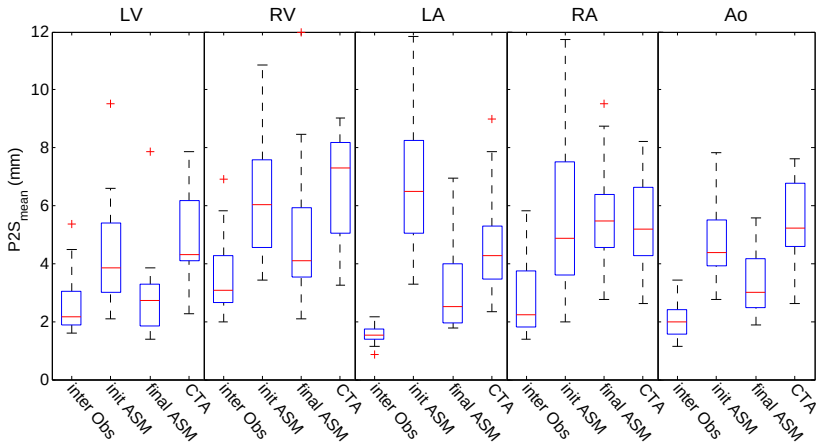

Figure 3.7: $P2S_{mean}$ for all five heart cavities between average observer (avg Obs) and different segmentations, averaged over all patients. From left to right: observer one vs. observer two (inter Obs); avg Obs vs. initial model (init ASM), avg Obs vs. final ASM TEE segmentation (final ASM), and avg Obs vs. the CTA segmentation (CTA). Please note that the $P2S_{mean}$ was computed only within the FoV.

Table 3.2: Mean Dice coefficients and $P2S_{mean}$

	LV	RV	LA	RA	Ao
Dice **inter Obs** (%)	91.3	84.2	95.2	83.4	82.7
Dice **init ASM** (%)	83.3	72.6	67.4	63.4	59.5
Dice **final ASM** (%)	90.0	79.5	87.4	64.8	70.1
Dice **CTA** (%)	84.5	74.7	85.3	68.9	61.6
$P2S_{mean}$ **inter Obs** (mm)	2.56	3.46	1.56	2.76	2.06
$P2S_{mean}$ **init ASM** (mm)	4.33	6.16	6.85	5.71	4.72
$P2S_{mean}$ **ASM** (mm)	2.82	5.17	3.10	5.70	3.34
$P2S_{mean}$ **CTA** (mm)	4.74	6.84	4.62	5.41	5.45

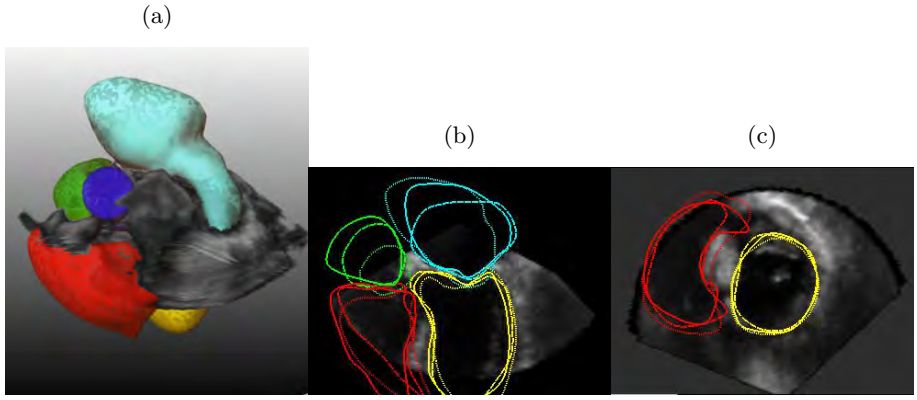

Figure 3.8: Qualitative example of a final ASM segmentation within the rendered 3D TEE volume (3.8a). The left ventricle is shown in yellow, the right ventricle in red, left atrium in cyan, the right atrium in green, and the aorta in blue. Two cross sections are shown in 3.8b and 3.8c with contours of the two manual observers (solid and dashed lines) and the final ASM (dotted lines). Note the limited field of view of the TEE probe.

3.4 Results

The inter-observer-variability Dice coefficients, and the $P2S_{mean}$ for all sets and heart cavities are shown in the boxplots of Fig. 3.6, and Fig. 3.7. The Dice coefficients, and the $P2S_{mean}$ of the average observer to $\bar{\mathbf{s}}_{init}$, to the final segmentation result, and to registered CTA segmentations are also shown in Fig. 3.6 and Fig. 3.7. Note that for the left heart chambers (LV and LA) we obtain the best interobserver variability and also the best segmentation results (final ASM). For the right heart chambers (RV and RA) we have less agreement between the observers and the ASM segmentation results agree less with the average observer. A qualitative comparison of an ASM segmentation with the two manual observers is shown in Fig. 3.8.

The Dice coefficients, and the $P2S_{mean}$ of the registered CTA segmentation with the average observer for all sets and heart cavities are shown in the boxplots of Fig. 3.6 and Fig. 3.7 (CTA). Note that generally the agreement between manual outlines and CTA segmentations is less than for the ASM segmentations.

The Dice coefficients and the $P2S_{mean}$ of the registered CTA segmentation with the ASM segmentations for all sets and heart cavities are shown in Fig. 3.9 and 3.10.

Note that the agreement of the segmentation for the full heart is only slightly

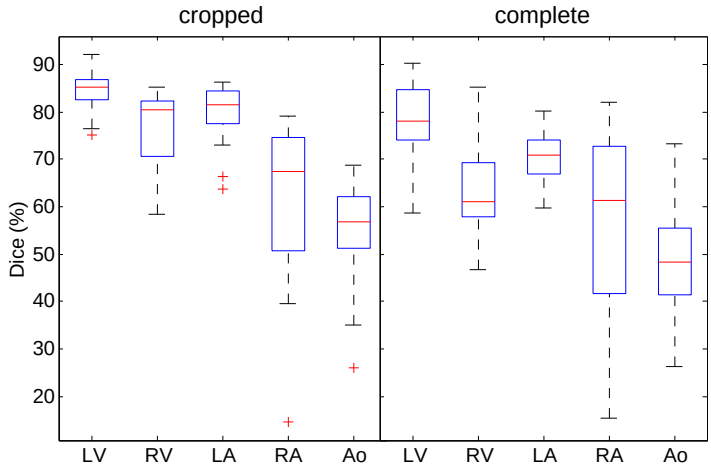

Figure 3.9: Dice coefficients of TEE vs. CTA segmentations (3D) considering only the TEE FoV (cropped) or the entire heart (complete).

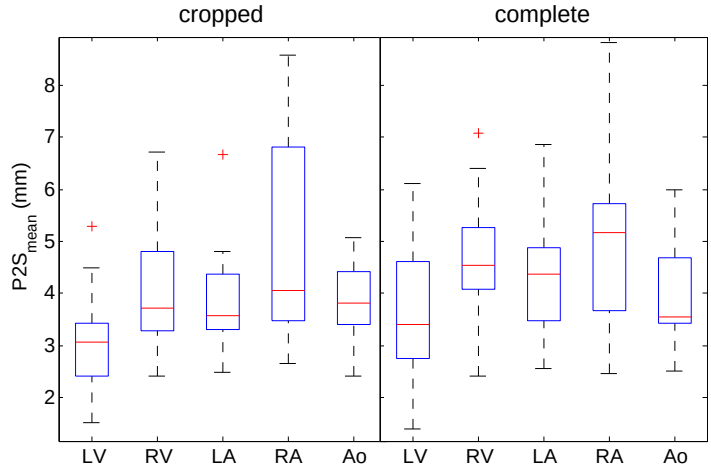

Figure 3.10: $P2S_{mean}$ of TEE vs. CTA segmentations (3D) considering only the TEE FoV (cropped) or the entire heart (complete).

decreased compared to the agreement confined within the field of view of the TEE image sector.

3.5 Discussion

In this paper, we validate our multi-cavity ASM segmentation method for 3D TEE on an extended data set of twenty patients. We successfully show that the proposed segmentation scheme, using a GMM tissue/blood classifier in conjunction with a multi-cavity ASM, can handle narrow view data and automatically identify different heart chambers in complex TEE images. The run time of the non-optimized segmentation scheme was in the order of 2 minutes for one patient data set.

The accuracy of the segmentation for the different cavities was reasonably close to the interobserver variability of the manual segmentations that served as ground truth. As should be expected, the final segmentation had a much higher overlap with the average observer than the initially placed average model for all cavities (see Fig. 3.6) and the Dice coefficient improved on average by 6.7, 6.9, 20.0, 1.3, and 11.0 percent points for LV, RV, LA, RA, and Ao respectively. For the LV and RV we could achieve segmentation accuracy close to the interobserver variability even though mostly large parts of the RV and LV were not visible in the TEE image. We also achieved a good segmentation for the LA (the second highest Dice score of all cavities segmented). However, the interobserver variability of the LA is very low, since this part has the best contrast in the image with the sharpest borders, and mostly simple anatomy (not much trabeculation). Although the ASM results cannot match this extremely low variability we still consider our segmentation scheme to provide good results. The results of the $P2S_{mean}$ support these findings. The LA segmentation may remain suboptimal due to the small visible portion of the LA in the TEE image (only the inferior part is visible) and negative influence of the combined model in previous steps. Specific optimizations of parameters per cavity (step 3) might help here.

The comparison of the ASM segmentations to automatically segmented CTA of the same patients showed good correspondence which is supported by the obtained Dice coefficients (see Fig 3.6). Comparing the correspondence for only the TEE sector to that for the entire heart, we see that the Dice coefficients drop by only a small amount: 6.3, 12.9, 8.9, 5.0, and 6.2 percent point which supports that the ASM has good generalization capabilities and can be used to extrapolate the heart cavities to beyond the limited view of the sector with reasonable accuracy. The good agreement of the TEE segmentations with the real anatomical structure can be qualitatively inspected by overlaying the transformed TEE segmentations with the CTA image as shown in Fig. 3.11.

The patients used in our study were quite different from the normal population with a rather abnormal anatomy (e.g. highly dilated atria) and reduced TEE image quality. Although this might form a challenge for the ASM's statistical shape model

coverage, still very acceptable segmentations were achieved. Only in one case the ASM did not converge: this case had a limited field of view with poor image quality and an indeterminate content. For all other cases, which included a wide range of anatomical variation, image orientations and artifacts, segmentation was successfully converging.

The remaining P2S errors are in the order of 3-4 mm for the different cavities. While this is sufficient for many applications, and better than accuracies of EAM or preoperative imaging in EP, precise interventions may require precisions in the order of 1-2 mm. An additional refinement by an alternative or hybrid edge finding might supply this.

There are some limitations in our study. The 3D ASM segmentations were only compared to several 2D average observer contours which present a rather coarse sampling of the 3D structures segmented. However, there is currently no feasible manual ground truth for studies dealing with larger data sets. We tried to overcome this limitation by introducing an alternative ground truth provided by the CTA segmentations. However, the CTA and ASM segmentation need to be registered which may bias our results. An image-based registration may overcome this problem but we are not aware of any robust automatic method. Furthermore, the contrast in CTA image intensities and the detected edges in the GMM (e.g. probability of 0.5) are caused by different physical mechanisms and may differ considerably. Also, there may have been a significant amount of remodeling of the heart anatomy or change in physiological conditions since there were several weeks between the CTA scan and the intervention. In addition, the temporal sampling of the TEE volumes was quite low and may have resulted in mismatches between ASM and CTA segmentations. Furthermore, the starting point of the manual outlines and the initialization of the automatic segmentation were the same. This may have led to a bias during the outlining process. The Dice coefficients and $P2S_{mean}$ reveal that the initial model is very different from the manual contours and from the final segmentations (see Fig. 3.6 and 3.7). Therefore, we feel confident that the bias is minimal. Another limitation is the limited TEE FoV. Even though the segmentation scheme seems to extrapolate the cavities outside the FoV relatively well, we would like to investigate if image fusion of different TEE views will improve the segmentation results.

Several extensions of the current approach are foreseen. Further improvement may be reached by optimizing algorithmic parameters per cavity or adding a final contour refinement stage. An iterated local estimation of blood/tissue probability based on prior local knowledge of blood and tissue from the previous model estimate could be a promising approach. The integration of an automatic landmark detection scheme is a promising extension, which will render our approach into a fully automatic segmentation scheme. Application in EP patients, including models generated from such patients, is a following step.

Figure 3.11: Qualitative example of a TEE segmentation transformed into the corresponding CTA volume.

3.6 Conclusion

In this work we successfully showed on 20 patient data sets that our segmentation approach is robust and accurate. This whole-heart model segmentation method will provide excellent opportunities for multi-view fusion and instrument tracking in procedure guidance.

Acknowledgment

We would like to thank Nora Baka and Stefan Klein for their inputs and fruitful discussion about active shape models, registrations, and programming techniques.

This research is supported by the Dutch Technology Foundation STW, which is the applied science division of NWO, and the Technology Programme of the Ministry of Economic Affairs.

Chapter 4

Fully automatic detection of salient features in 3D transesophageal images

This chapter has been published as:
A. H. Curiale, **A. Haak**, G. Vegas-Sánchez-Ferrero, B. Ren, S. Aja-Fernández, and J. G. Bosch,Fully automatic detection of salient features in 3D transesophageal images, *Ultrasound in Medicine and Biology* 40, no. 12 (2014).

Abstract
Most automated segmentation approaches for the mitral valve and left ventricle in 3D echocardiography require a manual initialization. In this article, we propose a fully automatic scheme to initialize a multi-cavity segmentation approach in 3D transesophageal echocardiography by detecting the left ventricle long axis, the mitral valve and the aortic valve location. Our approach uses a probabilistic and structural tissue classification to find structures such as the mitral and aortic valve; the Hough transform for circles to find the center of the left ventricle; and multidimensional dynamic programming to find the best position for the left ventricle long axis. For accuracy and agreement assessment, the proposed method was evaluated in 19 patients with respect to manual landmarks, and as initialization of a multi-cavity segmentation approach for the left ventricle, the right ventricle, the left atrium, the right atrium and the aorta. The segmentation results showed no statistically significant differences between manual and automated initialization in a paired t-test ($p > 0.05$). Additionally, small biases between manual and automated initialization were detected in the Bland-Altman analysis (bias, variance): left ventricle $(-0.04, 0.10)$, right ventricle $(-0.07, 0.18)$, left atrium $(-0.01, 0.03)$, right atrium $(-0.04, 0.13)$ and aorta $(-0.05, 0.14)$. These results show that the proposed approach provides a robust and accurate detection to initialize a multi-cavity segmentation approach without any user interaction.

4.1 Introduction

Echocardiography is one of the most relevant non-invasive diagnostic tools for real-time imaging of cardiac structure and function. Significant advances in three-dimensional transthoracic echocardiography (3D TTE) and transesophageal echocardiography (3D TEE) have made this modality a powerful tool in the clinic. Real-time 3D TEE, for instance, has become the standard echocardiographic modality for visualization of structures in the atrial and valvular regions of the heart [44]. It is also commonly used for establishing the diagnosis of the mitral valve, describing the precise anatomy, and for visualization of mitral regurgitant jets in mitral valve prolapse and functional mitral regurgitation [126, 46].

A global quantification of the cardiac function is highly desirable to treat different kinds of pathologies. For this purpose, identifying salient structures in an objective, reproducible and automated way is a prerequisite. 3D echocardiography (3DE) can provide accurate and reliable measurements for volumetric analysis and functional assessment of the right and left ventricle [132, 50, 97, 141]. However, the complexity of cardiac anatomy, poor contrast, noise and motion artifacts make the segmentation a challenging task.

Most segmentation approaches for the right and left ventricle depend on an appropriate initialization step [67]. Many model-based left/right ventricle segmentation approaches have been studied [110, 111]: Active Contours [70] and Level-Set [106] methods, Active Shape Models and Active Appearance Models [26, 27]. Unfortunately, all these models have shown a strong dependence on the initial model placement. In general, the effect of an improper initialization is the convergence to an undesired local minimum. Also, and despite of the efforts from the research community and medical vendors, a global quantification and volumetric analysis typically remains a time consuming task and heavily relies on user interaction. For example, the amount of time required to accurately extract the most common volumetric indices for the left ventricle for a single patient are in the range of 5 or 6 minutes [56, 135]. Thus, there is still a significant need for tools allowing fully automatic 3D quantification.

Recently, several studies have focused on the reduction of user interaction in different 3DE segmentation approaches for the mitral valve and left ventricle: [129] reduced the user interaction to one single point (near to the center of the mitral valve) in a mitral annulus segmentation approach, using a thin-tissue detector and a principal-component analysis. [114] proposed a fully automatic segmentation of the mitral leaflets in 3D TEE images using multi-atlas joint label fusion and deformable medial modeling. [144] proposed an automatic method to replace the manual initialization in 3D TTE segmentation approaches for the left ventricle using the Hough transform [8] for circles and multidimensional dynamic programming [139] to detect the left ventricle long axis (LV-LAX). Inspired by this work, [10] introduced an initialization algorithm using the Hough Transform for circles and multidimensional dynamic programming in 3D TTE to realize a fully automatic segmentation scheme for the left ventricle.

The Hough transform for circles has shown to be a powerful tool to provide an initialization in a wide range of automated and semi-automated segmentation approaches of the left ventricle [10, 93, 142, 144]. However, the anatomical pose information derived from these approaches (LV-LAX and mitral valve) does not suffice to initialize our multi-cavity model since the rotation around the LV-LAX remains unknown. To overcome this problem, we estimate the aortic valve location by using a detector which enhances thin tissue structures such as the mitral valve and aortic valve.

Some approaches for classifying structures have been proposed in the literature. [54] proposed a classification of local intensity structures based on the analysis of the eigenvalues of the Hessian matrix of intensity gradients. Sato et al.[127] generalized this approach to different types of local intensity structures such as lines, sheets and blobs. Recently, [21] combined this generalization with a k-means clustering to detect sheet-like structures, providing a rough initial segmentation of the mitral valve, which is subsequently refined by user interaction.

The structure classification proposed by Sato et al.[127] has a remarkable performance to detect lines, sheets and blobs in a wide range of medical images. However, a large number of misclassifications are introduced due to the typical granular pattern known as speckle, which is inherent to ultrasound (US) images. Speckle comes from the random interaction of scatterers within the resolution cell of US images [154]. For this reason, in our approach we introduce a probabilistic tissue characterization to prevent from misclassifications.

Several statistical models have been proposed in literature for describing the fully formed (or developed) speckle, salient among them the Rayleigh distribution. Different studies with real acquisitions have shown that other distributions, like Gamma or Nakagami, approximate the experimental distribution of real US images better than the Rayleigh distribution [101, 147]. In our approach we make use of the Gamma Mixture Model (GMM) into the structural tissue classification, because of its successful performance in filtering [146], classification [151] and registration [33] in 3D US images. However, it is important to note that the proposed methodology is not confined to the GMM model and any other probabilistic model can be used instead. For example, [82] used a Gaussian Mixture Model to segment different surgical instruments in 3D US images.

In contrast to the previous authors, in this work we focus on the reduction of user interaction for more complex 3D segmentation approach. Our main goal is to provide the initial anatomical information (3D position and orientation, 6 degrees of freedom) to initialize a multi-cavity segmentation approach for 3D TEE [53] without any user interaction. With this aim, we propose a new automatic approach to detect the LV-LAX, the mitral and aortic valve location. These locations will provide a suitable initialization of the multi-cavity segmentation method.

The main advantage of the proposed method is its robustness in 3D TEE images when compared to previous methodologies. Note that a 3D structure detection becomes a much more challenging task since many partial cavities are visible in the 3D

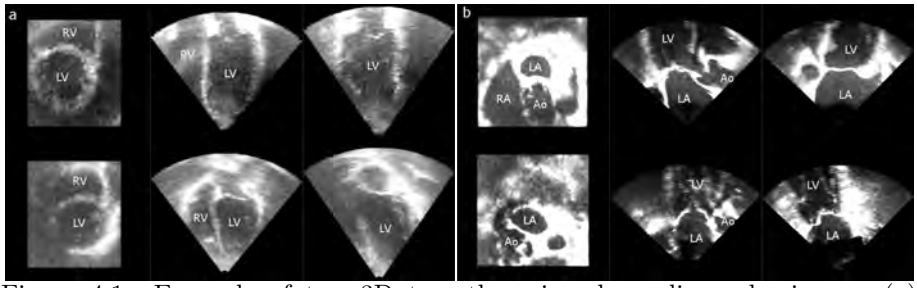

Figure 4.1: Example of two 3D transthoracic echocardiography images (a) and two 3D transesophageal echocardiography images (b) in three orthogonal views. This example illustrates the difficulty to identify the left ventricle and the left ventricle long axis in 3D transesophageal echocardiography image due to many visible partial cavities (the left ventricle (LV), the right ventricle (RV), the left atrium (LA), the right atrium (RA) and the aorta (Ao)). Also, in transesophageal echocardiography images the left ventricle is not the most prominent structure. In most of the cases, only the basal part of the LV is visible.

image and the left ventricle is not the most prominent one, mostly only the basal part of the left ventricle is visible (Fig. 4.1). Additionally, the presence of prominent structures of the mitral valve and aorta, and the highly rotational variability makes the location of the LV-LAX and the aortic valve difficult.

In comparison with other the state-of-the-art methods [10, 144], two novel features are presented in this work:

- **The localization of the aortic valve**. This feature is essential for the initialization of the multi-cavity segmentation method.
- **Tissue Detection**. A probabilistic and a structural tissue classification are combined to detect the LV-LAX, mitral valve and aortic valve. The probabilistic description of tissue avoids the misclassification of structures and palliates the effect of low contrast in US images.

4.2 Materials and Methods

Image acquisition

Real-time 3D TEE images were acquired with a central view of the mitral valve and including the aortic valve (Fig. 4.1 (b)), using a commercialy available Philips

iE33 xMatrix ultrasound system (Philips Healthcare, the Netherlands) with the X7-2t matrix-array TEE transducer. Patients were under general anesthesia in a supine position. The acquisition was performed on a group of 19 patients (age 78 $\pm$ 8 years) undergoing a Transcatheter Aortic Valve Implantation with a mean aortic valve thickness of 5.92 ± 1.69 mm. Images had slightly different sizes and resolutions, typically $261 \times 268 \times 212$ pixels with a resolution of $0.535 \times 0.532 \times 0.471$ mm. The study was approved by the institutional review board, and all patients gave informed consent.

Methods

Detection of the required structures is achieved by a Thin-Tissue Classification, a Left Ventricle Long Axis Detection and a Mitral Valve and Aortic Valve Detection. A flow chart of this approach is depicted in Fig. 4.2.

Thin-Tissue Classification.

The proposed thin-tissue detection, $TT(\mathbf{x})$, for a pixel $\mathbf{x}$ combines a probabilistic tissue characterization, $I_{GMM}(\mathbf{x})$, obtained from a mixture of Gamma distributions; the Hessian information to classify sheet-like local intensity structures, $S_{sheet}(\mathbf{x})$; and a gradient compensation $\Phi(\mathbf{x})$ to avoid the misclassification inside the myocardium as follows:

$$\begin{aligned} TT(\mathbf{x}) = \Phi(\mathbf{x}) \times S_{sheet}(I_{GMM}(\mathbf{x})) \\ \times I_{GMM}(\mathbf{x}) \end{aligned} \tag{4.1}$$

The mixture of Gamma distributions (GMM) is used to statistically characterize the blood and tissue in US images. This probabilistic tissue classification is used as a contrast enhancement operation, where I_{GMM} is the likelihood of a pixel being tissue. This way, the detection is confined to most likely tissue regions. The GMM is calculated by means of the Expectation-Maximization algorithm [95]. This method maximizes the log-likelihood function for hidden discrete random variables, $\mathbf{Z} = \{Z_i\}$. Let $\mathbf{X} = \{x_i\}, 1 \leq i \leq N$ be an identical independent distribution set of samples (pixel intensities) and x_i belongs to the distributions class j when $Z_i = j$. The GMM considers that these variables result from the contributions of J distributions:

$$p(x_i|\mathbf{\Theta}) = \sum_{j=1}^{J} \pi_j f_X(x_i|\Theta_j) \tag{4.2}$$

where $\mathbf{\Theta}$ is a vector of parameters of GMM (π_j, Θ_j) and Θ_j are the parameters of the probabilistic distribution function for a Gamma distribution (α_j and β_j) and $\sum_{j=1}^{J} \pi_j = 1$. The Expectation-Maximization algorithm is applied in the following way [151]:

1. An initial estimation of the hidden variables is obtained by k-means [55]. For each cluster, j parameters $\Theta_j^{(0)}$ and $\hat{\pi}_j^{(0)}$, are calculated from samples.

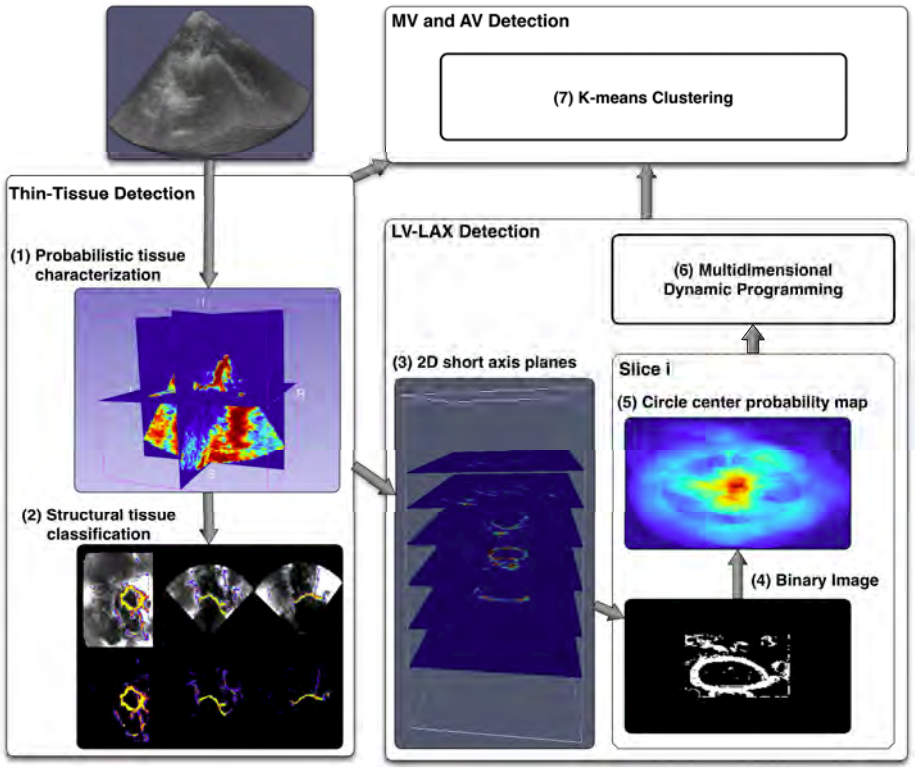

Figure 4.2: Workflow for the methodology to obtain the left ventricle long axis (LV-LAX), mitral valve (MV) and aortic valve (AV). A probabilistic tissue characterization (1) combined with a structural tissue classification is performed to enhance thin tissue structures such as the MV and AV (2). From the thin-tissue detection, several 2D planes are taken (3) to detect the LV-LAX. Applying the Hough transform for circles to each 2D binary image (4), a circle center probability map is generated (4). 3D dynamic programming determines the LV-LAX path (5) through the probability maps. Finally, the thin-tissue and the LV-LAX detection are used with a k-means clustering (7) to find the MV and AV location.

2. A Bayesian Inference step is performed to calculate $\gamma_{i,j}$ as:

$$\begin{aligned} p(Z_i = j|x_i, \mathbf{\Theta}^{(n-1)}) &= \gamma_{i,j} \\ &= \frac{\pi_j^{(n-1)} p(x_i|\Theta_j^{(n-1)})}{p(x_i|\mathbf{\Theta}^{(n-1)})} \end{aligned} \tag{4.3}$$

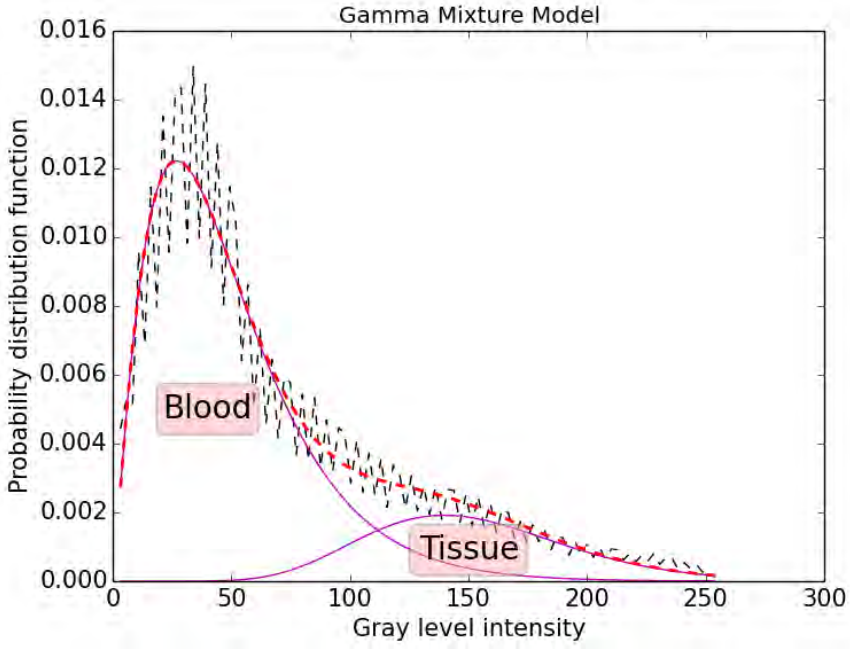

Figure 4.3: Probability distribution function for a patient data (dark dash-line) and the Gamma Mixture Model fitted using the Expectation-Maximization algorithm (red dash-line). The Gamma Mixture Model is used to distinguish between blood and tissue as it shows in bold-line.

3. The parameters for the mixture of Gamma distributions ($\hat{\alpha}_j, \hat{\beta}_j$ and $\hat{\pi}_j$) are estimated in the Expectation-Maximization step as follow:

$$\begin{aligned} log(\hat{\alpha}_j) - \psi(\hat{\alpha}_j) &= log\left(\frac{\sum_{i=1}^{N}\gamma_{i,j}x_i}{\sum_{i=1}^{N}\gamma_{i,j}}\right) \\ &\quad - \frac{\sum_{i=1}^{N}\gamma_{i,j}log(x_i)}{\sum_{i=1}^{N}\gamma_{i,j}} \end{aligned} \tag{4.4}$$

$$\hat{\pi}_j = \frac{1}{N}\sum_{i=1}^{N}\gamma_{i,j}, \qquad \hat{\beta}_j = \frac{1}{\hat{\alpha}_j}\frac{\sum_{i=1}^{N}\gamma_{i,j}x_i}{\sum_{i}^{N}\gamma_{i,j}} \tag{4.5}$$

where ψ is the digamma function.

4. Until an acceptable tolerance is reached, $||\mathbf{\Theta}^{(n)} - \mathbf{\Theta}^{(n-1)}|| < \epsilon$, an iterative

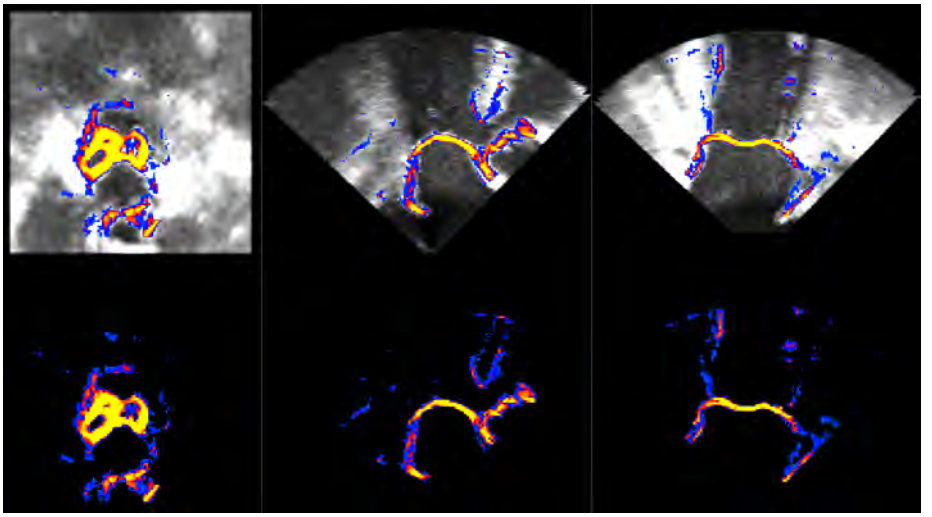

Figure 4.4: Example of the proposed thin tissue detector to illustrate the strong response inside the mitral valve and aortic vale, and the weak response in the myocardium. For clarity purpose, we decided to overlap the original image (top) and present the filter response with a dark background (bottom) using a cold-hot scale.

estimation of the parameters is performed repeating step 2 and 3.

As an example, in Fig. 4.3 the Gamma Mixture Model is fitted to patient data.

The gradient compensation, $\Phi(\mathbf{x})$, is defined as the average angle between gradient vectors in a neighborhood around pixel $\mathbf{x}$, as was done in Schneider et al. [129, eq. 1]:

$$\Phi(\mathbf{x}) = \frac{\sum_{a=1}^{J-1} \sum_{b=a+1}^{J} \arccos\left(\frac{\nabla I_{GMM}(\mathbf{x}_a) \cdot \nabla I_{GMM}(\mathbf{x}_b)}{|\nabla I_{GMM}(\mathbf{x}_a)||\nabla I_{GMM}(\mathbf{x}_b)|}\right)}{\sum_{j=1}^{J-1} j} \tag{4.6}$$

where ∇ is the gradient operator and J is the number of all neighboring voxels to $\mathbf{x}$. The gradient compensation is introduced to suppress non consistent gradients with the valves such as the myocardial boundaries. In particular, $\Phi(\mathbf{x})$ can be seen as an edge detector specialized in thin structures surrounded by blood. Finally, the structural thin tissue detector, S_{sheet}, was defined by Sato et al. [127] as follow:

$$S_{sheet}\{f\} = \begin{cases} |\lambda_3| \cdot \omega(\lambda_2; \lambda_2) \cdot \omega(\lambda_1; \lambda_3) & \lambda_3 < 0 \\ 0 & \text{otherwise.} \end{cases} \tag{4.7}$$

where the weighting function, ω, was defined as follows:

$$\omega(\lambda_s;\lambda_t) = \begin{cases} (1+\frac{\lambda_s}{\lambda_t})^\gamma & \lambda_t \leq \lambda_s \leq 0 \\ (1-\alpha\frac{\lambda_s}{\lambda_t})^\gamma & \lambda_t > \lambda_s > 0 \\ 0 & \text{otherwise.} \end{cases} \tag{4.8}$$

and $\lambda_1 \geq \lambda_2 \geq \lambda_3$ are the eigenvalues of the 3D hessian matrix for the image intensity I,

$$\nabla^2 I = \begin{bmatrix} I_{xx} & I_{xy} & I_{xz} \\ I_{yx} & I_{yy} & I_{yz} \\ I_{zx} & I_{zy} & I_{zz} \end{bmatrix} \tag{4.9}$$

Using the Hessian matrix $\nabla^2 I$ based on the second derivatives of a Gaussian with σ_f, allow us to control the thickness of interest. According to Sahasakul et al. [124] the mean thickness for the aortic valve is 1.42 ± 0.51 mm and 3.2 ± 1.52 mm for the mitral valve, so, to be sure to get a high response in this tissue without using any additional information about the patients, for example the mean mitral or aortic valve thickness, we decided to use a sheet thickness of 2 mm. Also, we set the parameters involved in the weighting function as it was suggested by Sato et al. [128], i.e $\sigma_f = 2\sqrt{2}$ mm , $\alpha = 0.25$ and $\gamma = 1$. Extensive analysis of the effects of parameters α and γ, can be found in [128].

The proposed thin-tissue detector is highly sensitive to the mitral valve and aortic valve leaflets, but also gives a low response inside the tissue and the myocardial boundaries (Fig. 4.4).

Left ventricle Long Axis Detection. The LV-LAX detection was performed using the Hough transform for detecting circular structures in 2D planes. Due to the presence of a circular thin-tissue response in the myocardial boundaries, we used the thin-tissue information as input to the Hough transform, instead of the 3D TEE image or its gradient [144, 10]. The response of the mitral valve itself was also circular and coaxial with the LAX, which further supports the Hough transform LV-LAX detection. To this end, the thin-tissue response was smoothed to remove the noise (with a Gaussian filter, $\sigma = 1.58$ mm), normalized and thresholded ($T_h = 0.0008$) in several 2D planes perpendicular to the acquisition axis (C-planes) taken 5 mm apart (Fig. 4.5).

The Hough transform is implemented by maintaining an accumulator array for centers of circles with a particular radius range. For example, if we set the radius range to [30 mm, 40 mm] the Hough transform will only detect circles with radius between 30 and 40 mm. This accumulator is used to create the probability map for circle centers, i.e the probability for a given position, (x, y), being the center of a circle with a particular radius r within the range. To reduce the dimensionality along the r dimension, a 2D circle center probability map (Fig. 4.5) is generated by taking the maximum probability value along the radius dimension. Finally, a 3D circle center probability map is created by stacking all the 2D circle center probability maps

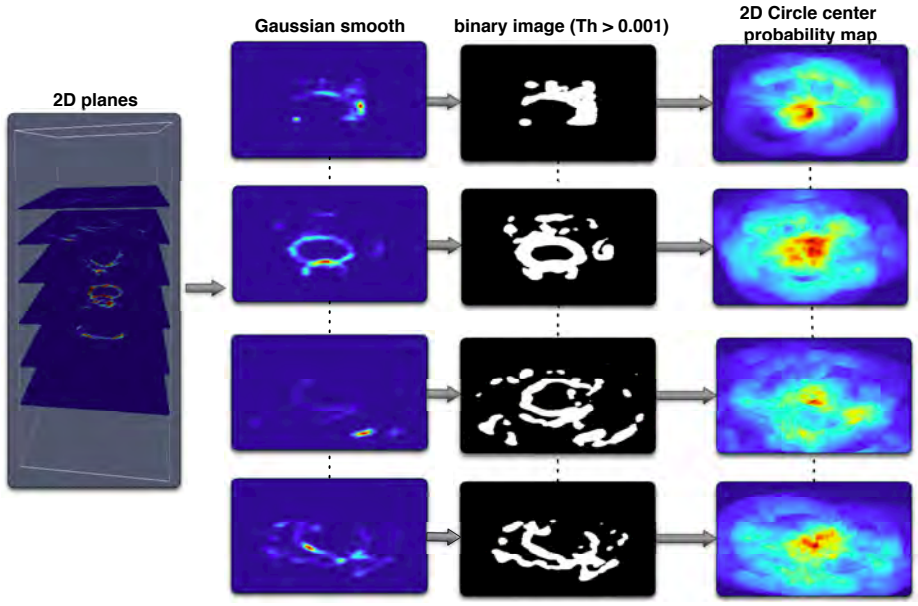

Figure 4.5: Complete workflow example to create a 3D circle center probability map by stacking the 2D circle center probability maps. First, a gaussian smooth is applied in each 2D plane to remove the noise and then they are thresholded previous normalization. Finally, a Hough transform for detecting circular structures in 2D is applied to get a 3D circle center probability map by stacking all the 2D circle center probability maps. The 3D circle center probability map is used to estimate the left ventricle long axis.

(Fig. 4.5). Due to the small part of the left ventricle present in the 3D TEE images and the interference of similar circular structures such as the aortic valve, we set the radius range to [30 mm, 40 mm] to maximize the response.

Finally, the LV-LAX is obtained as the path that maximizes the 3D circle center probability along the z direction. This path is calculated by means of multidimensional dynamic programming [139]. This approach was adopted due to its efficiency to find the best path through a N-dimensional cost image. After the detection, a straight line is fitted to the path along the z direction (Fig. 4.6).

For the estimation of the optimal parameters we assumed them to be dependent. We evaluated σ and T_h in the following range and increment denoted as $\{range; increment\}$: $\sigma = \{[1, 4.5]; 0.58\}$ mm and $T_h = \{[0.0007, 0.002]; 0.00014\}$. The full exploration of

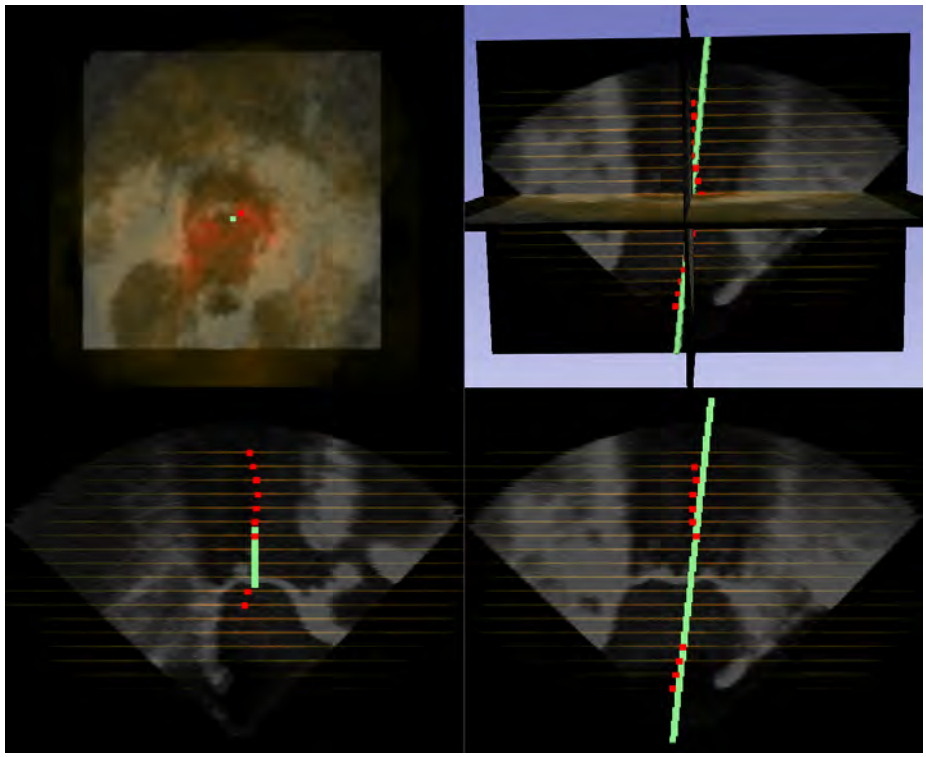

Figure 4.6: Left ventricle long axis (LV-LAX) detection in 3D image: The final 3D circle center probability map (orange), the path that maximize the 3D circle center probability map along the z direction (red) and the LV-LAX detected (green) are presented in a 3D view and in three orthogonal views.

these acquisition-dependent parameters space with the Mahalanobis distance resulted in the optimal parameters used for the LV-LAX detection. Also, a Leave-One-Out analysis for the nineteen patients reveals a low variability for these parameters (mean $\pm$ SD), 1.58 ± 0.5 mm for σ and 0.0008 ± 0.001 for T_h.

Mitral Valve and Aortic Valve Detection. The most relevant thin tissue in the 3D TEE images corresponds to the mitral valve, followed by the aortic valve. So, it is natural to think that the thin-tissue classification, which is highly sensitive to the mitral and aortic valve, provides good information about the mitral valve. Using this information and the LV-LAX detection, a profile containing the thin-tissue response

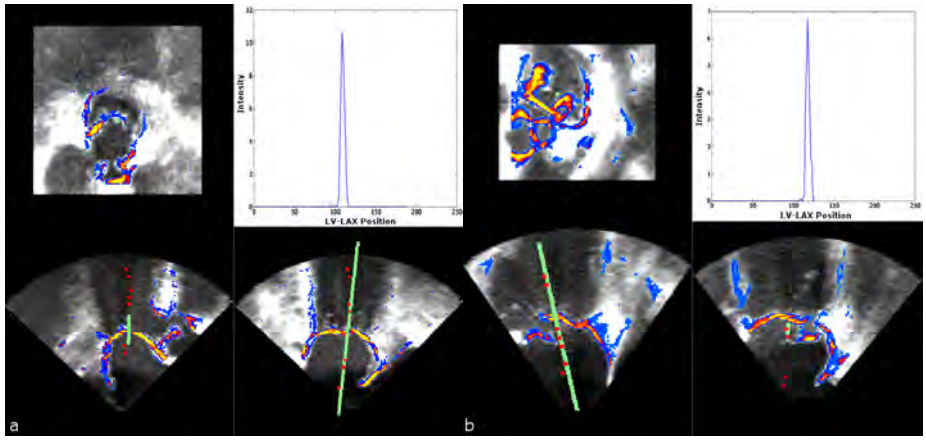

Figure 4.7: Example of the mitral valve detection for two patients (a, b). The mitral valve detection is performed building a profile of the thin tissue response (cold-hot scale) along the left ventricle long axis (green line). The maximum thin tissue intensity in the profile establishes the point where the left ventricle long axis is intersecting the mitral valve (upper right corner). The red dots correspond to the maximum probability path used to detect the left ventricle long axis.

along the LV-LAX is generated by taking the average in a neighborhood of radius of 2 pixels. The maximum value in the LV-LAX profile establishes the point where the LV-LAX is intersecting the mitral valve (Fig. 4.7). We defined the mitral valve point as the middle point around the mitral annulus, so the mitral valve detection is performed subtracting maximum normal tenting height to the position of the maximum value in the LV-LAX profile. According to Sonne et al. [136] and Watanabe et al. [157], we decided to use 3 mm as the maximum normal tenting length.

Moreover, it is possible to identify the mitral and aortic valve tissue using a k-means clustering [55] on the thin-tissue output with two classes, a maximum of 20 iterations and a threshold of 1×10^{-05} (Fig. 4.8 (a)) to separate tissue from blood/background. In particular, the center of gravity of the k-means output can be seen as the mitral valve center with a bias introduced by the presence of the aortic valve tissue. This bias is used to find the direction where the aortic valve must be with respect to the LV-LAX (Fig. 4.8 (b)). Finally, the aortic valve detection is performed taking the center of gravity of a new k-means clustering with two classes over the thin-tissue detection excluding the tissue around the mitral valve (with a radius of 15 mm) in the aortic valve direction (Fig. 4.8 (c)).

Evaluation. The accuracy for the automated detection was quantitatively evaluated against manually defined mitral valve/aortic valve landmarks and expert-drawn manual contours of the five cavities by using the following measures:

1. **Distance error**. The distance error was defined as the euclidian distance in millimeters between the manual landmarks and the automated detection for the mitral and aortic valve.
2. **Angle Error**. The angle error corresponds to the absolute difference in degrees for the LV-LAX direction and the direction of the aortic valve with respect to the mitral valve (Fig. 4.9).
3. **Dice's Coefficients**. The fully automated detection was evaluated in a segmentation framework [53] using the Dice's coefficient with respect to a manual segmentation for the left ventricle, the left atrium, the right ventricle, the right atrium and the aorta.

For agreement assessment a Bland-Altman analysis [12] was performed between the Dice's coefficient for manual and automated initialization.

For the manual landmarks, the expert was asked to provide the locations of the aortic valve, the Apex and four points around the mitral annulus. The segmentation ground truth was performed for all visible cavities in ten equally distributed 2D short axis views and 4 long axis views. The 2D contours were interpolated by B-splines and the control points were interactively manipulated by the observers to adapt the contours to the correct borders of the different cavities.

4.3 Results

In order to study the proposed thin-tissue detector, it was compared with the original approach to classify sheet structures [127]. The visual evaluation shows that the proposed thin-tissue detector overcomes most of the misclassification problems introduced by speckle and artifacts (Fig. 4.10). As a result of the probabilistic tissue characterization, the thin tissue response was improved inside the tissue and the misclassification in the blood was dramatically reduced. Also, the gradient compensation was introduced to reduce the misclassification inside the tissue. A visual example of the probabilistic tissue characterization and gradient compensation effects is shown in Fig. 4.11, where the effect of the probabilistic characterization in combination with the gradient compensation shows a much clearer definition of the boundaries of tissues.

A group of nineteen patients selected for aortic valve replacement were used in the present study for evaluation. In this population, the aortic valve tissue has different thickness according to the severity of each patient. The distance and angle error taking into account the normal mitral and aortic valve thickness was 6.3 ± 4.7 mm for the mitral valve where the normal mitral valve circumference is 100 mm [157], 13 ± 7.7 mm

for the aortic valve where the normal aortic valve circumference is 65 mm [64], 9.5 ± 7.2 degrees for the LV-LAX and 24.8 ± 18 degrees for the mitral valve/aortic valve direction. The thin-tissue detector showed its robustness to different valve thicknesses and the aortic valve tissue shows a high response for all patients when a normal thickness of 2 mm was assumed. However, in our experiments, the thin-tissue detection was used on a group of patients with a mean aortic valve thickness of 5.92 ± 1.69 mm. Using a custom aortic valve thickness for each patient (supervised case), the errors could be improved. The errors detected for the supervised case were 5.7 ± 3.5 mm for the mitral valve, 12 ± 7.6 mm for the aortic valve, 8.8 ± 3.6 degrees for the LV-LAX and 24.1 ± 14.9 degrees for the mitral valve/aortic valve direction (Fig. 4.12). To the best of our knowledge, the only ones who presented a similar error measure for the LV-LAX and the mitral valve were [144]. They measured the quality of the detected mitral valve plane as the projected signed distance between the mitral valve center detected and the manual mitral valve plane. Also, they measured the LV-LAX angle between the manual and detected LV-LAX in 3D transthoraxic echocardiography images for two different types of transducer (fast rotating ultrasound (FRU) and matrix array). They reported (Table 5. "MVP detection results for FRU and matrix data") an absolute mean error between the mitral valve center detected and the mitral valve plane of 6.07 ± 2.36 mm and 5.61 ± 3.11 mm for the FRU and the matrix transducer respectively. The LV-LAX angle error measured was 5.25 ± 3.15 degrees for the FRU and 5.95 ± 2.11 degrees for the matrix transducer. In our work the LV-LAX angle error is about 3 degrees than what is reported in [144]. This can be attributed to the different characteristics of the TEE images, with only partial visibility of the left ventricle and several other cavities in the field of view. Nevertheless, we still measured a similar mean error for the mitral valve.

As it was described in the previous section, the automated feature detection was evaluated within a fully automated segmentation framework. For comparison purposes, the same evaluation was performed using manual landmarks. The segmentation results (Fig. 4.13) showed no statistically significant differences between manual and automated initialization in a paired t-test ($p > 0.05$). This was the case both for the normal valve thickness and for the custom valve thickness. These results were confirmed by the small bias between manual and automated initialization detected in the Bland-Altman analysis (Fig. 4.14 and Fig. 4.15). However, the results show an increase in the variance for the right ventricle, the right atrium and aorta segmentation due to the error increase for mitral valve/aortic valve direction. The mitral valve/aortic valve direction provides the physical orientation of the right ventricle with respect to the left ventricle in the multicavity segmentation framework.

The segmentation algorithm may be more sensitive to initialization differences due to the absence of big parts of these cavities in the field of view. Nevertheless, although the absolute detection errors of the features seem considerable, their influence on the initialization is not statistically significant and the agreement results confirm that the proposed automatic initialization can be used instead of the manual initialization.

4.4 Discussion

Thin-Tissue Detection

The thin-tissue detector is a crucial stage in the proposed framework which is necessary to detect the mitral and aortic valve, and LV-LAX in 3D TEE images. Due to the small part of the cardiac anatomy that is covered in 3D TEE images and the presence of different circular structures, it is impossible to use the original image or an edge operator to detect the LV-LAX with an acceptable accuracy. In our experiments, the thin-tissue detector showed its robustness to different thickness and the aortic valve tissue was successfully detected for all patients using a thickness of 2 mm. However, an improvement can be done using a custom aortic valve thickness for each patient (Fig. 4.12 and Fig. 4.13).

Left Ventricle Long-Axis Detection

The LV-LAX detection is based on the Hough transform for circles which assumes the presence of circular shapes in each 2D plane perpendicular to the acquisition axis. However, in 3D TEE images two main problems appear: first, only a small part of the cardiac anatomy is covered and second, the acquisition axis is not aligned with the real LV-LAX. Hence, a fuzzy Hough transform approach [113] combined with the probabilistic tissue characterization seems to be more suitable to find the LV-LAX. In practice, the Hough transform is capable of dealing with imperfect and incomplete circle structures. We decided to use the standard Hough transform instead of the fuzzy approach because it is simpler and the LV-LAX angle error of 9 degrees is acceptable for initialization purpose.

Mitral Valve and Aortic Valve Detection

In this study, the most relevant thin tissue corresponds to the mitral valve, followed by the aortic valve. The mitral and aortic valve detection are based on the assumption that the center of gravity is close to the mitral valve but biased towards the aortic valve. However, the method might encounter problems in pathological cases where this bias is altered by other structures like left pulmonary veins. In particular, this is the case for the patient detected as outlier in the aortic valve error (AV) and the mitral valve/aortic valve angle error (MV-AV and MV-AVc) (Fig. 4.12). Also, this patient was detected as the biggest outlier for the aortic valve error taking into account a custom aortic valve thickness (AVc). In this case, the presence of other thin tissue structures are introducing a bias in the opposite direction to the aortic valve (Fig. 4.16). This was the only case where this assumption failed, but, this topic needs to be further investigated. This would be a subject for further research on aortic valve detection. A specific possibility is to exploit the tubular shape of the left ventricular outflow tract and aorta.

Potential for clinical applications/utility

The segmentation and tracking of different cardiac structures, such as the left ventricle or the mitral valve hinge points (MVHP), have an important role to treat different kinds of pathologies. However, accurate and reliable measurements for volumetric analysis and functional assessment heavily relies on user interaction. The results obtained in this work (the the mitral valve, the left ventricle long axis and the aortic valve location location) can be efficiently used for the initialization of segmentation methods [53, 129]. Additionally, this work leads to extensions for automatic detection and tracking of the MVHP. The mitral annular motion is useful in the evaluation of global and regional LV functions and it is also an important parameter in the diagnosis of annular diseases and LV disorders [34]. Besides, the proposed thin-tissue detector offers a suitable way to detect the mitral and aortic valve tissue which can be used directly as an initial valve segmentation and lay the ground for new automatic mitral valve segmentation approaches in 3D TEE images.

4.5 Conclusions

A new automatic approach to detect the LV-LAX, the mitral valve and aortic valve in 3D TEE images is proposed. This approach is based on a probabilistic and structural tissue classification, the Hough transform for circles and multidimensional dynamic programming. For accuracy and agreement assessment, the proposed method was evaluated in 19 patients with respect to manual landmarks, and as initialization of a multi-cavity segmentation approach for the left ventricle, the right ventricle, the left atrium, the right atrium and the aorta using the dice's coefficient with respect to manual segmentation.

The aortic valve tissue shows a high response for all patients using a valve thickness suggested in the literature [124] for normal patients. The median distance error obtained for the automated detection using this normal valve thickness was 6.3 ± 4.7 mm for the mitral valve and 13 ± 7.7 mm for the aortic valve. Besides, the median angle error detected was 9.5 ± 7.2 and 24.8 ± 18 degrees for the LV-LAX and mitral valve/aortic valve direction, respectively. However, the median and variance error could be improved taking into account a custom aortic valve thickness for each patient. Using an aortic valve thickness similar to the patient, the median distance error was 5.7 ± 3.5 mm for the mitral valve, 12 ± 7.6 mm for the aortic valve, 8.8 ± 3.6 degrees for the LV-LAX and 24.1 ± 14.9 degrees for the mitral valve/aortic valve direction. The segmentation results showed no statistically significant differences between manual and automated initialization in a paired t-test ($p > 0.05$). Additionally, small biases between manual and automated initialization were detected in the Bland-Altman analysis (bias, variance): left ventricle $(-0.04, 0.11)$, right ventricle $(-0.08, 0.19)$, left atrium $(-0.02, 0.06)$, right atrium $(-0.10, 0.22)$ and aorta $(-0.07, 0.17)$ for a normal valve thickness; and left ventricle $(-0.04, 0.10)$, right ventricle $(-0.07, 0.18)$, left

atrium $(-0.01, 0.03)$, right atrium $(-0.04, 0.13)$ and aorta $(-0.05, 0.14)$ for a custom valve thickness. These results show that the proposed approach provides a robust and accurate detection to initialize a multi-cavity segmentation approach without any user interaction.

Acknowledgements

This work was partially supported by the Ministerio de Educación, Ciencia y Tencología (MECyT) de Argentina, Fundación Carolina de España, Universidad de Valladolid (FPI-Uva) and Ministerio de Ciencia e Innovación de España for grant TEC 2013-44194.

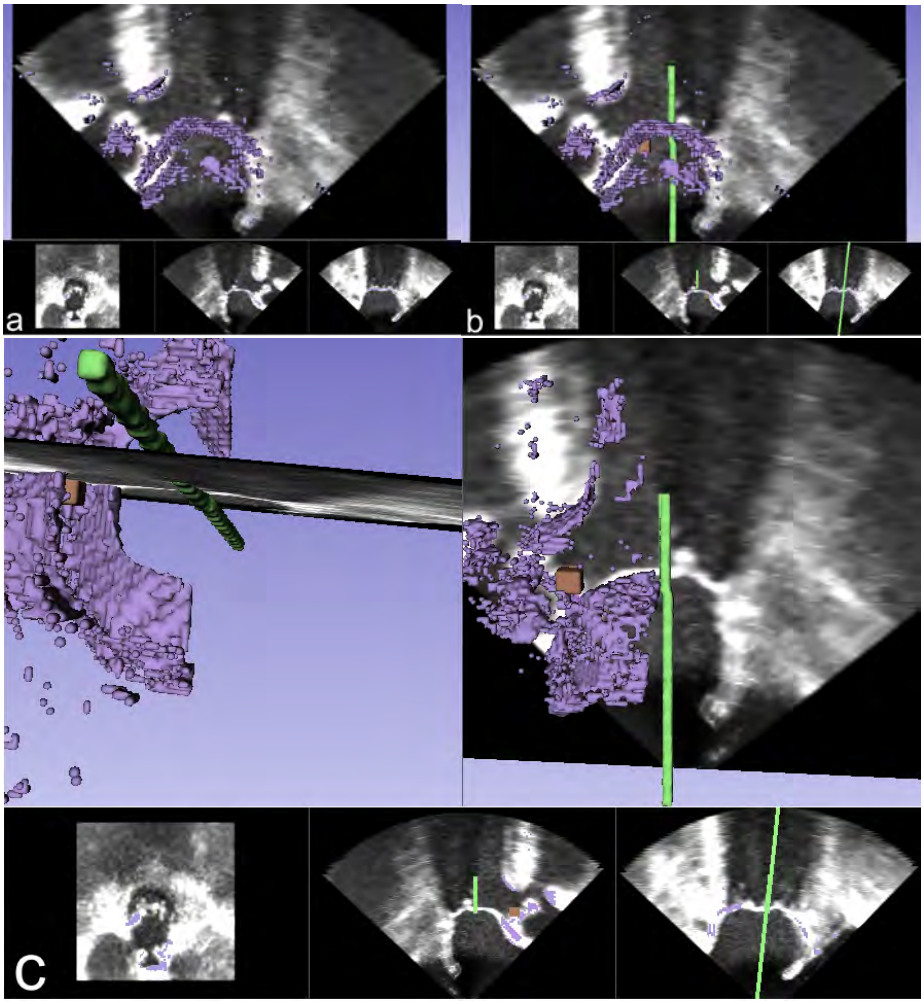

Figure 4.8: Example for the aortic valve detection. The aortic valve (brown cube) (c) is detected using a k-means clustering on the thin-tissue output with two classes to separate tissue from blood/background (a) and excluding the tissue around the mitral valve (with a radius of 15 mm) and the tissue in the opposite direction to the aortic valve (c). The aortic valve direction is detected using the center of gravity for the k-means output (brown cube) (b).

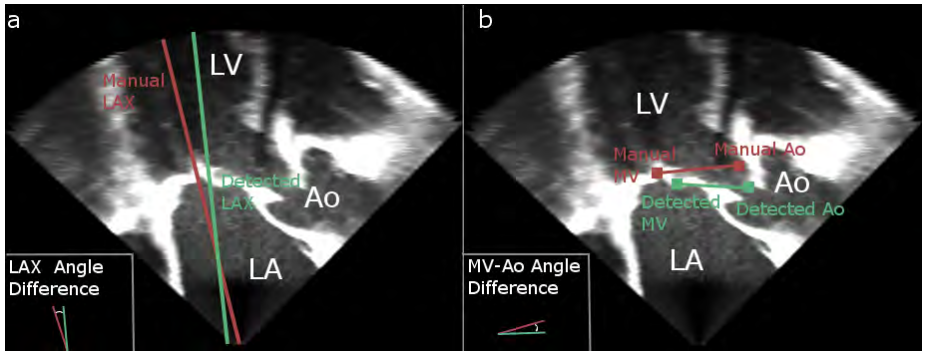

Figure 4.9: Left ventricle long axis direction differences ((a) LAX Angle Difference) and mitral valve/aortic valve direction differences ((b) MV-Ao Direction) between manual (red) and automatic detection (green).

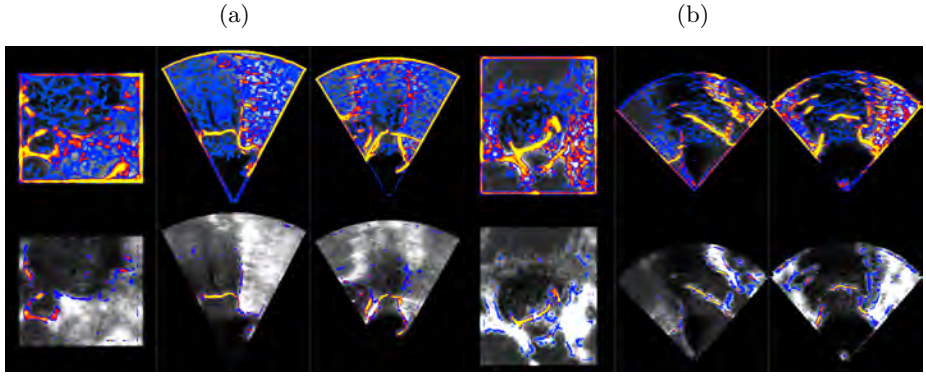

Figure 4.10: Misclassification problems introduced by speckle and artifacts in the original thin-tissue detector (top) and the thin tissue-detector proposed to overcome these misclassification problems (bottom) for two 3-D images (a, b) in three orthogonal views.

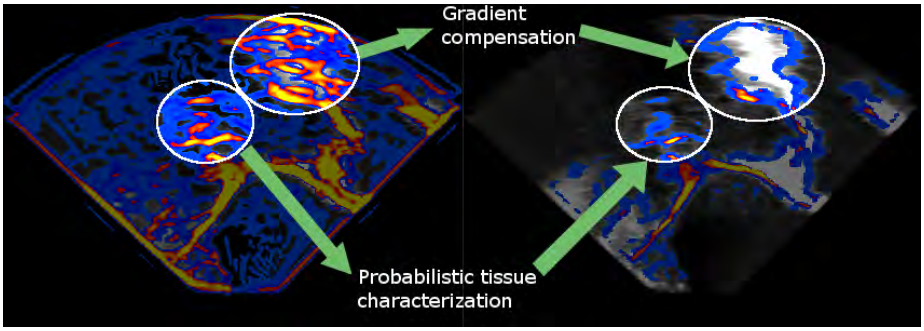

Figure 4.11: Effect of the probabilistic tissue characterization and gradient compensation (right) with respect to the original tissue classification (left) for 3D TEE image. For clarity purpose, the original thin tissue and the proposed thin tissue response are presented in a cold-hot scale.

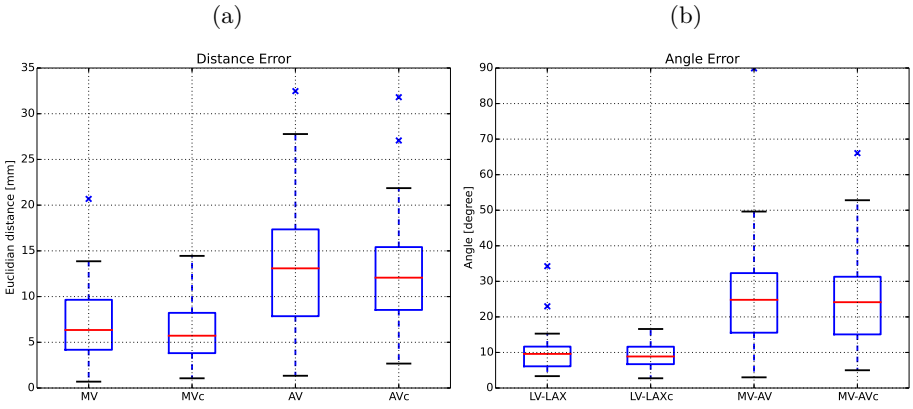

Figure 4.12: Distance and angle error between manual landmarks and automated detection for mitral valve (MV), aortic valve (AV), left ventricle long axis direction (LV-LAX) and mitral valve/aortic valve direction (MV-AV) in a group of nineteen patients taking into account a normal aortic valve thickness and a custom aortic valve thickness for each patient (MVc, AVc, LV-LAXc and MV-AVc).

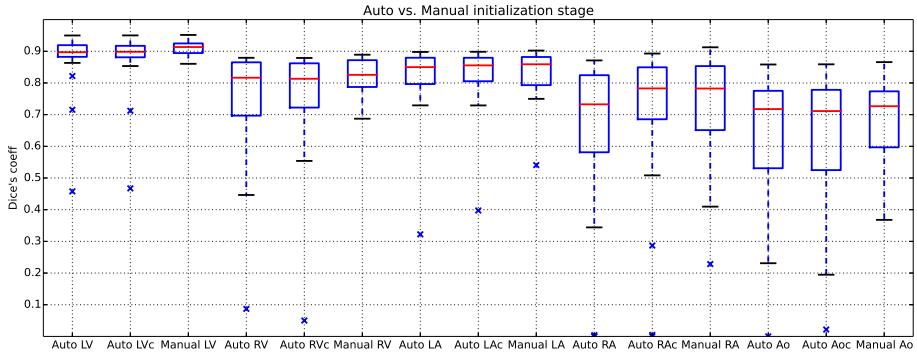

Figure 4.13: Dice's coefficient results for the segmentation using a manual and automatic initialization for the left ventricle (LV), right ventricle (RV), left atrium (LA), right atrium (RA) and aorta (Ao) in a group of nineteen patients taking into account a normal aortic valve thickness and a custom aortic valve thickness for each patient (LVc, RVc, LAc, RAc, Aoc).

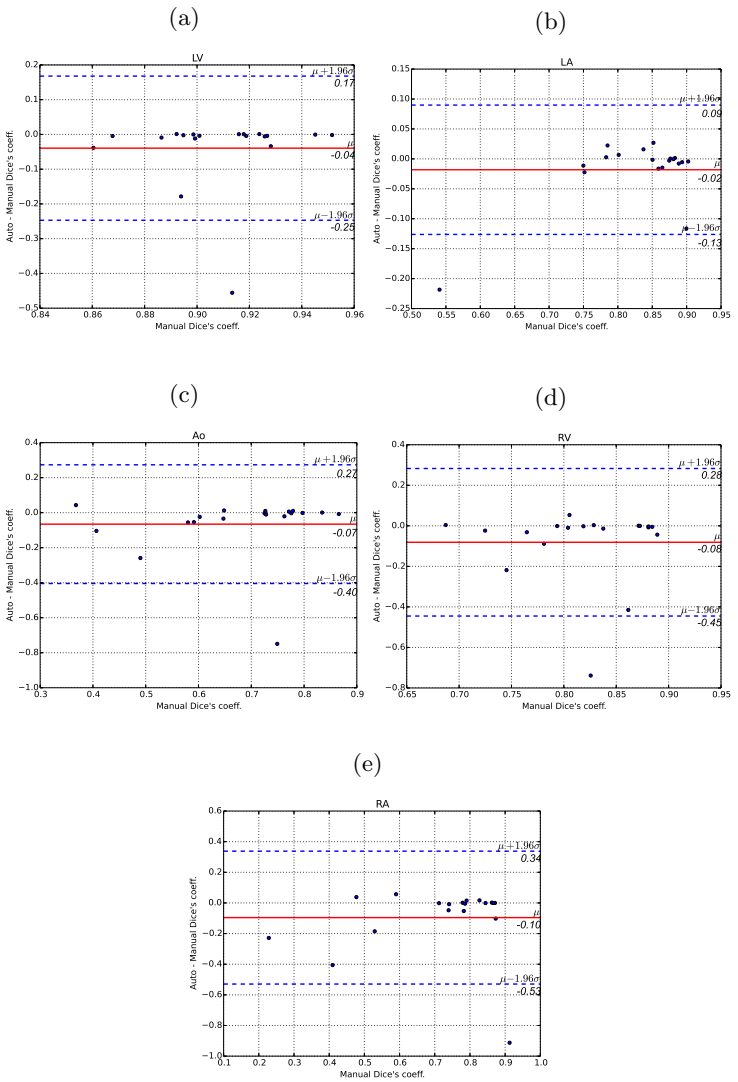

Figure 4.14: Bland-Altman plots of Dice's coefficients of manually initiated detection (Manual) and of automatically initiated detection (Auto) for the five segmented structures: the left ventricle (LV), right ventricle (RV), left atrium (LA), right atrium (RA) and aorta (Ao). Dice's coefficients are computed from comparison with expert-defined manual contours in a group of nineteen patients taking into account a normal aortic valve thickness.

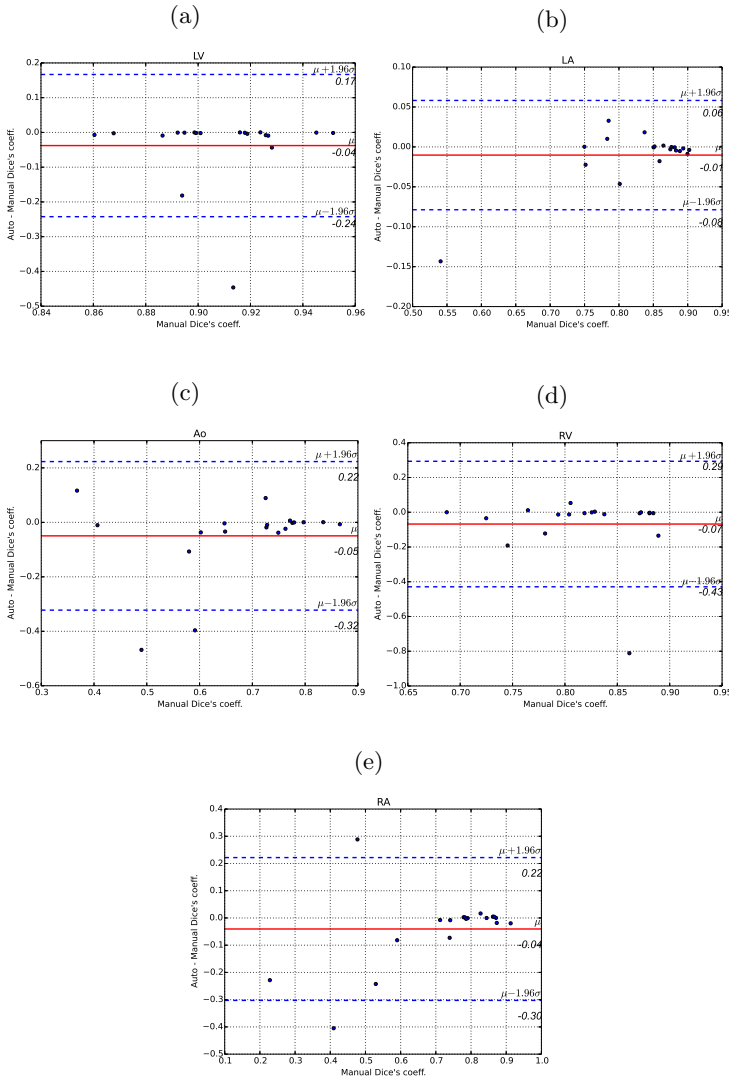

Figure 4.15: Bland-Altman plots of Dice's coefficients of manually initiated detection (Manual) and of automatically initiated detection (Auto) for the five segmented structures: the left ventricle (LV), right ventricle (RV), left atrium (LA), right atrium (RA) and aorta (Ao). Dice's coefficients are computed from comparison with expert-defined manual contours in a group of nineteen patients taking into account a custom aortic valve thickness for each patient.

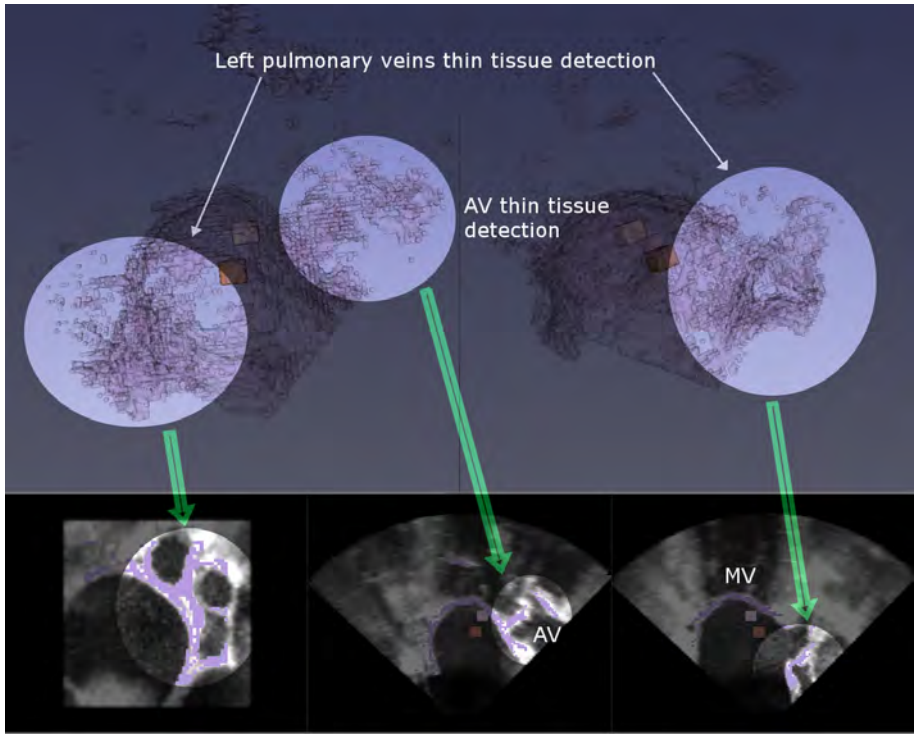

Figure 4.16: Example of a pathological case to detect the aortic valve (AV). In this example, the presence of the left pulmonary veins are introducing a bias in the opposite direction to the AV with respect to the mitral valve (MV).

Chapter 5

A transoesophageal echocardiographic image acquisition protocol for wide-view fusion of three-dimensional datasets to support the atrial fibrillation catheter ablation

This chapter has been published as:
B. Ren, H.W. Mulder, **A. Haak**, M. van Stralen, T. Szili-Torok, J.P.W. Pluim, M.L. Geleijnse, J.G. Bosch, A transoesophageal echocardiographic image acquisition protocol for wide-view fusion of three-dimensional datasets to support the atrial fibrillation catheter ablation, *J Interv Card Electrophysiol* 37, no. 1, 21-6, (2013).

Abstract
Purpose: To propose a transoesophageal echocardiography (TOE) image acquisition protocol which provides a systematic manner of acquiring a minimal number of overlapping 3D TOE datasets allowing the reconstruction of a wide 3D view of the left atrium (LA) with anatomical landmarks important for the atrial fibrillation catheter ablation.
Methods: In eight cardiac surgical patients, 3D TOE datasets were acquired with a 6-step protocol. In the protocol, Step 1 aims to acquire the central view of the mitral valve (MV), aortic valve (AV) and left atrial appendage (LAA). Step 2 was developed to acquire the left pulmonary veins (PVs) and Step 3 to acquire the right PVs. Step 4, 5 and 6 were developed to create sufficient overlap between different datasets. 3D TOE datasets were registered and fused manually in end diastole.
Results: The image acquisition protocol was feasible in all patients. In the fused 3D dataset, a wide 3D view of the LA is shown and left and right PVs could be seen simultaneously. The LAA, MV, AV, and fossa ovalis (FO) were visualised clearly in the 3D TOE datasets. The PV ostia, which are located at the edges of the 3D datasets, suffered more from the artefact of echo loss. The volume overlaps between neighbouring TOE datasets were 50–75%.
Conclusion: The major part of the LA anatomy incorporating the PVs, LAA, MV, AV and FO as important anatomical landmarks can be reconstructed by registering and fusing 3D datasets acquired with the 6-step TOE image acquisition protocol.

5.1 Introduction

Atrial fibrillation (AF) is increasingly treated by catheter ablation, during which circumferential lesions are created around the left and right pulmonary vein (PV) ostia to isolate the PVs, thus eliminating the triggers initiating AF [88]. To support the procedure, imaging the left atrium (LA) along with the PVs, left atrial appendage (LAA) and mitral valve (MV) is important. Several imaging modalities are commonly applied. Rotational angiography [105], computerized tomography (CT), or magnetic resonance imaging (MRI) is often used before the ablation procedure, and the pre-acquired CT or MRI images are segmented and registered by the electro-anatomical surface mapping (EAM) system to the real time mapping space during the procedure [38]. However, the substantial dose of ionizing radiation of CT scans, rotational angiography and fluoroscopy required by the catheter ablation causes important delayed effects on patients [123, 76, 109]. As AF ablation procedures often need to be repeated, there is a consensus that every attempt should be taken to minimize radiation exposure [23]. Additionally, CT and MRI are of cumbersome logistics and high cost. Up till now, the contribution of pre-interventional CT or MRI to the efficacy of the AF catheter ablation procedure is still under debate.

Transoesophageal echocardiography (TOE) is used routinely to exclude LAA thrombus a few days or immediately before the catheter ablation. The anatomy of the LA and adjacent structures can be visualised in high resolution 2D and 3D TOE images [41, 63, 145]. However, the field of view of one single full volume 3D TOE dataset is not large enough to visualise all important cardiac structures simultaneously, and this holds particularly true for the PVs which are located at the left and right edges of the LA. In theory, it is possible to reconstruct a 3D anatomical surface of the LA using overlapping and fused 3D TOE datasets, eliminating the need for pre-interventional CT or MRI [137]. In this study, we propose a stepwise TOE image acquisition protocol which provides a fast and systematic manner of acquiring a minimal number of overlapping 3D TOE datasets which allows the reconstruction of a wide 3D view of the LA along with all important anatomical landmarks.

5.2 Methods

Study population and ultrasound system

In eight cardiac surgical patients (five men, aged 59 $\pm$ 14 years), intraoperative TOE was performed with the iE33 xMatrix ultrasound system (Philips Medical System, the Netherlands) with the X7-2t matrix-array transducer under general anaesthesia. The protocol was approved by the institutional review board.

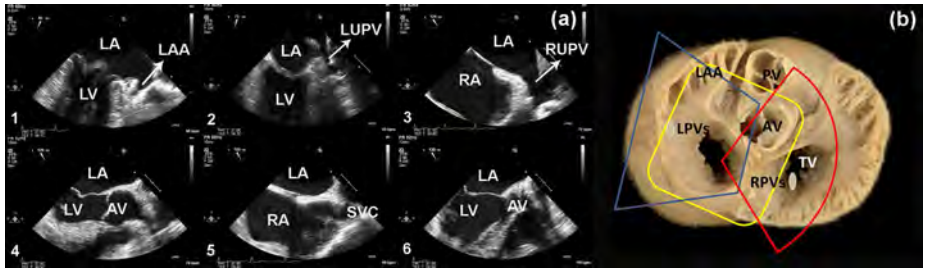

Figure 5.1: A, two-dimensional transoesophageal echocardiography reference views of the 6-step image acquisition protocol. 1, the mitral commissural view; 2, the superior commissural view including the left upper pulmonary vein; 3, the modified bicaval view including the right upper pulmonary vein; 4, the aortic valve long axis view; 5, the midpoint view between the aortic valve long axis and bicaval views; 6, Further left to the aortic valve long axis view. B, cardiac structures acquired in the 3D datasets of Step 1 (yellow), Step 2 (blue) and Step 3 (red). The grey areas represent the area of the pulmonary vein ostia projected to the cross-section of the anatomical view. AV, aortic valve; LA, left atrium; LAA, left atrial appendage; LPVs, left pulmonary veins; LUPV, left upper pulmonary vein; LV, left ventricle; MV, mitral valve; PV, pulmonary valve; RA, right atrium; RPVs, right pulmonary veins; RUPV, right upper pulmonary vein; SVC, superior vena cava; TV, tricuspid valve

Transoesophageal echocardiography image acquisition protocol

The stepwise TOE image acquisition protocol with the rotation angle and probe manipulation is depicted in Table 1. All acquisitions are performed at the mid-oesophageal level. All structures of interest are first visualised in 2D images of each step (Figure 1A); then, the corresponding 3D datasets are acquired according with one cardiac cycle with a proper depth and the largest volume size to include the structures of interest. The 2D reference views and 3D datasets are acquired according to the ASE guidelines for performing the intraoperative TOE examination [130] and the latest EAE/ASE recommendations for image acquisition and display using 3D echocardiography [77]. In the protocol, Step 1 aims to acquire the central view of the MV, LAA and AV; Step 2 was developed to acquire the left PVs and Step 3 to acquire the right PVs (Figure 1B). Step 4, 5 and 6 were developed to create sufficient overlap between different datasets for image registration and fusion.

Table 5.1: The 6-step transoesophageal echocardiographic image acquisition protocol.

Step	Angle	Manipulation of the probe
1	60-80˚	First position the probe at the mid-oesophageal level at 0˚and retroflex the probe tip slightly to develop the 4-chamber view; rotate the angle forward to 60–80˚to develop the imaging plane parallel to the line intersecting the two commissures of the mitral valve [130].
2	60-80˚	From Step 1, withdraw the probe by 1–2 cm and turn it anti-clockwise about 15 o to visualise the left PVs.
3	100-130˚	Turn the probe back to the position in Step 1; rotate the angle forward to 100–130 o and turn the probe clockwise until the left atrium appears in the upper part of the screen and right atrium in the lower part with the superior vena cava at the right side to develop the bicaval view; turn the probe further clockwise about 15˚to reveal the right upper pulmonary vein at the right side of the screen and the superior vena cava is not seen.
4	120-160˚	From Step 3, rotate the angle to 120–160 ˚and turn the probe anticlockwise until the left ventricular outflow tract, aortic valve and proximal ascending aorta line up and the aortic valve appears in the centre of the image[130].
5	120-160˚	From Step 4, turn the probe clockwise by about 40˚, half way back to the 2D view of Step 3.
6	120-160˚	Turn the probe back to the position in Step 4; turn the probe further anticlockwise about 20˚.

Image registration

To construct a wide 3D view of the LA including the left and right PVs, the datasets of the six different steps were registered manually in a pairwise fashion in end diastole in two stages. Firstly, three landmarks were indicated in each dataset. For all datasets, the tip of the pyramidal 3D datasets and the coaptation point of the aortic valve (AV) leaflets were used as soft landmarks. Depending on the view, the coaptation point of the MV leaflets or the fossa ovalis (FO) was chosen as the third landmark. Since corresponding time frames were registered, only rotational and translational differences between the volumes were expected and therefore a rigid transformation model was used. The landmarks were registered by a closed-form least squares optimization algorithm [65]. Secondly, the image alignment was improved manually by rotating and translating one volume with respect to the other, viewing the result in all three orthogonal views. Once an adequate transformation was found, the datasets were fused with maximum intensity fusion. Severe near-field artefacts were removed by cropping the ultrasound pyramid before the image fusion.

5.3 Results

The clinical characteristics of all patients are depicted in Table 2. The image acquisition protocol was feasible in all eight patients and in total 48 3D TOE datasets were acquired. For all full volume 3D datasets, the average volume size was 91 °(lateral width) x 93 °(elevation width). The average volume rate of the 3D TOE datasets was six volumes per second.

The cardiac structures captured in the 3D datasets of each step and the corresponding image qualities are shown in Table 3. The main 3D artefact was the echo loss. In general, the LAA, MV, AV, and FO were always visualised with good image quality, i.e. visualised clearly and distinguished easily in the 3D datasets without artefacts of echo loss. The ostia of the PVs, which are located at the edges of the 3D datasets, suffered more from the artefact of echo loss.

Three orthogonal views of a fused 3D dataset and its orientation with respect to the heart are shown in Fig.2. The different colours represent the different steps. An example of a fused 3D TOE dataset in different orientations revealing the important anatomical structures is shown in Fig.3. It is clearly shown that the extension of the field of view gives a wider 3D view of the LA than the 3D TOE dataset of a single step does. Using the described protocol, the average volume overlap between neighboring TOE datasets ranges from 50–75%.

Table 2 Clinical characteristics of the patients (n = 8).

No.	Age	Gender	BSA (m^2)	LA size*	Surgical indications	Rhythm	Hypertension	HR (bpm)†	BP (mmHg)†
1	76	F	1.96	Severely enlarged	Severe MR	Sinus	No	66	110/65
2	67	F	1.78	Normal	Severe MR	Sinus	Yes	87	115/60
3	30	M	1.99	Severely enlarged	Severe MR	Sinus	No	50	115/65
4	58	M	2.15	Normal	MI	Sinus	Yes	64	135/75
5	56	M	2.04	Normal	MI	Sinus	Yes	46	130/80
6	58	M	1.90	Severely enlarged	Paravalvular leak after mitral valve repair	Sinus	No	57	80/55
7	61	F	1.77	Severely enlarged	Severe MR, ventricle aneurysm,	Sinus	Yes	56	125/65
8	68	M	2.04	Severely enlarged	Severe MR, MI, tricuspid regurgitation	Pacemaker	Yes	60	125/65

BSA, body surface area; LA, left atrium; HR, heart rate; BP, blood pressure; F, female; M, male; MR, mitral regurgitation; MI, myocardial infarction.

*The grading of the LA size was based on LA volume index (LA volume divided by BSA) according to the ASE recommendations for chamber quantification.[19]

†Heart rate and blood pressure were measured instantaneously during image acquisition.

Table 3 Cardiac structures in and image quality of the 3D TOE datasets.

Step	Cardiac structures in 3D TOE datasets	Image quality
1	MV, AV, LAA	Good* in 8 patients.
2	part of MV, part of AV, LAA, ostia of left PVs	MV, AV and LAA: good* in 8 patients; left PVs: two ostia could be seen in 2 patients, one ostium could be seen in 2 patients, poor† in 4 patients.
3	part of AV, FO, ostia of right PVs	AV and FO: good* in 8 patients; right PVs: one ostium could be seen in 5 patients, poor† in 3 patients.
4	MV, AV	Good* in 8 patients.
5	part of AV, FO	Good* in 8 patients.
6	MV, AV	Good* in 8 patients.

TOE, transoesophageal echocardiography; MV, mitral valve; AV, aortic valve; LAA, left atrial appendage; PV, pulmonary vein; FO, fossa ovalis.

*Good: visualised clearly and distinguished easily in the 3D datasets without artefacts of echo loss.

†Poor: indistinguishable due to too much echo loss.

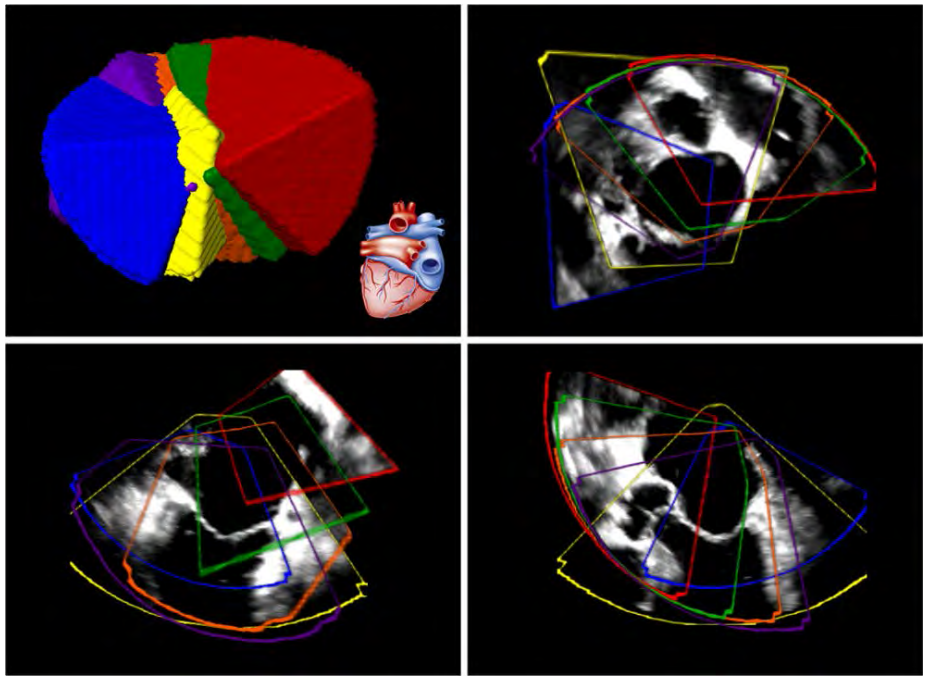

Figure 5.2: The orientation of 3D TOE datasets of each step with respect to the heart (the left upper quadrate) and orthogonal views of a fused 3D TOE dataset. Step 1 (yellow); Step2 (blue); Step 3 (red); Step 4 (orange); Step 5 (green); Step 6 (purple).

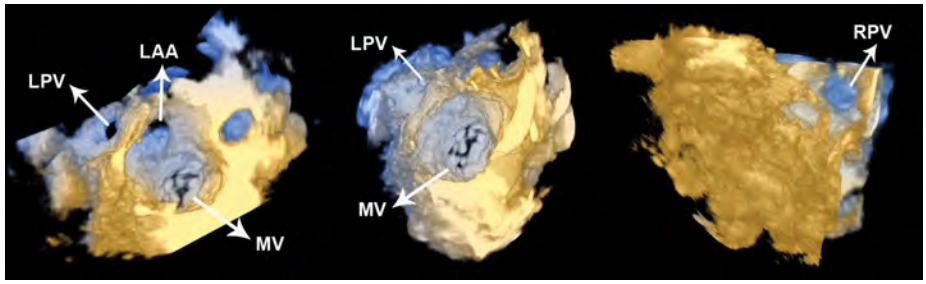

Figure 5.3: An example of a fused 3D TOE dataset and important cardiac structures are indicated. LAA, left atrial appendage; LPV, left pulmonary vein; MV, mitral valve; RPV, right pulmonary vein. Since the complete dataset was fused from six 3D TEE datasets, some part of the fused dataset was cropped to reveal the important anatomic landmarks.

5.4 Discussion

In this study, we developed a systematic TOE image acquisition protocol with which six 3D TOE datasets were acquired and fused, providing a much wider reconstructed 3D view of the LA, incorporating the PVs, LAA, MV and AV. The protocol provides an important step towards using the pre- and/or intra-interventional 3D TOE to generate an anatomical map of LA for AF catheter ablation, eliminating the need for pre-interventional CT or MRI.

The six steps of the protocol were chosen based on their feasibility and reproducibility in acquiring 3D TOE datasets which provide sufficient overlap among each step for registration.

Of all important anatomical landmarks, the LAA, MV, and AV were always of good image quality because they are located in the relative central part of the pyramidal 3D TOE datasets. Although the thin membranous area of the FO is likely to suffer from echo loss, its appositional muscular rim (limbus) can be distinguished easily in the 3D datasets. Since the PVs are adjacent to the lung and the 3D datasets are likely to suffer from the echo loss, the ostia of the PVs were less distinguishable than other cardiac structures, especially in those of inferior general image quality. The typical arrangement of four distinct pulmonary venous ostia is present in 20–60% of subjects, but it is also common to find the presence of a short or long common venous trunk on the left side, and supernumerary veins on the right side [71], The variances in the PVs' anatomy greatly influence the success rate of the AF catheter ablation if the variant PVs are treated inadequately. In this study, a short common venous stem of the left PVs was revealed in the 3D TOE datasets of one case and three right PVs in another case.

In this study, five patients had had severely enlarged LA due to severe mitral regurgitation. The relative positions of the PVs, lung and probe might be altered in this situation, which may compromise the general image quality. This might also be the case for patients with AF because they usually have an enlarged LA [9, 61]. In addition, the patients' position during the acquisition may also influence the general image quality as the position of the heart relative to the lung might be changed. The lateral decubitus position tends to rotate the heart to the left of the sternum [94] and towards the chest wall. In this study, all patients were supine during the image acquisition.

Limitations

Although the major part of the LA including important anatomical structures was reconstructed successfully by registering the 3D TOE datasets, it was still not possible to reconstruct the whole LA. The roof of the LA was always lost in the 3D datasets, because the currently used matrix TOE probe (Philips X7-2t) is not capable of visualising the structures in the near field of the ultrasound beam. We tried to acquire 3D TOE datasets in the transgastric view in which the LA roof lies in the far field of the ultrasound beam, but the spatial resolution dropped substantially and essential structures could hardly be distinguished. Nevertheless, we intend to carry out the 3D reconstructions also using images acquired by the Philips S8-3t micro-TOE probe which is of higher frequency (up to 6 MHz). According to our primary experience, the micro-TOE probe is able to visualise the LA roof in adults.

In this study, all 3D TOE datasets were registered manually, which requires specific expertise and relatively long time. However, the manual registration time consumption highly depends on the image quality of the 3D TOE datasets which determines the recognisability of the anatomical landmarks. Currently, we are developing an automatic registration method which will eliminate manual input and speed up the registration process. The automatic registration algorithm will take much less time than the manual registration and can be further incorporated into the ultrasound system, thus allows an on-line reconstruction. Therefore, the wide-view fused 3D TOE dataset can be made available to the electrophysiology physician during the ablation procedure.

All single full volume 3D datasets were free from 3D stitching artefacts because they were acquired from only one cardiac cycle, but as a result, the volume rates were very low. This limits temporal alignment and results in different positions of fast moving cardiac structures, thus influencing the quality of the fused dataset negatively. To acquire full volume 3D datasets from two or four cardiac cycles can greatly improve the volume rate (up to about 32 volumes per second) at the cost of longer acquisition time and stitching artefacts. Additionally, it should be noticed that the patients included in this study were under general anaesthesia and in non-anaesthetised patients stitching artefacts might be a bigger problem. These issues need to be investigated further.

Future clinical implications

The wide-view fused 3D TOE dataset will be very useful to reconstruct the LA anatomy; the segmented 3D surface could be imported to the EAM system. Additionally, intra-interventional 2D echocardiographic images can be matched to the pre-interventional 3D TOE images, preventing cumbersome multi-modality registration to CT or MRI images. The wide-view fused 3D TOE dataset may also serve as a substrate for registering and merging intra-interventional 2D echocardiographic images into the EAM system without errors from the probe position sensing.

5.5 Conclusion

The major part of the LA anatomy incorporating the PVs, LAA, MV, AV and FO as important anatomical landmarks can be reconstructed successfully by registering and fusing 3D datasets acquired with the proposed 6-step TOE image acquisition protocol.

Acknowledgments

The support of Gerard van Burken in data processing is gratefully acknowledged.

Chapter 6

Fusion of Three-dimensional Transesophageal Echocardiographic Images of Left Atrium for Supporting Catheter Ablation Procedures: Comparison with Computed Tomography

This chapter has been published as:
B. Ren, H.W. Mulder, **A. Haak**, J. McGhie, T. Szili-Torok, K. Nieman, M. van Stralen, J.P.W. Pluim, M.L. Geleijnse, and J.G. Bosch, *Advanced Three-Dimensional Echocardiography*, chapter 4.2, pages 147-161, (2014).

Abstract

Objective: The aim of the study was to evaluate wide-view fused 3D transesophageal echocardiography (TEE) datasets of the left atrium (LA) for supporting catheter ablation procedures by comparing with computed tomography (CT).

Methods: Twenty-two patients undergoing transcatheter aortic valve implantation were included, who had had both CT and 3D TEE examinations. Six 3D TEE datasets were acquired according to the imaging protocol and were registered and fused manually in end diastole. Eight landmarks including mitral valve (MV), aortic valve (AV), left atrial appendage (LAA), fossa ovalis (FO), left superior pulmonary vein (LSPV), left inferior pulmonary vein (LIPV), right superior pulmonary vein, and right inferior pulmonary vein were marked in both fused 3D TEE and CT datasets. The Euclidean distances were calculated between corresponding landmarks.

Results: The wide-view registration and fusion of the 3D TEE datasets was feasible in all patients. The MV, AV, and LAA were visualized in all cases and FO in 77% of cases. LSPV including the common ostium was visualized in 64% and RSPV including the common ostium in 77% of the patients. The inferior PVs were visualized with 3D TEE in only one patient. The distances between the landmarks marked in the fused 3D TEE and CT datasets were 5 ± 3 mm.

Conclusion: Wide-view registration and fusion of the 3D TEE datasets were feasible and accurate in reconstructing the major part of the LA compared with the CT dataset. This technique can potentially replace the preinterventional CT or MRI in complex LA catheter ablation procedures.

6.1 Introduction

Atrial fibrillation (AF) is increasingly treated by catheter ablation, including pulmonary vein (PV) isolation and complex left atrial ablation for non-PV triggers, thus eliminating the triggers initiating AF[23]. Several imaging modalities are commonly applied before the intervention to visualize the left atrium (LA) along with the PVs, left atrial appendage (LAA) and mitral valve (MV), such as rotational angiography, computed tomography (CT), and magnetic resonance imaging (MRI)[105]. The pre-acquired CT or MRI images are segmented and registered within the electro-anatomical surface mapping (EAM) system to the real time mapping space during the procedure3. Since AF ablation procedures often need to be repeated and the substantial dose of ionizing radiation of CT scans, rotational angiography and fluoroscopy required by the procedures causes important delayed effects on patients [123, 76, 109], every attempt should be taken to minimize radiation exposure1. Additionally, CT and MRI are of cumbersome logistics and high cost.

Transesophageal echocardiography (TEE) is performed routinely to exclude LA/LAA thrombus before the catheter ablation. The anatomy of the LA and adjacent structures can be visualised in high resolution 2D and 3D TEE images [41, 63, 145]. However, the field of view of one single full volume 3D TEE dataset is not enough to visualize all important cardiac structures simultaneously, which is particularly true for the PVs at the left and right edges of the LA. We have shown in a previous study that it is feasible to reconstruct the majority of the LA with important anatomical landmarks with six single-view 3D TEE datasets acquired with a stepwise TEE image acquisition protocol [120]. In the present study, we sought to validate the wide-view fused 3D TEE dataset of the LA against CT by indicating the important anatomical landmarks in both fused 3D TEE and CT datasets. This is an important prerequisite in the process to replace pre-interventional CT by TEE in the catheter ablation procedures.

6.2 Patients and methods

Twenty-two patients (15 men, aged 79 ± 7 years old) who had undergone transcatheter aortic valve implantation (TAVI) for severe aortic valve stenosis were included in this study. These patients had undergone the CT examination three to five weeks before the procedure and 3D TEE examination during the procedure. The patients were under general anesthesia during the 3D TEE image acquisition. The protocol was approved by the institutional review board.

The TAVI patients were chosen as the study sample because they had had both CT and 3D TEE examinations. Although patients planned for catheter ablation all undertake the TEE exam a few days or immediately before the procedure, the TEE exam is always kept short and focused in our out-patient clinic in order to minimize patients' discomfort and 3D acquisition is not frequently performed. On contrary, the TAVI patients are under general anesthesia during the procedure, which provides

more time for 3D TEE acquisition and image optimization, thus are comparable ideal research subjects.

3D TEE image acquisition and registration

Intra-interventional TEE was performed with the iE33 xMatrix ultrasound system (Philips Medical System, Best, the Netherlands) with the CX7-2t matrix-array transducer. All acquisitions were performed at the mid-esophageal level. The image acquisition was performed following the stepwise image acquisition protocol depicted in our previous study [120] (Figure 1). In the protocol, Step 1 aimed to acquire the central view of the MV, LAA and aortic valve (AV); Step 2 was developed to acquire the left PVs and Step 3 to acquire the right PVs. Step 4, 5 and 6 were mainly used to create sufficient overlap between different datasets for image registration and fusion. The 2D reference views and 3D datasets were acquired according to the ASE guidelines for performing a comprehensive TEE examination [130] and the latest EAE/ASE recommendations for image acquisition and display using 3D echocardiography [77]. The 3D datasets were acquired with the full volume mode during one cardiac cycle with a proper depth and the largest volume size to include the structures of interest.

To construct a wide 3D view of the LA, the datasets of the six different steps were registered manually to the CT image in end diastole by a single observer (HWM). Firstly, a minimum of three landmarks was indicated in both the TEE and CT datasets. Depending on the TEE view, the coaptation point of the AV leaflets, coaptation point of the MV leaflets, fossa ovalis (FO) and LAA were used as soft landmarks. Occasionally, some additional corresponding points were indicated to improve the initial alignment between the images. Since corresponding time frames were registered, only rotational and translational differences between the volumes were expected and therefore a rigid transformation model was used. The landmarks were registered by a closed-form least squares optimization algorithm [65]. Secondly, image alignment was improved manually by rotating and translating the TEE volume with respect to the CT, viewing the result in all three orthogonal views. Thirdly, all different TEE images were jointly displayed with respect to the CT image and each other, to optimize the image alignment between the different TEE views, thus minimizing TEE misalignment. Once an adequate transformation was found, the datasets belonging to step 1, 2, 3, and 4, the views that were required for coverage of the heart, were fused with maximum intensity fusion. Data of step 5 and 6 were used only in the registration process and not included in the fusion.

Multislice CT image acquisition

Contrast-enhanced cardiac CT was performed using a dual-source CT system (Somatom Definition, Siemens Medical Solutions, Forchheim, Germany), with the following acquisition parameters: two tube-detector systems with a detector collimation of

32 x 0.6 mm, Z-axis flying focal spot for double sampling in the longitudinal axis, rotation time 330 ms (temporal resolution 85 ms), tube voltage 120 kV. The pitch varied between 0.2 for low heart rates (¡40 min-1) and 0.53 for high heart rates (¿100 min-1). Each tube provided 412 mA/rot (625 mA), and full X-ray tube current (100%) was given during the 14– 46% of the R – R interval. The scan ranged from the top of the aortic arch to the diaphragm. The radiation dose ranged from 8 to 20 mSv depending on body habitus and heart rate dependent table speed. The volume of iodinated contrast material (Iodixanol 320 mg/ml, GE Healthcare) was adapted to the expected scan duration. A contrast bolus (50–60 ml) was injected in an antecubital vein at a flow rate of 5.0 mL/s, followed by a second bolus of 30 – 40 at 3.0 ml/s. Bolus tracking was used to synchronize the start of the scan with opacification of the aortic root. Images were reconstructed at 5%-R-R intervals: slice thickness 1.5 mm; increment 0.4 mm; medium-to-smooth convolution kernel (B26f). In this study, we assessed CT datasets reconstructed during diastole, the same cardiac phase used in the TEE registration and fusion.

Indication of landmarks in the 3D TEE and CT datasets

Eight cardiac structures were chosen as the landmarks to be indicated in both fused 3D TEE and CT datasets: MV, AV, LAA, FO, left superior pulmonary vein (LSPV), left inferior pulmonary vein (LIPV), right superior pulmonary vein (RSPV), and right inferior pulmonary vein (RIPV). The common ostium of the PVs was defined if two PVs join each other and share a common stem before entering the LA or they enter the LA through the same ostium. All 3D TEE datasets were displayed as three orthogonal 2D views, which could be rotated and panned to locate the landmarks. The landmarks were indicated independently in the TEE and CT datasets at two different times in all 22 patients by one observer (BR) blinded to the image registration process. The landmarks were indicated in the following locations: 1) MV: in the center of the mitral annulus plane; 2) AV: in the center of the aortic annulus plane; 3) LAA: in the center of the ostium of the LAA; 4) FO: in the center of the thin fossa ovalis area; 5) LSPV: in the center of the ostium of the LSPV; 6) LIPV: in the center of the ostium of the LIPV; 7) RSPV: in the center of the ostium of the RSPV; 8) RIPV: in the center of the ostium of the RIPV. If two or more pulmonary veins entered the LA through a common ostium, only one landmark was marked in the center of the common ostium. If the cardiac structures were not visible in the datasets, the landmarks were skipped.

For correspondence evaluation, the differences between corresponding landmarks in the fused 3D TEE ($\mathbf{p}_{TEE} = (x_{TEE}, y_{TEE}, z_{TEE})^T$) and CT ($\mathbf{p}_{CT} = (x_{CT}, y_{CT}, z_{CT})^T$) datasets were calculated as Euclidean distances

$$d = \sqrt{(x_{TEE} - x_{CT})^2 + (y_{TEE} - y_{CT})^2 + (z_{TEE} - z_{CT})^2}. \tag{6.1}$$

Intra- and interobserver variability analysis

The landmarks were indicated a second time by the same observer (BR) and independently by a second observer (JMG) in five patients randomly chosen. The distances of 40 corresponding landmarks of CT-CT, TEE-TEE and CT-TEE by the same observer and between two observers were calculated.

6.3 Results

In Figure 2, a fused 3D TEE dataset of one patient are shown along with the CT dataset in different orientations to show important cardiac structures. In Figure 3, one fused 3D TEE dataset with the landmarks indicated for TEE and CT is shown.

Using CT as the gold standard, the visibility of eight landmarks in fused 3D TEE datasets in all patients is depicted in Table 1. As shown in Table 1, a left PV common ostium was observed in 14 cases using CT and seen in the fused 3D TEE datasets in 10 cases (71%). A right PV common ostium was seen in 2 patients using CT and also in the fused 3D TEE dataset (100%).

For the eight cardiac structures chosen as the landmarks, the distances between the corresponding landmarks placed in the fused 3D TEE and CT datasets are shown in Figure 4. The distances of the landmarks of the LIPV and RIPV were not calculated because they were seen in the fused 3D TEE dataset only in one patient. The distance between landmarks was 5 $\pm$ 2 mm for MV, 4 $\pm$ 2 mm for AV, 5 $\pm$ 2 mm for LAA, 6 $\pm$ 3 mm for FO, 9 $\pm$ 4 mm for LSPV, and 5 $\pm$ 3 mm for RSPV.

The intra- and interobserver variabilities in landmarks are shown in Table 2. The intraobserver and interobserver variabilities of TEE-TEE and CT-CT distances were small, but were also shown to constitute a considerable part of the CT-TEE distances.

6.4 Discussion

In this study, we compared the wide-view fused 3D TEE datasets of the LA with the CT data. The main findings were 1) the wide-view registration and fusion of the 3D TEE datasets was feasible in all patients and enabled the visualization of major parts of the LA; 2) important anatomical landmarks such as the MV, AV, LAA and FO could be clearly visualized in the fused 3D TEE in all (MV, AV and LAA) or almost all patients (FO); 3) LSPV including the common ostium could be visualized in 64% and RSPV including the common ostium in 77% of the patients. However, the LIPV and RIPV were very difficult to visualize with 3D TEE; 4) the registration and fusion of the 3D TEE datasets tended to be accurate as the average distances between the landmarks marked in the fused 3D TEE dataset and those made in the CT dataset were 5 $\pm$ 3 mm for the important cardiac structures.

Table 1 The visibility of eight anatomic landmarks in the fused 3D TEE dataset compared with CT in 22 patients.

	CT	Fused 3D TEE	Visibility
MV	22	22	100%
AV	22	22	100%
LAA	22	22	100%
FO	22	17	77%
LPV common ostium	14	10	71%
LSPV	8	4	50%
LIPV	8	1	13%
RPV common ostium	2	2	100%
RSPV	20	15	75%
RIPV	20	0	0

Visibility was calculated as the number of fused 3D TEE divided by the number of CT. CT, computed tomography; TEE, transesophageal echocardiography; other abbreviations as in Figure 1, 2 and 3.

Table 2 Distances between 40 landmarks marked in CT and fused 3D TEE datasets, and distances between landmarks in CT and 3D TEE datasets in five patients from the same observer (intraobserver) and two observers (interobserver).

	Intraobserver	Interobserver
CT – CT (mm)	3 ± 2	5 ± 3
TEE – TEE (mm)	3 ± 2	7 ± 4
CT – TEE (mm)	6 ± 4	10 ± 5

Data presented as bias ± standard deviation. Abbreviations as in Table 1.

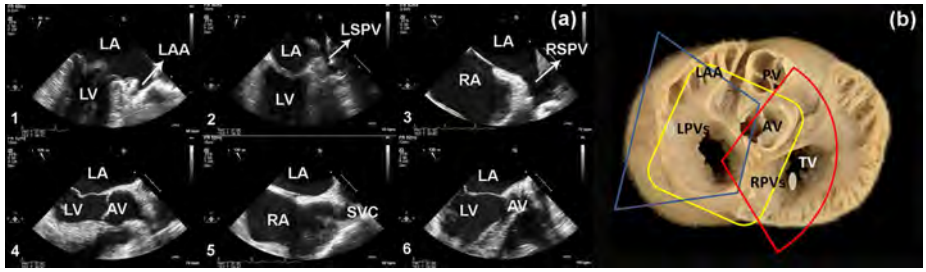

Figure 6.1: A: 2D transoesophageal echocardiography reference views of the 6-step image acquisition protocol. 1, the mitral commissural view; 2, the superior commissural view including the left upper pulmonary vein; 3, the modified bicaval view including the right upper pulmonary vein; 4, the aortic valve long axis view; 5, the midpoint view between the aortic valve long axis and bicaval views; 6, Further left to the aortic valve long axis view. B: cardiac structures acquired in the 3D datasets of Step 1 (yellow), Step 2 (blue) and Step 3 (red). The grey areas represent the area of the pulmonary vein ostia projected to the cross-section of the anatomical view. AV, aortic valve; LA, left atrium; LAA, left atrial appendage; LPVs, left pulmonary veins; LSPV, left superior pulmonary vein; LV, left ventricle; MV, mitral valve; PV, pulmonary valve; RA, right atrium; RPVs, right pulmonary veins; RSPV, right superior pulmonary vein; SVC, superior vena cava; TV, tricuspid valve. The figure is cited from Ren B et al. J Interv Card Electrophysiol. 2013 Jun;37(1):21-6. Permission was obtained.

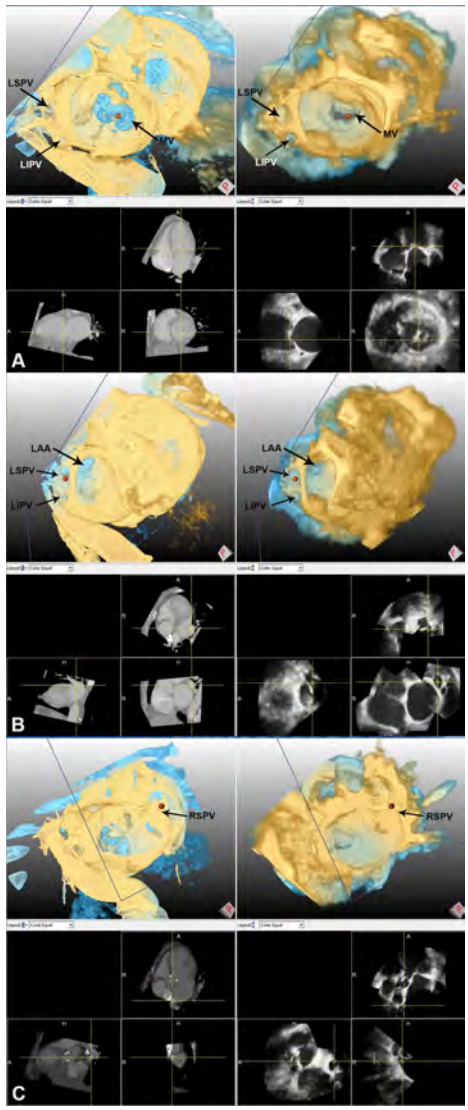

Figure 6.2: An example of a fused 3D transesophageal echocardiographic dataset and the corresponding CT dataset with important cardiac structures indicated. The 2D multiplanar reconstruction planes of both 3D echocardiographic and CT data are also shown. A: mitral valve en-face view with left pulmonary veins; B: left atrial appendage and left pulmonary veins; C: right inferior pulmonary vein. Some part of the fused 3D echocardiographic and CT datasets was cropped to reveal the anatomic landmarks. CT, computed tomography; LIPV, left inferior pulmonary vein; RSPV, right superior pulmonary vein; other abbreviations as in Figure 1.

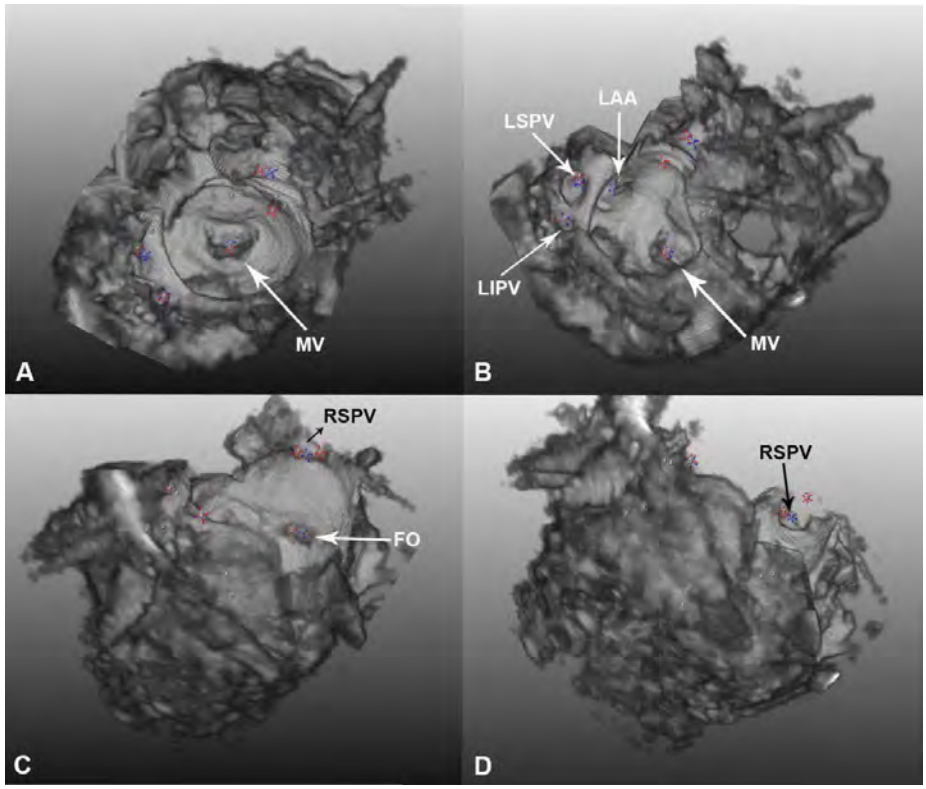

Figure 6.3: An example of a fused 3D transesophageal echocardiographic dataset with landmarks on the important cardiac structures. Red crosses are the landmarks marked in the CT dataset and blue crosses are the landmarks marked in the fused 3D TEE datasets. The right superior pulmonary vein ostium was not visible in the 3D TEE dataset. FO, fossa ovalis; other abbreviations as in Figure 1 and 2.

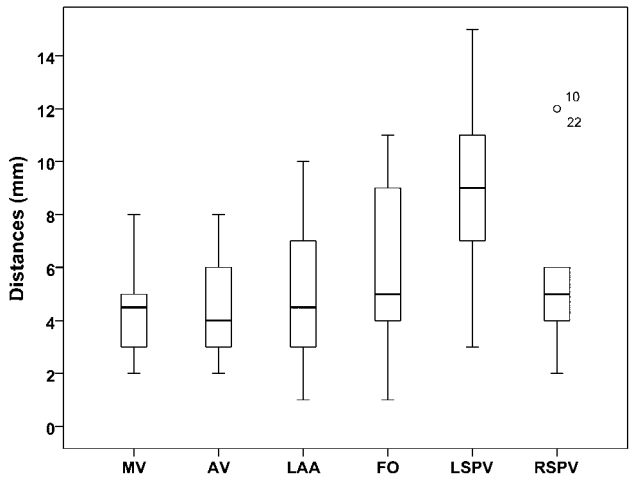

Figure 6.4: Boxplots showing the distance between corresponding landmarks. Open dot as outlier. Abbreviations as in Figure 1, 2 and 3.

The single view 3D TEE datasets were acquired with a systematic step-wise TEE image acquisition protocol as described in our previous study [120]. This image acquisition protocol provides a systematic and fast procedure for acquiring 3D TEE datasets which allow the manual registration and fusion. Important anatomical structures for the ablation procedure could be clearly visualized in the fused 3D TEE datasets. Centrally located structures such as MV, AV, LAA and FO were well visualized in the fused 3D TEE datasets in all (MV, AV, LAA) or the majority of the patients (FO in 77%). The reason why the FO was not visible in all patients was because it was not included in the 3D acquisition sector in some patients since the image protocol was set to focus on PVs. In fact, the atrial septum including the FO can be excellently visualized with 3D TEE [77, 41], as this technique is commonly used to diagnose atrial septum defect [140, 90]. Since the PVs are adjacent to the lung and the 3D datasets are likely to suffer from the echo drop-out, the ostia of the PVs were less distinguishable than other cardiac structures. This might be the main reason for the invisibility of the inferior PVs because the inferior veins tend to be smaller and have shorter distances from the ostia to the first-order branches than the superior veins and the LIPV is surrounded by descending aorta and lung. In addition, the superior veins enter the LA in an anterosuperior direction, whereas the inferior veins open into the LA perpendicular to the posterior wall [86]. The posterior wall of LA was always lost in the

3D TEE datasets, because the currently used matrix TEE probe (Philips CX7-2t) is not capable of visualising the structures in the very near field of the ultrasound beam. Variances in the PV anatomy are commonly seen, such as a short or long common venous trunk or supernumerary veins [71]. These increase the difficulty in distinguishing the PVs in the fused 3D TEE datasets. Additionally, the variable distance of the transducer placed into the esophagus and the PVs may also affect imaging. When the oesophagus and transducer inside is close to the left PVs, imaging of right PVs can be easier, while imaging of the lower left PV is troublesome, and vice versa. There is quite a variance in the chance of visualizing the inferior PVs in the literature [4, 42] and it should be noted that the visualisation of PVs using TEE also depends on the operator's experience and apparently requires certain training.

As shown in the results, the distances between landmarks in the fused 3D TEE and CT datasets were around 5 mm, which is quite small for such cardiac structures compared with the reported inaccuracies in the EAM [60]. The reported distances are a combination of several inaccuracies: the TEE fusion and reconstruction inaccuracies, the observer variability in the landmarks, different physiological conditions between the CT and TEE images taken weeks apart and inherent differences between the CT and TEE images. Since the intraobserver and interobserver CT-CT and TEE-TEE distances were 3 to 7 mm (Table 2) , the CT-TEE distances could be largely attributed to observer variability, and the errors due to registration and modality differences were actually much smaller than suggested by the measurements. In order to investigate the cause of the distances between landmarks in 3D TEE and CT datasets, especially for the distances larger than 10 mm, we further calculated the distance vector in two directions: radial and circumferential (with respect to the centre of the LA). The results, however, showed no significant correlation between the absolute distance and the radial distance. On inspection, in all four cases where the landmark indicated in the fused 3D TEE datasets was not reliable, this was proven to be because of inferior 3D image quality, not because of registration errors.

Limitations

Although the major part of the LA was reconstructed accurately by registering the 3D TEE datasets, it was still not possible to reconstruct the whole LA as the posterior wall of the LA was always lost in the 3D datasets as discussed above. There may be several solutions for this, e.g. using a balloon standoff or using a probe of higher frequency. These solutions are subject of further study. In the imaging protocol, the inferior PVs are not visualized in the 2D reference views. Because of the close location between the superior and inferior PVs, we assume that with sufficient image quality, both veins could be included in the 90°x 90°3D acquisition sector even if only one vein is seen in the 2D reference view. Different 2D views specially targeting at the inferior PVs could be used [77, 42], yet the inferior PVs cannot always be visualized in certain views as the success rate reported largely varied [4, 42], especially in diseased hearts

whose orientations maybe changed due to chamber enlargement.

The study was carried out in patients undergoing the TAVI procedure, in whom both CT and TEE studies were available. Although the AV and MV annuli were often heavily calcified in this patient population, the 3D TEE image quality in terms of structure recognition was not influenced by the strong echo of calcified annuli. Nevertheless, this study ultimately aims at facilitating the catheter ablation procedures in patients with AF. Thus, the ideal patient population would be patients undergoing the catheter ablation. However, the accuracy of fusing 3D TEE datasets acquired in the patients with AF compared with CT is assumed to be similar as shown in this study. Besides, patients with AF usually have enlarged LA as patients with aortic stenosis, but whether the degree of LA enlargement is comparable between the two patient populations still needs interrogation.

In this study, all 3D TEE datasets were registered manually, which requires specific expertise and relatively long time. An automatic registration method is highly desirable. This will eliminate manual input and speed up the registration process, which can be further incorporated into the ultrasound system, thus allowing an online reconstruction. In fact, this current study constitutes a proof of principle for the future case where such an automated registration will be available, and shows that TEE may support the ablation procedure as the fused 3D TEE dataset can be made available during the procedure. The parts that are not well visualized (atrial posterior wall and inferior PVs) should then be further elucidated during the simplified EAM procedure.

The temporal mismatch between the different TEE subsets may play an important role in the registration errors. The volume rates of the 3D TEE datasets were very low (4 Hz) because they were acquired from one cardiac cycle, which limits temporal alignment and results in different positions of fast moving cardiac structures. The volume rate can be improved if full volume 3D datasets are acquired from more cardiac cycles. However, it should be noted that the patients included in this study were under general anaesthesia and had a stable heart rate. In non-anaesthetised patients, the heart rate may vary more especially in patients with AF who usually have irregular R-R interval, thus stitching artefacts might adversely affect the registration.

The use of CT as the basis and aid for the manual TEE registration may provide a bias in the CT-TEE comparison, especially since some landmarks (MV, AV, FO) are used in both processes. However, the landmarks indicated in the TEE registration were not known to the observers performing the landmark indication. In fact, the TEE registration could also be performed without the CT and alignment of the TEE sets was finally performed between TEE datasets.

Clinical implications

The wide-view fused 3D TEE dataset can represent the atrial anatomy in a similar way as the preoperative CT does. Apart from some of the inferior PVs and the atrial

posterior wall, the major structures are represented correctly. Regarding the poor visibility of the inferior PVs in the fused 3D TEE datasets, implementing 3D TEE in the PV isolation procedure may be limited. However, this technique might replace pre-interventional CT or MRI in facilitating ablation approaches not targeting the PVs, including ablation of peri-mitral flutter, LA tachycardia (post-ablational superior PVs and LAA tachycardias), septal atrial tachycardia, and LAA occlusion which is performed frequently during the catheter ablation procedure. In a separate study, we have shown that a multicavity anatomy can be successfully segmented from these TEE images [53]. This segmented 3D surface could be imported to the EAM system, which may obviate the need for preoperative CT. Additionally, intra-interventional 2D echocardiographic images can be matched to the pre-interventional 3D TEE images, preventing cumbersome multi-modality registration to CT or MRI images. TEE probes equipped with 3D position sensing or X-ray based position/orientation estimation [137] will fit this application even better. The wide-view fused 3D TEE dataset may also serve as a substrate for registering and merging intra-interventional 2D echocardiographic images into the EAM system without errors from the probe position sensing.

6.5 Conclusion

Wide-view registration and fusion of the 3D TEE datasets were feasible and accurate in reconstructing the major part of the LA compared with the CT dataset. This technique may replace the pre-interventional CT or MRI in complex LA catheter ablation procedures. When the visualization of the ostia of inferior PVs is improved, this technique could be applied in catheter ablations targeting at PVs as well.

Acknowledgments

The support of Gerard van Burken in data processing is gratefully acknowledged. We acknowledge MeVis Medical Solutions AG (Bremen, Germany) for the use of MeVisLab for analysis and visualization in this study. This research was supported by the Dutch Technology Foundation STW, which is the applied science division of NWO and the Technology Programme of the Ministry of Economic Affairs.

Chapter 7

Improved segmentation of multiple cavities of the heart in wide-view 3D transesophageal echocardiograms

This chapter has been published as:
A. Haak, B. Ren, H.W. Mulder, G. Vegas-Sánchez-Ferrero, G. van Burken, A.F.W. van der Steen, M. van Stralen, J.P.W. Pluim, T. van Walsum and J. G. Bosch, Improved segmentation of multiple cavities of the heart in wide-view 3D transesophageal echocardiograms, *Ultrasound in Medicine and Biology* in press (2015)

Abstract
Minimally-invasive interventions of the heart such as in electrophysiology (EP) are becoming more and more important in clinical practice. Currently, preoperative Computed Tomography Angiography (CTA) is used to provide anatomical information during EP intervention, but this does not provide real-time feedback and burdens the patient with additional radiation and side effects of the contrast agent. Three-dimensional transesophageal echocardiography (3D TEE) is an excellent modality to visualize anatomical structures and instruments in real-time but some cavities suffer from the limited coverage of the 3D TEE volumes which is especially true for the left atrium (LA). This leads to difficulties segmenting the LA. We propose to replace or complement preoperative CTA imaging by wide-view TEE. We tested this on twenty patients for which TEE image volumes covering the LA and CTA images were acquired. The TEE images were manually registered and wide-view volumes were generated. Five heart cavities in single-view TEE and the wide-view TEE were segmented and compared to atlas based segmentations derived from the CTA images. We could show that the segmentation accuracy (Dice coefficients) improved relative to segmentation of single-view images by 5, 15, and 9 % points for left atrium, right atrium, and aorta respectively. Average anatomical coverage was improved by 2, 29, 62, and 49 % points for right ventricle, left atrium, right atrium, and aorta respectively. This finding confirms that wide-view 3D TEE can be useful for support of electrophysiology interventions.

7.1 Introduction

With the aging population in the western world, and improved survival of congenital diseases and infarcts, treatment of cardiac arrhythmias becomes more and more important. Cardiac electrophysiology (EP) is therefore a rapidly growing specialization in cardiac care. Atrial fibrillation (AF) is an unsynchronized or reduced contraction of the atria due to abnormal electrical activation patterns in the atria, and it is very common in elderly people. When pharmacological treatment is no longer effective, AF can be treated by interruption of the electrical pathways that induce the arrhythmia. Open heart surgery [31] is one way of isolating erroneous conduction sites but the involved risks are often too high for patients in this population [115].

In EP, AF is generally treated in a minimally invasive way by mapping the ECG signals inside the atrium and ablating the culprit sites with RF ablation catheters. The ablation may sometimes be limited to a few points, but in many procedures continuous lines of ablation points need to be created to isolate a region on the atrial wall, leading to very lengthy and costly procedures. In the last decade, anatomical features became more important for treating AF; for instance, by creating circumferential lines around the pulmonary veins (PVs) [108, 107]. The large anatomical variability in the PVs [48] and the high risk of complications [118] made 3D visualization of anatomical structures necessary.

Currently, the major means of real-time visualization during the intervention is X-ray fluoroscopy, which produces a 2D projection image only, has poor or no soft tissue contrast, and uses ionizing radiation [76]. The ablation and ECG catheters are equipped with 3D position sensors and their position is continuously tracked. By moving these catheters over the atrial wall, a rough 3D electro-anatomical map (EAM) of the atrium can be constructed [133]. This map is not very precise because of the limited number of contact points involved, influence of breathing and cardiac motion and the inaccuracy of 3D sensing. This led to the integration of preoperative computed tomography angiography (CTA) images into the EAM [37] to supply a better impression of the patient's specific LA anatomy. These preoperative images are segmented and the resulting surfaces are imported into the EAM system. By indicating a number of anatomical landmarks in EAM and segmentation, the segmentation can be registered to the EAM. However, the preoperative CTA is a relatively costly, logistically cumbersome procedure, and burdens the patient with ionizing radiation. Moreover, these preoperative images are often acquired weeks before the intervention, and the current physiological state of the LA can be quite different from the preoperative images. Therefore, it is sometimes still difficult to ensure continuous ablation lines especially when dealing with abnormal anatomies. We believe that these shortcomings in the visualization of the anatomical structure are an important cause of the low success rate of the EP procedures: 52 % without and 76 % with the use of antiarrhythmic drugs [24]. In order to achieve these success rates in 27 % of the patients multiple procedures were necessary.

Three-dimensional (3D) transesophageal echocardiography (TEE) with its good tissue-to-blood contrast could be an ideal real-time and preoperative modality to guide EP interventions. Preoperative TEE is generally performed shortly before the EP intervention, to exclude the presence of thrombus in atria and left atrial appendage. To complement or replace preoperative CTA, segmentation of the cardiac cavities in 3D TEE is required to allow the endocardial surfaces to be shown within the EAM system. We showed previously [53] that segmenting heart cavities in single TEE volumes is possible but may be limited by the narrow field of view (FoV). Wide-view image fusion is one way to increase the FoV [96] and we showed that by combining four TEE volumes we could cover most of the left atrium (LA), identify the main LA structures with accuracy similar to CTA and thus possibly replace preoperative CTA [120].

The purpose of this study is to investigate to what extent well-registered wide-view fused TEE images can be segmented appropriately and to confirm our hypothesis that the segmentation accuracy of wide-view TEE improves with respect to single views. Please note, that the purpose of this study is not to evaluate a fusion/registration method nor to investigate the clinical benefit of fusion; the fusion itself is only instrumental here. We are solely investigating the potential beneficial effect of an idealized fusion on the segmentation performance. We tested our hypothesis on a set of twenty patients for whom CTA and TEE were available.

7.2 Materials and Methods

A schematic outline of the used data and involved processing steps is shown in Fig. 1. For each patient six TEE views are manually registered and fused to create a wide-view image. A blood/tissue classifier and segmentation is applied to the wide-view images and the segmentation results are validated with CTA segmentations. We compare the segmentation results of the wide-view images with the results of a single-view image.

TEE Image Acquisition

Six 3D TEE image volumes were acquired per patient at mid-esophageal level following the protocol that we described earlier [120]. All TEE images were acquired with an iE33 system in combination with a matrixTEE probe (X7-2t, Philips Healthcare, The Netherlands). One to three heart cycles were acquired in "Live 3D" mode with a volume rate of 4.3 ± 0.9 volumes/sec. The image sector was set to 90 by 90 degrees and the imaging depth was 10 ± 2 cm.

There are three main volumes: 1) covering the central view including the mitral valve, the left atrial appendage, and the aortic valve; 2) aiming to the left including left PVs; 3) covering the atrial septum and the right PVs. The other three volumes are intermediate steps to ensure sufficient overlap of volumes 1 to 3. More details on the acquisition protocol can be found in [120] and an example of the different views

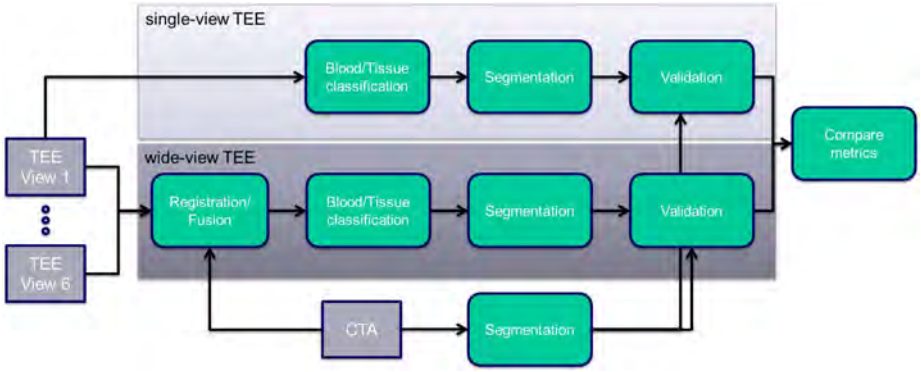

Figure 7.1: Block diagram of our methods and validation. For each patient six TEE images and one CTA image was acquired. We used a manual registration to align the six TEE views and subsequently a wide-view TEE image was created. A blood/tissue classifier was run on the single- and wide-view images followed by a segmentation. The segmentations were validated with a ground truth derived from the CTA image.

can be seen in Fig. 2.

TEE Image Registration and Fusion

To build a 3D wide-view of the heart, the data sets of the six different volumes were registered manually to the corresponding CTA image and to each other. Since we aim at a proof-of-principle for the segmentation of fused sets we wanted to test our segmentation on the best possible registration and fusion. Even though we expect that artifacts caused by registration errors and fusion in the wide-view images will only minimally affect our segmentation scheme, we did not want to mix the errors of the registration and segmentation and chose to evaluate our wide-view segmentation with the best possible registration. Therefore, we chose to use an elaborate manual registration in order to minimize the effect of registration errors on the segmentation results.

First, a single observer picked in each of the six TEE images and the CTA image the end diastolic volume and indicated a minimum of three anatomical landmarks (from a set of 8) in all volumes. From corresponding landmarks an initial rigid transform (rotation and translation only) was computed. Second, image alignment was improved by manually refining the rotation and translation of the TEE volume with respect to the CTA image. The correct alignment of the anatomical structures was checked by

slicing the volumes in three orthogonal cross-sections and overlaying the resulting 2D images. Third, after repeating step one to two for all 6 TEE views, all TEE images were jointly displayed with respect to the CTA image and each other. With small manipulations of the rotations and translations of the individual TEE volumes the alignment of the overall anatomical structures was optimized. The registered TEE volumes are shown in Fig. 2. Once the adequate transformations were found, the volumes 1 to 4 were fused since these views contain all the information and view 5 and 6 only add overlap between view 1, 3, and 4. Therefore, we excluded view 5 and 6 from the fusion to minimize fusion artifacts. Furthermore, minimum-intensity fusion was chosen to suppress artifacts especially at the edge of the imaging cones.

The registration accuracy, the coverage and morphology of anatomical landmarks, and the correspondence of landmarks in fused TEE volumes and CTA volumes was assessed previously [119]. In this study a total of 8 landmarks (mitral valve, aortic valve, left atrial appendage, fossa ovalis, and left/right superior/inferior pulmonary veins) were indicated in wide-view TEE and CTA images by two experts. Please note, that coverage of LA in the wide-view TEE was not complete and specifically the inferior pulmonary veins were mostly not covered. Good spatial agreement was shown between landmarks derived from wide-view TEE and CTA images with an average Euclidean distance of 5±3 mm. The good correspondence between CTA and fused TEE can be visually appreciated in Fig 3.

Gamma Mixture Model

Classifying different tissues such as myocardium and blood can be done based on the differences in intensity distribution of the so-called ultrasound *speckle* for these tissues. Previously, Vegas-Sánchez-Ferrero et al. [152, 150, 149] showed that a Gamma Mixture Model (GMM) can accurately represent the intensity distribution ($\mathbf{X} = \{X_i\}, i = 1...N$, with N denoting the number of voxels) of ultrasound images after beam-forming, post-processing, and interpolation. An Expectation Maximization algorithm [95] was used to estimate the parameters ($\mathbf{\Theta} = \pi_1, ..., \pi_J, \alpha_1, ..., \alpha_J, \beta_1, ..., \beta_J$) of a two-class ($j = \{1, ..., J\}, J = 2$) mixture model with the probability density function

$$p\left(x|\mathbf{\Theta}\right) = \sum_{j=1}^{2} \pi_j f_X\left(x|\alpha_j, \beta_j\right), \tag{7.1}$$

where f_X denotes the Gamma density function. A 3D map showing the voxel-wise probability of blood versus tissue is then computed by applying Bayes' theorem. An example slice of a TEE volume and the computed tissue probability map is shown in Fig. 4.

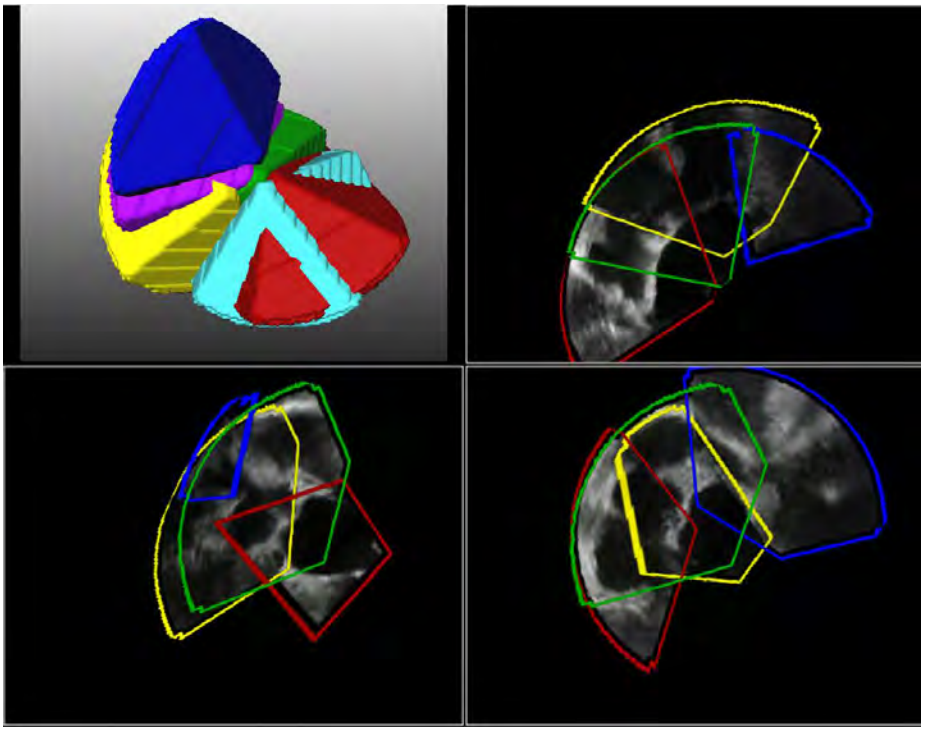

Figure 7.2: Display of the registered six TEE volumes. The center view (view 1) is shown in yellow, the view the furthest to the left (view 2) is shown in blue, and the view to the furthest to the right (view 3) is shown in red. The intermediate views four (green), five (turquoise), and six (purple) are recorded to ensure sufficient overlap between the center and the most right view. For image fusion views 1, 2, 3, and 4 were used.

Active shape model

Active shape models (ASM) [29, 59] employ statistical shape models (SSM) generated from a large training set to model all probable anatomical variations in organ shape. The SSMs used in this work were derived from 151 3D CTA segmentations [73, 91] containing the left and right atria (LA and RA), left and right ventricles (LV and RV), and the aorta (Ao). We created SSMs for the complete heart keeping 90 % and for the individual cavities keeping 98 % of the shape variation. The CTA scans were

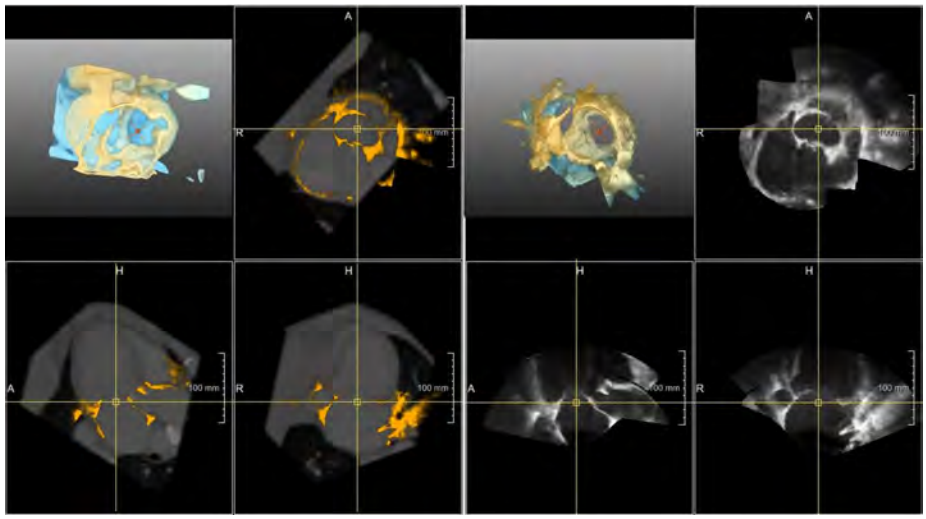

Figure 7.3: Rendered CTA volume (top left) and rendered fused TEE (top right). The three orthogonal cross sections of the CTA (left) and the fused TEE (right) are shown as well. The marker in the 2D views (yellow cross) indicates the center of the mitral valve. The same location is shown in the 3D rendering indicated by the red cross. Please note the good anatomical correspondence between CTA and TEE. This can be appreciated in the 2D CTA cross sections (left) where the fused TEE is overlaid in orange.

made from a mixed population of patients covering a large variability in anatomy and pathology [91]. Although this patient population does not explicitly relate to TAVI-specific pathology, the excellent generalization capabilities of SSMs are expected to overcome this [59]. In our TEE segmentation scheme, update points ($\mathbf{r}'$) are found along the surface normals of each shape vertex ($\mathbf{r}$) in the tissue probability maps by minimizing an objective function as described by Van Ginneken *et al.* [143]. The pose and/or shape of the ASM is updated until convergence. The pose (scale, rotation and translation) is estimated by a weighted least square scheme which was described in [5, 65]. Shape updates are estimated by a weighted projection to the shape parameter space as described by Cootes *et al.* [28]. The weights w used for the pose and shape updates are composed from a GMM based edge probability, $w_{GMM}(\mathbf{r}')$, a model distance term, $w_{ASM}(\mathbf{r}')$, and a term to disqualify points outside the pyramidal TEE volume, $w_{US}(\mathbf{r}')$. The weighting factor is computed as follows:

$$w(\mathbf{r}') = w_{ASM}(\mathbf{r}')\ w_{US}(\mathbf{r}')\ w_{GMM}(\mathbf{r}'), \tag{7.2}$$

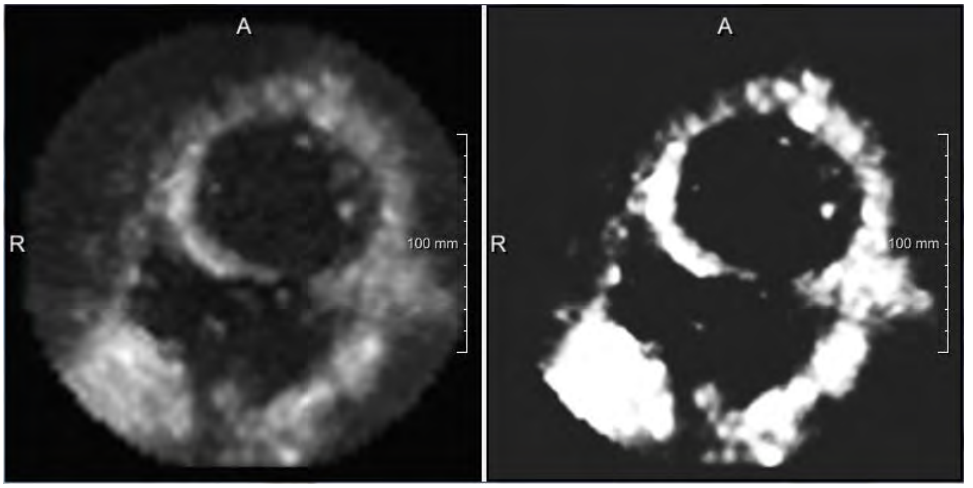

Figure 7.4: Short axis cross section through a TEE volume (left) and the corresponding tissue probability map (right). Note the suppression of speckle in the tissue probability map compared to the intensity map.

where

$$w_{ASM}\left(\mathbf{r}'\right) = \exp\left(-\frac{\|\mathbf{r}-\mathbf{r}'\|^2}{\sigma^2}\right), \tag{7.3}$$

σ is used to adjust the model distance penalty term, and $\|\cdot\|$ indicates the Euclidean distance. The term $w_{US}\left(\mathbf{r}'\right)$, is derived by convolving the binary TEE mask with a Gaussian kernel with a standard deviation of $\sqrt{20}$ voxels. The GMM term, $w_{GMM}\left(\mathbf{r}'\right)$, enhances update points being close to the blood/tissue transition zone (probability of 0.5) and is defined as

$$w_{GMM}\left(\mathbf{r}'\right) = 1 - \frac{\left|p_2\left(I\left(\mathbf{r}'\right)|\mathbf{\Theta}\right) - 0.5\right|}{0.5}, \tag{7.4}$$

where $I\left(\mathbf{r}'\right)$ is the intensity in the TEE image at $\mathbf{r}'$.

Segmentation scheme

We use a three-stage segmentation scheme where the mean shape of the SSM is initialized by a rigid transform computed from three manually indicated landmark points. Generally, each stage is initialized with the results of the previous stage while the model pose is more and more constrained and the shape is more and more relaxed. The different stages and their function are described by the flow chart in Fig. 5.

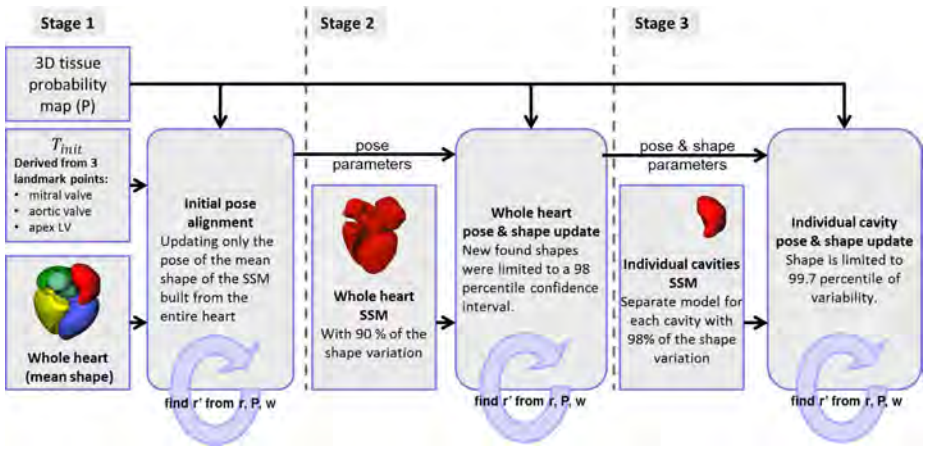

Figure 7.5: Three stage segmentation scheme: At each stage the model is updated until convergence. Convergence criterion is a RMS difference between the current and previous shape of less than 0.1 mm. **First stage**, the mean shape of the SSM containing all five cavities is initialized using a rigid transform derived from three landmark point pairs. In this stage only the pose is updated and the resulting transform is passed to the next stage. **Second stage**, pose and shape of the complete heart SSM are simultaneously updated. **Third stage**, For each heart cavity a separate SSM is used and initialized based on the pose and shape of the previous stage. The shape estimates for stage 2 and 3 are limited to a hyper-ellipsoid defined by the 98th percentile of the shape parameters' χ^2 distribution [29]. Please note that in this segmentation scheme the pose is more and more constrained while the shape is more and more relaxed while propagating through the stages. The constraining and limiting parameters used for all stages are shown in Table 1.

Table 7.1: Segmentation parameters: σ defines the range of w_{ASM}, c constrains $\boldsymbol{\theta}, \mathbf{t}, \mathbf{b}$, and c_a constrains a at each iteration. Upper and lower limits for the pose and shape parameters have the subscript lim.

parameters	stage 1 (S1)	stage 2 (S2)	stage 3 (S3)
c	0.0	0.2	0.6
c_a	0.0	0.2	0.3
σ (voxel)	44	20	20
a_{lim} (%)	$\pm$30 of a_{init}	$\pm$18 of a_{S1}	$\pm$15 of a_{S2}
$\boldsymbol{\theta}_{lim}$ (°)	$\pm$30 of $\boldsymbol{\theta}_{init}$	$\pm$20 of $\boldsymbol{\theta}_{S1}$	$\pm$5 of $\boldsymbol{\theta}_{S2}$
$\mathbf{t}_{lim}$ (mm)	$\pm$30 of $\mathbf{t}_{init}$	$\pm$20 of $\mathbf{t}_{S1}$	$\pm$5 of $\mathbf{t}_{S2}$
$\mathbf{b}_{lim}$(%)	0.0	98.0	99.7

To guarantee a high robustness of the segmentation scheme the pose parameters and the shape are constrained and limited to a plausible range.

In the different stages we constrain the pose parameters (scale, rotation, and translation) and shape parameters to prevent large jumps of the model due to erroneous edge responses. Each of the parameters p at iteration i is constrained by

$$p_i = c p_{i-1} + (1 - c)\, \hat{p}_i, \tag{7.5}$$

where $\hat{p}_i$ indicates the estimated unconstrained parameter at iteration i. The used constraints are shown in table 1. These constraints are identical to those used in single TEE segmentations [53] for fair comparison.

The scale (a_{lim}), the rotation angles ($\boldsymbol{\theta}_{lim}$), the translation ($\mathbf{t}_{lim}$) and the shape ($\mathbf{b}_{lim}$) are limited and their values for the different stages are shown in table 1 as well.

7.3 Experiments

Data

The segmentation method was validated in 3D TEE data sets obtained from 20 patients (13 male, 7 female; mean age $\pm$ standard deviation: 80$\pm$7) undergoing a Transcatheter Aortic Valve Implantation (TAVI). The data acquisition protocols were approved by the institutional review board (MEC-2013-257), and informed consent was obtained from all patients. All patients had severe aortic valve stenosis with different severity of valve regurgitation. This caused for all patients severe pathologies with different degrees of LV hypertrophy and enlargement as well as LA enlargement. All TAVI patients had 3D TEE data acquired during the preparation of the intervention. The patients were anesthetized and in supine position. The end-diastolic (ED) time-frame was manually selected. All patients also underwent a gated CTA three to five weeks

before the intervention for preoperative planning. More details on the CTA acquisition protocol can be found in [120].

Gold standard

Segmentations of CTA images from the same twenty patients served as the ground truth. We generated these using a multi-atlas based approach introduced in [73]. The CTA volumes were cropped so that only the heart was in the image volume. The ASM was generated earlier on 151 patients and did not include any of the CTA segmentations which were used for our validation. All CTA segmentations were visually inspected and considered of good quality. The CTA segmentations provide an independent ground truth of the cavity outline and are not limited to the TEE FoV. One should note that the CTA supplies the anatomy of the same patient but at a different time and with a different modality, so one can not expect a perfect match with TEE.

Evaluation measures

For comparing the different segmentations, overlap in volume for each cavity was expressed as a Dice coefficient in 3D [35]. The distance between corresponding 3D segmentations was computed as average Euclidean point-to-surface distance ($P2S_{mean}$). Please note that the Dice coefficient and the $P2S_{mean}$ were computed for the whole heart and not limited to the FoV. Furthermore, the percentage of each cavity that is contained within the FoV is measured, both for the single-view segmentations and the wide-view. It is expected that the segmentation accuracy of each cavity is related to this coverage.

7.4 Results

Spatial Coverage

The coverage of the FoV for each heart cavity for the single-view and wide-view images was computed based on the CTA segmentations and is shown in Fig. 6. It is shown that the wide-view images contain a much larger portion of the different cavities. The median coverage increased by 2, 29, 62, and 49 percent points for RV, LA, RA, and Ao respectively. The FoV of the LV did not improve since it was captured already within the single-view volumes (view 1).

Segmentation

A qualitative example of a wide-view TEE volume with corresponding CTA and their segmentations are shown in Fig. 7. In Fig. 8 the box-plots of the Dice coefficients and in Fig. 9 the $P2S_{mean}$ distances for all cavities are shown. On the left of Fig. 8

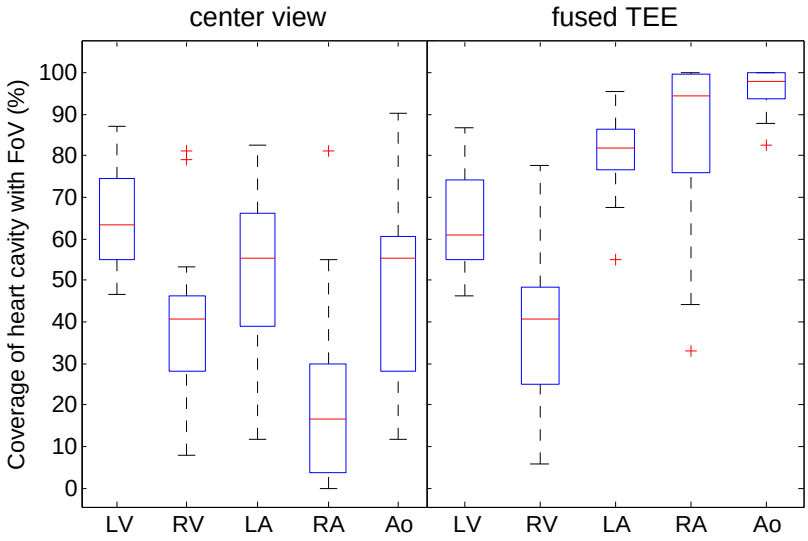

Figure 7.6: Coverage of the different heart cavities within the field of view (FoV) of the single-view TEE image (left) and of the fused wide-view TEE image (right). The red horizontal line indicates the median, the blue box indicates the 25 and 75 percentiles, and the whiskers indicate the range excluding outliers. Outliers are considered data points beyond mean ± 2.7 times the standard deviation and plotted as red +. Note the improved coverage of the LA, RA, and Ao cavities compared to the single-view images.

and 9 the segmentation results using only the central TEE volume (view 1) are shown, whereas on the right the segmentation results using the fused TEE volumes are shown. It is shown that the cavities which had an improved coverage with the wide-view TEE FoV also had an improved segmentation accuracy.

7.5 Discussion

We showed previously that wide-view TEE images can provide an alternative to preoperative CT images in clinical applications [119]. In this work we investigated to what extent wide-view TEE volumes can be used to to improve segmentation accuracy. To that end, we segmented twenty single and wide-view patient data sets successfully

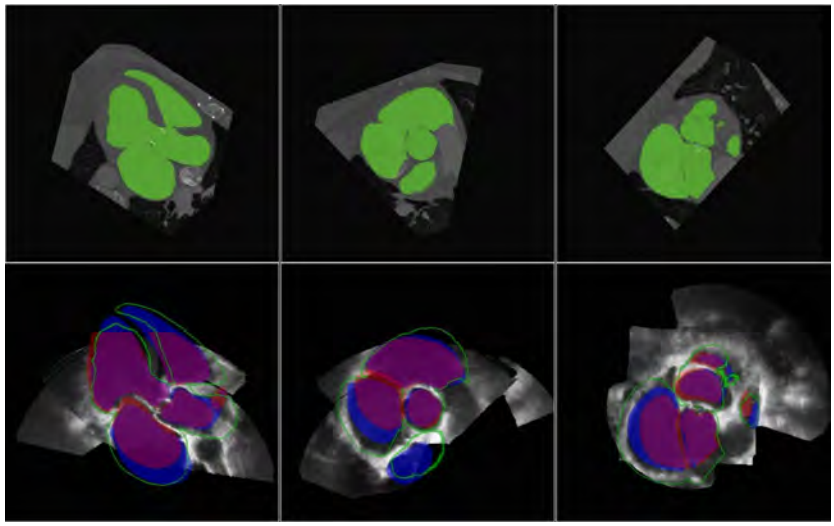

Figure 7.7: Three orthogonal cross sections of the CTA volume with the segmentation overlaid (top). The same cross sections are displayed for the fused TEE data set (bottom) together with the segmentation results based on the single-view (red) and the fused wide-view data (blue). The outline of the CTA based segmentation is shown in green.

with our segmentation scheme and compared them with CTA derived segmentations which served as ground truth.

Generally, the wide-view TEE images helped to improve the coverage of the FoV for the different heart cavities and fusion artifacts did not hamper the segmentation accuracy.

We obtained improvements of the segmentation results of LA, RA, and Ao which improved the median Dice coefficient by 5, 15, and 9 percent points respectively (see Fig. 8). This may be mostly due to the improved field of view which resulted in a coverage of 82, 94, and 97 percent compared to the single-view coverage of 56, 17, and 56 for LA, RA, and Ao, respectively. The RA improves the most from the wide-view TEE which is most likely due to larger distance of the TEE probe relative to the RA. Furthermore, we expect that other applications that depend on image segmentation such as volume and wall motion estimation would benefit from an extended coverage. For LV and RV, which had no improved FoV compared to the single-view TEE segmentations, the segmentation accuracy stayed the same. This implies that generally the segmentation accuracy is not deteriorated by the fusion.

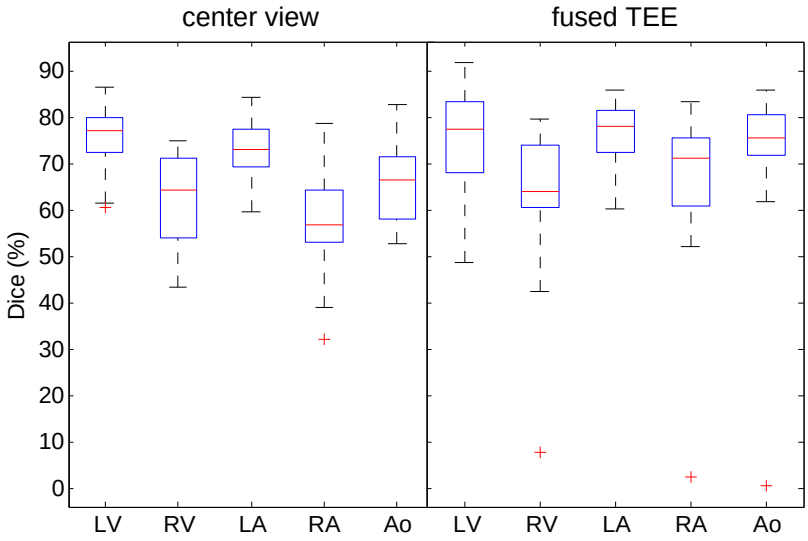

Figure 7.8: Comparison (Dice) of single-view segmentation (left) and fused TEE segmentation (right) vs. CTA segmentations. The computation of the Dice coefficients was not restricted to the FoV of the TEE images.

For one fused patient data set segmentation failed (see Fig. 8, outliers). Visual inspection of the fused image data and the segmentation indicated that for this patient the image data of the different views was quite noisy, had low SNR and the individual views seemed to have quite different mean intensities. This resulted in a wide-view image with considerable artifacts which misguided the segmentation.

Four registered TEE volumes were fused to a wide-view image utilizing a minimum-intensity fusion which creates in our opinion the least fusion artifacts. However, this method still creates some fusion artifacts, such as propagating echo drop outs and edges of the single-view sectors, which will create false edges and may influence the segmentation scheme (see Fig. 3). There could also be some temporal mismatches between the different single-view volumes which also will influence the cavity borders in the fused image. With a higher volume rate these errors should be reduced. To further reduce fusion artifacts we did not include views 5 and 6 since they are intermediate views. They do help in the spatial alignment process by providing additional overlap between views 1, 3, and 4. However, the fusion artifacts mainly come from the edges of the imaging cone where the image quality is compromised. If that area is already

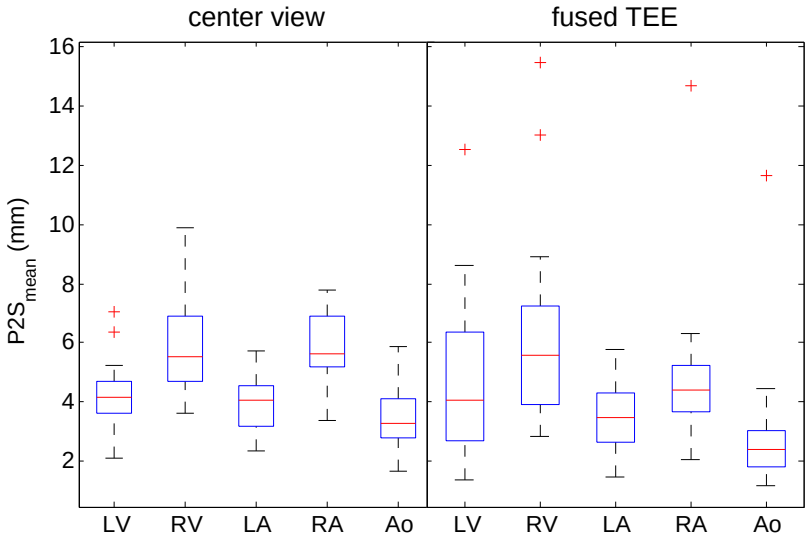

Figure 7.9: Comparison (Point-to-surface distance) of single-view segmentation and fused TEE segmentation vs. CTA segmentations. The computation of the mean point-to-surface distances was not restricted to the FoV of the TEE images.

covered well by other views the edge artifacts may locally deteriorate the total fused image.

We did not obtain a significant improvement of the segmentation results for LV and RV (see Fig. 8 and 9). This may be due to the fact that the center view (view 1) contained most of the LV and RV and the wide-view fusion did not add much information. This is supported by the finding that the FoV did not improve for LV and RV, respectively (see Fig. 6). Although it has been reported by others that multi-view fusion may improve the image quality in transthoracic echocardiography [116] this is not very apparent in TEE. The effect of multi-angle compounding is small in TEE, since the position of the probe in the esophagus is almost the same for all views. Also, the minimum-intensity fusion that we applied is not improving local image quality, although it is good for reducing artifacts.

Limitations

Up to now our segmentation work is based on manual registration of the single TEE volumes. This is arguably a major limitation for the practical usability of such a method in the clinic. However, this is a proof-of-principle study and we use the manual registration as a best-case proxy for a general automated registration to show that segmentation results improve in wide-view TEE. We refrained from testing the observer variability of the manual registration in conjunction with our segmentation method since this will not be part of a final automated method. As soon as an automatic registration method is available, an assessment of the influence of its registration accuracy on the segmentation outcome should still be performed. Our next step is to apply the segmentation in combination with an automated registration approach for TEE images. Our group previously reported good results for different registration metrics for transthoracic US/US registration [96] which is promising for replacement of CTA/MR. However, we chose to use an elaborate manual registration scheme since this is currently the most accurate method and will minimally deteriorate the results of our segmentation.

Our final goal is to replace or complement CTA/MR. For complementing CTA/MR with wide-view TEE, automatic intermodality registration would be desired. However, to our knowledge there is not yet a reliable standard method of registering ultrasound images to CT or MR and this is an ongoing research topic.

The segmentation scheme is currently initialized by three manually indicated landmark points. Note that an automatic method for initialization has been recently proposed by Curiale et al. and tested on the same data set as used in this study [32]. This automatic initialization showed similar segmentation results as our manual initialization despite the fact that the generated landmark points were quite different (median Euclidean distance about 6 to 12 mm). This shows that the method is robust against variations in the landmarks and that complete automatization seems feasible.

Another limitations is that the ground truth segmentations are derived from a different imaging modality (CTA) which uses different physical principles for image contrast formation. Furthermore, there are weeks between CTA and TEE image acquisitions which may have resulted in changes in anatomy and physiological state. Therefore, we cannot expect perfect correspondence between wide-view TEE and CTA. In a previous study [119] we investigated the correspondence between fiducial landmarks in CTA and wide-view TEE. We found an average Euclidean distance of about 5 ± 3 mm between fused TEE and CTA landmarks. This distance may seem high at first glance but one should realize that the intra-observer variability of repeated indications of the landmarks in the CTA volumes was already about 4 mm. Therefore, we conclude that correspondence between CTA and fused TEE is actually quite good and that some of the landmarks were difficult to consistently indicate, due to their tubular structure. The $P2S_{mean}$ in our study includes a similar intermodality difference error which means that the difference between TEE segmentations and anatomical reality

may be considerably smaller than the values reported in Fig. 9.

Future work

We expect that a more sophisticated fusion method than minimum-intensity fusion may improve the segmentation results further. The outer edges of ultrasound image volumes are usually hampered by artifacts and low SNR due to side lobes. Taking this information into account, a weighted-mean fusion with lower weights at the sides of the imaging pyramid than in the center portion may improve the image quality of the fused volumes. However, the fusion artifacts did not affect the segmentation scheme in all but one extreme case. Also, the quality of our segmentation should still be investigated in combination with an automated registration approach, when this becomes available.

We are confident that our technique can improve the intra-operative visualization in EP procedures and may reduce the need of pre-operative imaging such as CT/MR and the use of X-ray fluoroscopy.

7.6 Conclusions

We showed that wide-view fusion can improve segmentation accuracy for TEE images by 5, 15, and 9 percent points for LA, RA, and Ao respectively. This proves that in principle 3D TEE is capable of visualizing large parts of the heart and that segmentation accuracy can be improved compared to single-view TEE, which makes this wide-view segmentation a good candidate for support of EP interventions.

Acknowledgements

This research is supported by the Dutch Technology Foundation STW (10847), which is the applied science division of NWO, and the Technology Programme of the Ministry of Economic Affairs.

Dr. Vegas-Sanchez-Ferrero wants to acknowledge to Consejeria de Educacion, Juventud y Deporte of Comunidad de Madrid and the People Programme (Marie Curie Actions) of the European Union's Seventh Framework Programme (FP7/2007-2013) under REA grant agreement n. 291820.

Chapter 8

Catheter shape estimation using tracked ultrasound imaging and Kalman filters

This chapter has been published as:
A. Haak, G. Vegas-Sánchez-Ferrero, and J. G. Bosch, Catheter Catheter shape estimation using tracked ultrasound imaging and Kalman filters, *International Journal of Computer Assisted Radiology and Surgery* (submitted).

Abstract
For minimally invasive interventions accurate estimation of the tool position, orientation, and shape relative to the anatomical context is critical for a successful outcome. Electrophysiology interventions suffer from a lower success rate compared to open heart surgeries, which may be due to the inadequate real-time visualization of ablation catheters. Ultrasound imaging is an excellent modality to visualize catheters and anatomy and has been successfully used to guide minimally invasive interventions. However, in electrophysiology ultrasound imaging is not used for tracking catheters yet. In this paper we develop and validate a tracking scheme, modeling the ablation catheter and estimating the catheter location and shape in a Kalman filter framework. We tested our tracking scheme on simulated catheters and experimental data by scanning an ablation catheter in a water tank. We could show that our estimation scheme works well and outperforms estimates derived from noisy measurements.

8.1 Introduction

Minimally invasive interventions are becoming more and more important and sophisticated in clinical practice nowadays. Depending on the medical field and type of intervention, the used tools range from simple needles to sophisticated devices such as complex catheters with a multitude of degrees of freedom, artificial valves with complex internal structures used in transcatheter aortic valve implantation (TAVI), and devices for left atrial appendage (LAA) closures [15].

For the clinician it is essential to accurately know the position of the device relative to the target site. For instance, needle biopsies used to be performed to a large extent blindly, only guided by palpation. Ultrasound (US) guided biopsies enabled to visualize the target site and the needle in real-time, improving the clinical outcome. It has been reported that ultrasound guided liver biopsies compared to blind liver biopsies have 10 percent points less minor complications and 2 percent points less major complications [159]. This demonstrates that for the success of minimally invasive procedures the correct estimation of the device position, orientation and shape within the anatomical target site is crucial.

One of the oldest and most common guided minimal invasive procedures are needle biopsies with US imaging, which is used for many types of interventions such as breast, liver and prostates biopsies, to name just a few. Two-dimensional (2D) and three-dimensional (3D) ultrasound is used to visualize the needle and target sites [19, 72]. Needle deflection[99] and tissue deformation [36] have been modeled and there are now robots and steerable needles that can be used to avoid vulnerable areas such as blood vessels and nerves and to improve biopsy sampling [72, 2].

There are many other devices used in clinical practice. Simple wires under X-ray guidance were first used to visualize and to open coronary stenoses and occlusions in the heart. Later on more sophisticated balloon and stenting catheters were developed which added higher demands on the image guidance to correctly deploy these catheters and stents. Electrophysiology (EP) interventions became feasible when more sophisticated technology could be integrated into the catheters, such as ECG electrodes, RF-ablation, position sensing, force sensing, and irrigation. In EP, heart rhythm disorders are treated among others with catheter ablations. EP catheters are equipped with electrodes to measure the ECG and to ablate tissue at specific sites within the heart to create isolating lesions. Therefore many of those catheters are steerable or specially shaped (lasso catheter) [117] to reach different sites in the heart. Currently, the major imaging modality in EP is X-ray but lately also intra cardiac echo (ICE) and transesophageal echo (TEE) are used more and more during interventions. Furthermore, the catheter tip location is usually measured with a 3D position sensing system enabling to show the current catheter position, the recorded ECG signals on the heart wall, and the ablation position in an augmented reality environment, so-called electro-anatomical maps (EAM) [133, 37]. However, EP ablation, for instance around the pulmonary vein, are still not as successful as open heart surgical methods

[31, 115, 24]. These advanced catheters pose high demands on the image guidance and inadequate imaging/tracking of the catheter might be one of the major factors that EP ablations fall back compared to surgical procedures.

We believe that modeling the mechanical behavior of the catheters similar to needle deflection models could be beneficial for catheter tracking and shape estimation. The catheter could be scanned in consecutive cross-sections with tracked US imaging similar as shown in Fig. 8.1. Since the catheter is continuous and bends are usually moderate the knowledge of the catheter image plane cross-section in one image can be used to predict the intersection position of the catheter in the next image. Scanning and estimating the position of the cross-section over a larger area could be used to build up a catheter shape model. If such a catheter model is once built this could be used to help predicting the image catheter intersection during the next scan.

Furthermore, there are many imaging modalities and tracking systems in the EP lab which could potentially improve catheter tracking if they are combined appropriately. For instance, the EP electromagnetic tracking systems can provide the location of the catheter tip quite accurately and in real-time. However, there is no information provided away from the tip of the catheter. We believe that if the shape of the catheter can be estimated and if the mechanical properties (e.g. mechanical stiffness and bending) are modeled correctly the motion of the tip could be "propagated" to estimate the motion at parts away from the catheter tip. Modeling the mechanical properties of a device and predicting the deformation of the device could be used to estimate e.g. the proper fit and the firm seat of a LAA closure device or TAVI valve.

Kalman filters (KF) [69] are an excellent tool for estimating model states from noisy measurements in real-time. There have been many applications of Kalman filters ranging from aerospace control and navigation up to medical image segmentation [104]. KFs recursively predict the state from a state model and update the state with noisy measurements. Extended Kalman filters (EKF) [89, 134] and unscented Kalman filters (UKF) [68] were derived from the original KF formulation and are capable of handling non-linear models. Therefore, we believe that if the device and the sensor fusion is properly modeled, accurate device position, orientation and shape estimates are possible using KFs.

In this paper we would like to test applicability for device position and shape estimations by a relatively simple device model. A catheter is scanned with a tracked ultrasound probe resulting in a series of short axis cross sections of the catheter. Image acquisition and image plane velocity are chosen such that the distance between consecutive image slices is small which allows us to use a relatively simple catheter model. An UKF [68] is used since the obtained model is non-linear. An UKF performs as good as an EKF without the necessity to estimate Jacobian matrices [156]. We tested our model on straight and bent catheters with data derived from simulations and experimental scans in a water tank. In this paper we would like to show that modeling the mechanical behavior of the catheter in conjunction with a tuned UKF is capable of improving catheter location estimates with respect to the raw measurements.

8.2 Methods

8.2.1 Modelling

In this section we develop the image plane and catheter state model. We focus on tracked free hand US which is used to scan a catheter in short axis cross sections. We assume that the image plane movement is slow and that the US image frame rate is high enough so that we can assume that the catheter pieces between consecutive US images can be approximated by straight line elements. In the following sections we develop the kinematic model for the image plane movement and the catheter-image plane intersection.

Image Plane

We assume without loss of generality that the image plane is moving almost with constant velocity and orientation, scanning a volume which contains the catheter (see Fig. 8.1). The plane position (offset) relative to a reference coordinate system is given by the column vector $\mathbf{O} = [x_O, y_O, z_O]^T$, where ^{T} indicates the transpose. The plane orientation is described by two unit vectors $\widehat{\mathbf{u}}$ and $\widehat{\mathbf{v}}$ and its normal unit vector $\widehat{\mathbf{n}}$. A sketch of the plane and its parameters are shown in Fig 8.2.

The current orientation of the image plane can be expressed using the three Euler angles (α, β, γ) which are used to compute the rotation matrix as $\mathbf{R}(\alpha, \beta, \gamma) = \mathbf{R}_z(\gamma)\,\mathbf{R}_y(\beta)\,\mathbf{R}_x(\alpha)$. The plane orientation is then computed by

$$[\widehat{\mathbf{u}}, \widehat{\mathbf{v}}, \widehat{\mathbf{n}}] = \mathbf{R}(\alpha, \beta, \gamma)\,\mathbf{Id}_3 \tag{8.1}$$

where Id_3 is the 3×3 identity matrix which accounts for the canonical base representation. We are assuming that the image plane is moved in a sweeping motion (forward and backward) over the catheter with a slowly varying velocity. We therefore model the image plane position and orientation over time (or discretized time step k) as a 1st-order approximation. This can be written as

$$\mathbf{s}_k^\pi = \mathbf{F}_k \mathbf{s}_{k-1}^\pi + \mathcal{N}\left(\mathbf{0}, \boldsymbol{\sigma}_p^\pi\right), \tag{8.2}$$

with

$$\mathbf{s}^\pi = \left[\mathbf{O}^T, \dot{\mathbf{O}}^T, \alpha, \beta, \gamma, \dot{\alpha}, \dot{\beta}, \dot{\gamma}\right]^T \tag{8.3}$$

where $\mathbf{s}_k^\pi$ is the current plane state vector, $\mathbf{s}_{k-1}^\pi$ is the previous state vector, $\mathbf{F}_k$ is the state transition matrix, and $\mathcal{N}\left(\mathbf{0}, \boldsymbol{\sigma}_p^\pi\right)$ is an additive zero mean Gaussian noise term with a standard deviation denoted by $\boldsymbol{\sigma}_p^\pi$. The dot above the letters indicates the first time derivative.

Image Plane Catheter Intersection

We assume that the catheter piece between consecutive image planes (e.g. $\mathbf{O}_k$ and $\mathbf{O}_{k-1}$) can be approximated by a line segment (see Fig. 8.1 and 8.2) if the sampling period (Δt) of the image planes is short, the velocity of the plane movement is low, the catheter is continuous, and the bending radius is not extreme. Any point lying on this line segment, $\mathbf{p}(\lambda)$, can be interpolated by the parametric equation

$$\mathbf{p}(\lambda) = \mathbf{p}_{k-1} + \lambda \mathbf{v}_k, \tag{8.4}$$

with

$$\mathbf{v}_k = \mathbf{p}_k - \mathbf{p}_{k-1}, \qquad \text{and} \qquad \lambda \in [0, 1], \tag{8.5}$$

where $\mathbf{p}_k$ and $\mathbf{p}_{k-1}$ are the 3D intersection points of the plane with the catheter at the current and previous time point. The direction vector $\mathbf{v}_k$ in conjunction with the parameter λ varies the position of the point on the line segment.

Any point lying on the image plane can be described by the parametric equation

$$\mathbf{p}(u, v) = u \cdot \widehat{\mathbf{u}}_k + v \cdot \widehat{\mathbf{v}}_k + \mathbf{O}_k \tag{8.6}$$

by varying the parameters u and v. See Fig. 8.2 for details.

The intersection point between the image plane and the line segment can be computed by setting equation 8.4 and 8.6 equal

$$\mathbf{p}_{k-1} + \lambda \mathbf{v}_k = u \cdot \widehat{\mathbf{u}}_k + v \cdot \widehat{\mathbf{v}}_k + \mathbf{O}_k \tag{8.7}$$

and solving for λ, u, and v. When the distance between consecutive image planes is small, we can assume that the line segment direction does not change by much so that $\mathbf{v}_k \approx \mathbf{v}_{k-1}$. This system of equations can be solved for the three parameters. For readability we will just refer to this function as

$$[\lambda, u, v] = f_{inter}\left(\mathbf{p}_{k-1}, \mathbf{v}_{k-1}, \widehat{\mathbf{u}}_k, \widehat{\mathbf{v}}_k, \mathbf{O}_k\right). \tag{8.8}$$

The actual expressions for solving the parameters λ, u, and v are given in Appendix 8.6.

Catheter intersection point

After computing the intersection parameters (λ, u, v) with equation 8.8 the k-th intersection point, $\mathbf{p}_k$, could be computed with equation 8.4 or 8.6. Since we can measure the plane intersect parameter u, v in the image directly we decided to use equation 8.6 which translates then to

$$\mathbf{p}_k = u \cdot \widehat{\mathbf{u}}_k + v \cdot \widehat{\mathbf{v}}_k + \mathbf{O}_k \tag{8.9}$$

With this we can formulate the state vector of the catheter piece

$$\mathbf{s}^{cat} = \left[\mathbf{v}, \mathbf{p}\right]^T. \tag{8.10}$$

Overall State Vector and State Transition function

The overall state vector is just a concatenation of the catheter state vector $\mathbf{s}^{cat}$ and the image plane state vector $\mathbf{s}^{\pi}$

$$\mathbf{s} = \begin{bmatrix} \mathbf{s}^{cat} \\ \mathbf{s}^{\pi} \end{bmatrix}. \tag{8.11}$$

The forward propagation of the catheter state is non linear since the computation of the parameters u and v is not a linear combination of the other state vector components. Therefore, we use a state transition function $f_{\mathbf{s}}(\mathbf{s})$ to predict the next state

$$\mathbf{s}_k = f_{\mathbf{s}}(\mathbf{s}_{k-1}) + \mathcal{N}(\mathbf{0}, \boldsymbol{\sigma}_p), \tag{8.12}$$

where $k-1$ indicates the previous state, and $\mathcal{N}(\mathbf{0}, \boldsymbol{\sigma}_p)$ is the overall zero mean Gaussian process noise term. Details of how the state transition function $f_{\mathbf{s}}(\mathbf{s})$ is computed are given in algorithm 1.

Algorithm 1 Forward function.

function $f_{\mathbf{s}}(\mathbf{s}_{k-1})$
  $\mathbf{s}^{cat}_{k-1}, \mathbf{s}^{\pi}_{k-1} \leftarrow \mathbf{s}_{k-1}$ ▷ Get the catheter and plane state vectors.
  $\mathbf{s}'^{\pi}_k = \mathbf{F}_k \mathbf{s}^{\pi}_{k-1}$ ▷ Predict the state of the plane. Primes indicate predictions.
  $[\mathbf{p}_{k-1}, \mathbf{v}_{k-1}] \leftarrow \mathbf{s}^{cat}_{k-1}$
  $[\widehat{\mathbf{u}}'_k, \widehat{\mathbf{v}}'_k, \mathbf{O}'_k] \leftarrow \mathbf{s}'^{\pi}_k$
  $[\lambda, u, v] = f_{inter}(\mathbf{p}_{k-1}, \mathbf{v}_{k-1}, \widehat{\mathbf{u}}'_k, \widehat{\mathbf{v}}'_k, \mathbf{O}'_k)$ ▷ Compute intersection parameters.
  $\mathbf{p}'_k = u \cdot \widehat{\mathbf{u}}'_k + v \cdot \widehat{\mathbf{v}}'_k + \mathbf{O}'_k$ ▷ Predict intersection point.
  $\mathbf{v}'_k = \mathbf{p}'_k - \mathbf{p}_{k-1}$ ▷ Predict direction of line element.
  $\mathbf{s}'^{cat}_k \leftarrow [\mathbf{p}'_k, \mathbf{v}'_k]$
  $\mathbf{s}'_k \leftarrow [\mathbf{s}'^{cat}_k, \mathbf{s}'^{\pi}_k]$
  return $\mathbf{s}'_k$

8.2.2 Unscented Kalman Filter

The Kalman filter [69] is a powerful tool to estimate system states of linear systems from noisy measurements. The original KF implementation can be used to predict the states of a linear model. The extended KF [134, 89] was developed to deal with non-linear systems by linearizing (first-order approximation) the non-linear system around the current state. However, this first order approximation can introduce large errors [156] and the unscented Kalman filter [68] (UKF) was introduced. The UKF uses a deterministic sampling approach where a minimal set of sample points is propagated

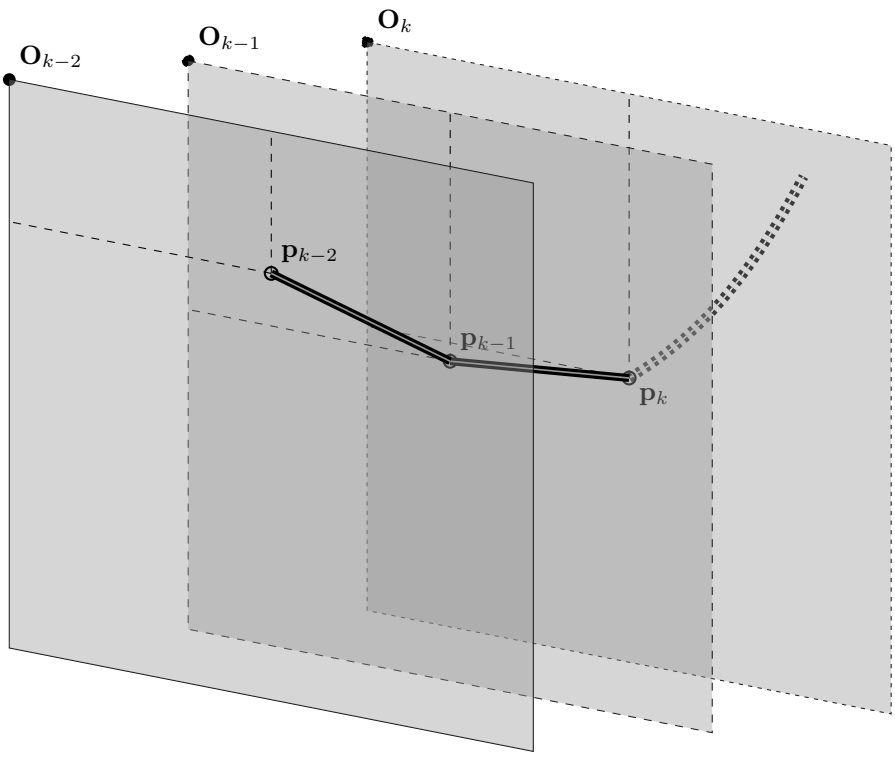

Figure 8.1: Plane positions depicted at several time points (k). We are assuming that the tracked ultrasound image plane is moved over the catheter obtaining short axis slices of the catheter. If the image plane orientation and position are known the intersection points ($\mathbf{p}$) of the catheter with the image plane can be estimated as well as measured by tracking the catheter intersection in the ultrasound image itself.

through the non-linear system, capturing the mean and variance of the state up to the

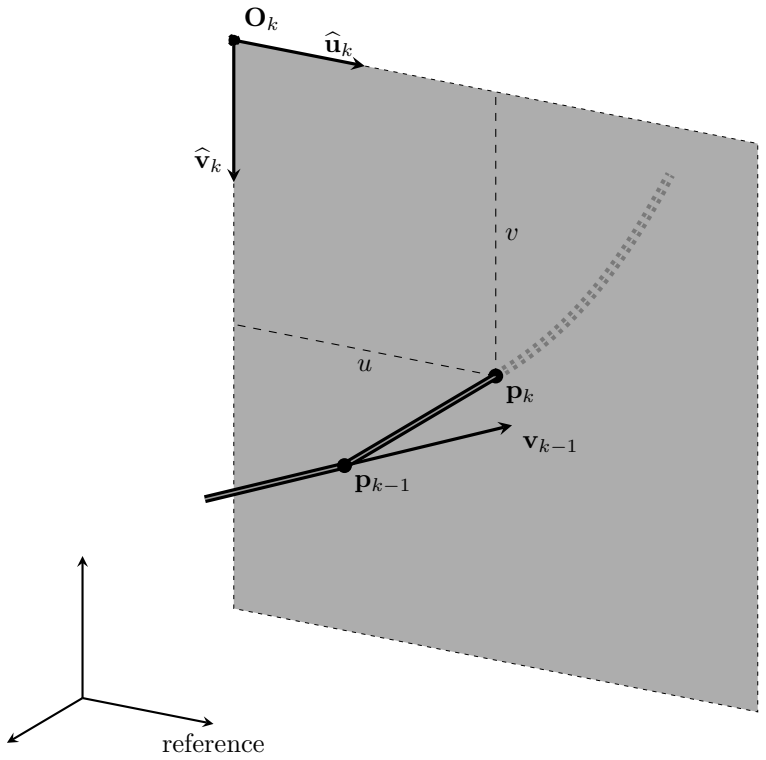

Figure 8.2: Sketch of the image plane catheter intersection. The current image plane position relative to a reference is given by $\mathbf{O}_k$ and the plane orientation is described by the vectors $\widehat{\mathbf{u}}_k$ and $\widehat{\mathbf{v}}_k$. The current image plane catheter intersection is given by $\mathbf{p}_k$. Note that the intersection point can be predicted with a relative small error by using the directional information of the previous line element $\mathbf{v}_{k-1}$ if the curvature of the catheter is not extreme and distance between consecutive image planes is small. The intersection of the catheter in the image can be detected and is described by u and v.

third order approximation [156]. There is extensive literature about the workings of

the Kalman filter and the UKF [68, 156] and we therefore refrain from explaining the UKF details here. However, in order to repeat our experiments someone would need to know the state vector $\mathbf{s}$, the state transition function $f_{\mathbf{s}}$, the process noise covariance $\mathbf{Q}$, the measurement vector $\mathbf{z}$, the measurement function $h_{\mathbf{s}}$, and the measurement noise covariance $\mathbf{R}$. The state vector and the state transition function were explained in the previous section. The other variables are introduced in the following sections.

Measurement Vector and function

The image plane location ($\mathbf{O}$) and orientation (α, β, γ) can be measured with an electro-magnetic or optical tracking system attached to the US probe. The coordinates of the catheter intersection within the image plane (u, v) can be detected using image processing tools (see section 8.2.4 for more details). The measurement vector, $\mathbf{z}$ can then be written as

$$\mathbf{z} = \left[u, v, \mathbf{O}^T, \alpha, \beta, \gamma\right]^T. \tag{8.13}$$

The current state vector $\mathbf{s}_k$ is transformed into the measurement space by a measurement function $h_{\mathbf{s}}$

$$\mathbf{z}_k = h_{\mathbf{s}}\left(\mathbf{s}_k\right) + \mathcal{N}\left(\mathbf{0}, \boldsymbol{\sigma}_m\right), \tag{8.14}$$

where $\mathbf{z}_k$ is the measurement vector and $\mathcal{N}\left(\mathbf{0}, \boldsymbol{\sigma}_m\right)$ is the measurement noise, where $\boldsymbol{\sigma}_m$ is the standard deviation of the measurements. The measurement function is non-linear and details of how $\mathbf{z}_k$ is computed are given in algorithm 2.

Algorithm 2 Measurement function.

function $h_{\mathbf{s}}(\mathbf{s}_k)$
  $[\mathbf{p}_k, \mathbf{v}_k, \mathbf{O}_k, \alpha_k, \beta_k, \gamma_k] \leftarrow \mathbf{s}_k$
  $\widehat{\mathbf{u}}_k = \mathbf{R}\left(\alpha_k, \beta_k, \gamma_k\right)[1, 0, 0]^T$ ▷ Compute 1st plane vector using equ. 8.1.
  $\widehat{\mathbf{v}}_k = \mathbf{R}\left(\alpha_k, \beta_k, \gamma_k\right)[0, 1, 0]^T$ ▷ Compute 2nd plane vector using equ. 8.1.
  $[\lambda, u, v] = f_{inter}\left(\mathbf{p}_k, \mathbf{v}_k, \widehat{\mathbf{u}}_k, \widehat{\mathbf{v}}_k, \mathbf{O}_k\right)$ ▷ Compute intersection parameters.
  $\mathbf{z}_k \leftarrow [u, v, \mathbf{p}_k, \mathbf{v}_k, \mathbf{O}_k, \alpha_k, \beta_k, \gamma_k]$
  return $\mathbf{z}_k$

Process and Measurement Noise Covariance Matrices

The process noise covariance matrix $\mathbf{Q}$ is computed in two parts. The process noise for the image plane $\mathbf{Q}^{\pi}$ (linear part of the model) is computed by

$$\mathbf{Q}^{\pi}(\Delta t) = \int_0^{\Delta t} \mathbf{F}\mathbf{Q}\mathbf{F}^T dt, \tag{8.15}$$

where $\mathbf{Q}$ is the covariance matrix of the continuous stochastic processes [18]. Note that we are assuming a first order model where the uncertainty comes from the velocity elements of $\mathbf{s}^{\pi}$. Thus, the covariance of the transformed variables $\mathbf{F}\mathbf{s}^{\pi}$ at a differential time dt becomes $\mathbf{Q}^{\pi}(dt) = \mathbf{F}\mathbf{Q}_{\mathbf{c}}\mathbf{F}^{T}$ where updated variables $(\mathbf{O}_k, \alpha_k, \beta_k, \gamma_k)$ are approximated as $(\mathbf{O}_k, \alpha_k, \beta_k, \gamma_k) + (\dot{\mathbf{O}}_k, \dot{\alpha}_k, \dot{\beta}_k, \dot{\gamma}_k)dt$. The stochastic process is assumed to be a wide sense stationary (WSS) Gaussian process where all the uncertain variables (velocities) are independent and identically distributed with zero mean and spectral density $\Phi_{\mathbf{s}}$. Under these assumptions, the variance in each sample time Δt can be easily calculated by the integral form shown in eq. (8.15) and is shown in Appendix 8.6.

The non-linear part of the noise model (catheter) can be described as:

$$\mathbf{Q}^{cat} = \mathbf{I}\sigma_p^2, \tag{8.16}$$

where $\mathbf{I}$ is the identity matrix, and σ_p^2 is the process noise variance. The overall process noise is then composed as a block matrix

$$\mathbf{Q} = \begin{bmatrix} \mathbf{Q}^{cat} & \mathbf{0} \\ \mathbf{0} & \mathbf{Q}^{\pi} \end{bmatrix}, \tag{8.17}$$

where $\mathbf{0}$ indicates a matrix filled with zeros.

The measurement noise covariance matrix $\mathbf{R}$ is modelled by

$$\mathbf{R} = \mathbf{I}\sigma_m^2, \tag{8.18}$$

where σ_m^2 is the measurement noise variance.

8.2.3 Image Acquisition

We used an ultrasound scanner (SonixTouchRP, Ultrasonix, British Columbia, Canada) with a phased array (SA4-2/24, Ultrasonix, British Columbia, Canada) to acquire images. The imaging depth of the ultrasound system is set to 24 cm and the focus to approximately 3.5 cm. The position and orientation of the ultrasound probe is tracked with an electromagnetic tracking system (trakSTAR, Ascension, Milton, VT). A *Model 90* sensor is taped to the probe and a *Mid-Range* transmitter is used. A frame grabber (DVI2USB 3.0, Epiphan, Ottawa, Ontario, Canada) is used to acquire the images from the ultrasound machine. We run an image acquisition rate of 30 frames/sec and the images are cropped so that only the ultrasound image is acquired resulting in an image size of 648 times 528 pixel. The pixel size was 0.45 mm.

The Plus (Public software Library for UltraSound) library [80] was used to calibrate the tracked images to the tracker coordinate frame and to record the catheter scans.

A 7.5 F *Open-Irrigated* ablation catheter (Blazer™, Boston Scientific, Marlborough, MA) is scanned in a sweeping motion similar as depicted in Fig 8.1. Two sweeps (one forward, one backward) are acquired and the ablation catheter was adjusted so that it is scanned being straight and curved with a bend of approximately 90 degree (see Fig. 8.3a and 8.3b).

(a) (b) (c)

Figure 8.3: A 7.5 F *Open-Irrigated* ablation catheter (Blazer™, Boston Scientific, Marlborough, MA) in straight (8.3a) and curved (8.3b) configuration. An example image of the scanned catheter is shown in 8.3c.

8.2.4 Catheter Detection in Image

We use *OpenCV* [16] in conjunction with *Numpy* [39, 103, 16] to do our image processing tasks. The detection algorithm is manually initialized by providing the position of the catheter cross section in the image (e.g. u_{init} and v_{init}). From this initial cross section an image template of 25 x 25 pixel is generated with u_{init} and v_{init} being in the middle of the template. This template is used to find the best matching area in the next frame using the normalized squared difference as a metric. We update the template by computing a weighted average of the newly found template (10% weight) and the previous template. To adjust slight mismatches caused by long tails of the point spread function (see Fig. 8.3c) we use the intensity centroid of the found matching area as the true catheter position and correct u and v accordingly. An example US image of the scanned catheter is given in Fig. 8.3c.

8.3 Experiments

We used a series of simulations to validate and tune our method. We also conducted in-vitro experiments where we scanned straight and curved ablation catheters with a clinical ultrasound system to verify our technique on real data.

Simulations

We used simulations to validate our catheter tracking approach and to tune some of the parameters, since a ground truth (GT) is readily available.

We apply constraints on some of the parameters to fit to our practical application. We intend to scan the catheter by hand at multiple cross sections similar as sketched in

Fig. 8.1. The hand tries to maintain a constant velocity in the direction perpendicular to the image plane, while keeping the other plane orientation more or less the same. However, due to the tremor of the hand there are also movements in the non-scanning directions, which we model in a slightly oscillating term. From our experiments with a real imaging device we concluded that we usually scanned the catheter with an upper sweep velocity of about 12 mm/sec. In the other two directions we assume a maximum velocity of about 2 mm/sec to simulate the erratic movements of freehand ultrasound. We also applied the oscillatory type of movements to the three rotation angles. The movement pattern can be visually appreciated at Fig. 8.4.

The measurement noise σ_m^2 for the trakSTAR positioning system may depend on environment. Positioning system are usually very susceptible to metal parts as well as other equipment, introducing large uncertainties [92, 79, 57]. From our own experience and from the literature we concluded that assuming zero mean Gaussian noise with a standard deviation of 2.0 mm and 2.0 degrees should appropriately cover most scenarios in clinical practice. We assume that the catheter cross section in the US image has an detection uncertainty in the order of the point spread function. The point spread function especially at the electrodes is rather large extending to 2 to 7 mm. Therefore, we decided to use the same measurement noise term for the image detector as for the position tracking system. This led us to run our experiments with three measurement noise terms ($mathbf{\sigma_m^2} = 0.05$, 2.0, and 4.0) covering a wide range of situations from ideal to worst case scenario encountered in the clinic.

We ran the simulations on straight and bent catheters. The curved catheter was realized by modeling x and y as a quadratic function of z resulting in bends of 60 mm in x and 30 mm in y dimension over a length of 100 mm (z direction). In Fig. 8.5 the catheter is shown.

We established the process variance for proper functioning of our setup experimentally. We varied the process variance σ_p^2 for a rather wide range from 0.1 to 4.0 with logarithmic increments. For each iteration of σ_p^2 we ran five simulation containing 525 measurements and model estimation using the parameter listed above.

Simulations using experimental data

The movements of free hand ultrasound are generally less regular as in our previous simulations. In order to test the ability of tracking a catheter from real data we used scans of straight and curved catheters scanned in a water tank. We adopted the measured positions as the true catheter positions and used this as our ground truth. We corrupted the measurements ($\mathbf{O}$, α, β, γ, u, and v) with additive zero mean Gaussian noise with a variance of 0.05, 2.0, and 4.0.

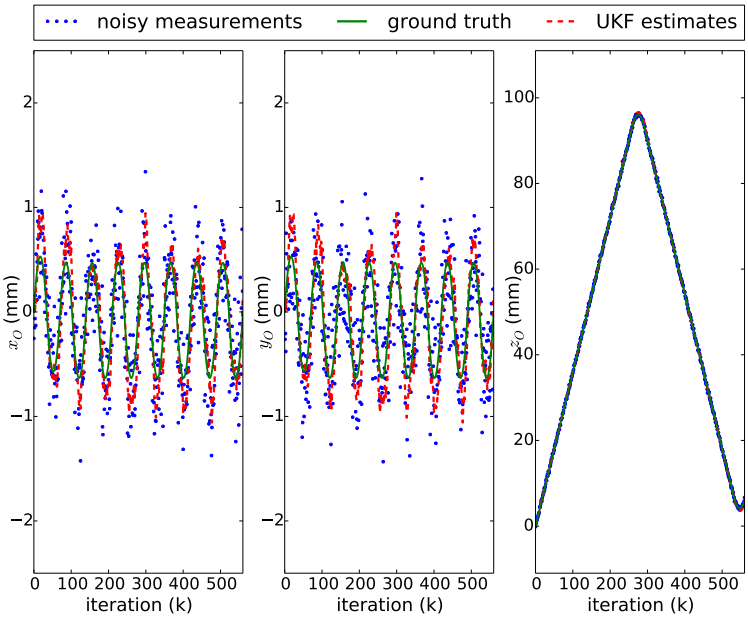

Figure 8.4: Simulated motion pattern used for the optimization. The three components (x, y, z) of the plane position (**O**) plotted as a function of time (k). The simulated catheter is scanned along the z axis whereas the other two components are almost constant. The oscillatory behavior of the x,y components is introduced to mimic the tremor of the hand associated with free hand ultrasound. For this simulation we used a process noise variance of $\sigma_p^2 = 3.0$ and a measurement noise variance of $\sigma_m^2 = 0.1$.

Metrics

We used the mean absolute error (MAE) between the true catheter/plane states and the estimated ones. The MAE is computed by

$$MAE = \frac{1}{NM} \sum_{n=0,m=0}^{n=N,m=M} |x_{n,m} - x_{true_{n,m}}|, \tag{8.19}$$

where $x_{n,m}$ and $x_{true_{n,m}}$ are the estimated/measured and true states with the rows (N≈300 to 600) containing the individual states for one sweep and the columns (M=5)

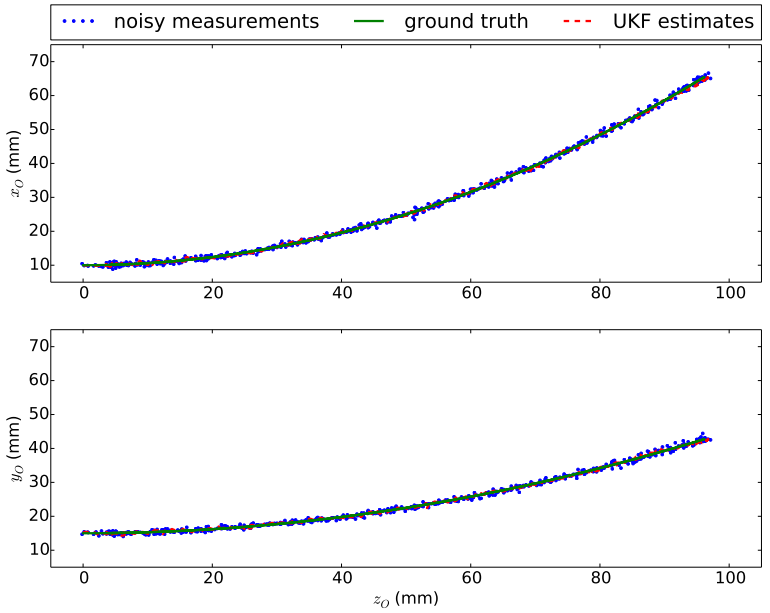

Figure 8.5: Shape of the curved catheter used in simulation. The shown UKF estimates and noisy measurements were generated using a process noise variance of $\sigma_p^2 = 3.0$ and a measurement noise variance of $\sigma_m^2 = 0.1$.

repetitions of the sweeps.

8.4 Results

The optimization results for the simulated straight and curved catheter are shown in Fig. 8.6 and 8.7. The optimization results for the straight and curved experimental catheter scans are shown in Fig. 8.8 and 8.9. In those graphs we plot the MAE of $\mathbf{O}_k$, $[\alpha, \beta, \gamma]_k$, and $\mathbf{p}_k$ as a function of the process noise. The estimates using the UKF are plotted with solid lines while the noisy measurements are plotted with dashed lines. The different measurement noises of 0.05, 2.0, and 4.0 are indicated with dots, asterisk, and crosses respectively. The error bars indicate the standard deviation of the MAE over the five repetitions of the optimization and the markers indicate the mean MAE value.

For the simulated catheters the UKF estimates of the intersection points $\mathbf{P}_k$ are better than the measurements for the higher measurement noise levels. This holds for all settings of the process noise. For the low noise measurements (σ_m^2 of 0.05) this is true as long as the process noise is above 0.4. Generally, process noise variances between 1 and 2 seem to produce good catheter estimation independently from the measurement noise tested.

The optimizations on the experimental catheter scans show similar results than the ones on the simulated catheters. For intermediate and high measurement noise cases the estimates are better than the raw measurements for a process noise variance above 1.5. For the low noise case the estimates of the plane orientation/position and intersection points are slightly worse than the measurements.

In Fig. 8.10 the estimated and measured states are shown for the experimental tracking results of the curved catheter scan. It is quite apparent that a freehand scan is not necessarily very smooth and that there are quite some 'random' accelerations (see $\mathbf{O}_k$ ground truth in Fig. 8.10). In Fig. 8.11 the intersection points of the curved catheter scan are plotted in 3D.

8.5 Discussion

We estimate reasonable parameter values, based on experiments, for our model and tested our results over a wide range of process variances. We tested and tuned our method on simulated and experimental catheter scans successfully. For the simulated catheters the UKF estimates easily outperform state estimates derived purely from noisy measurements. We could also show that the method works well on freehand catheter scans. There are possibilities to use more complex models and to incorporate more sensors with our method, such as the catheter tip position sensing commonly used in EP intervention rooms. This would enable real-time tracking of dynamic catheter movements.

The catheter simulations provide a reliable ground truth but the motion pattern of the image plane is a bit over-simplified. Nevertheless, the overall velocities and the accelerations were picked considering realistic values derived from experimental scans. Therefore, we believe that the process noise values found to work well (in the range of 1.0 to 3.0) are realistic, which is in agreement with our findings for the experimental catheter scans.

To investigate the influence of the movement 'noise' of free hand ultrasound due to jitter and tremor of the operator's hand we used experimental catheter scans as GT. A curved and straight catheter scan served as GT states which we corrupted with additive Gaussian zero mean noise. This gives an realistic motion pattern for the image plane but on the other hand the GT is already corrupted with measurement noise from the tracking system, ultrasound scanner, and image processing. This may explain that we can not obtain better state estimates from the UKF than the measurements for the

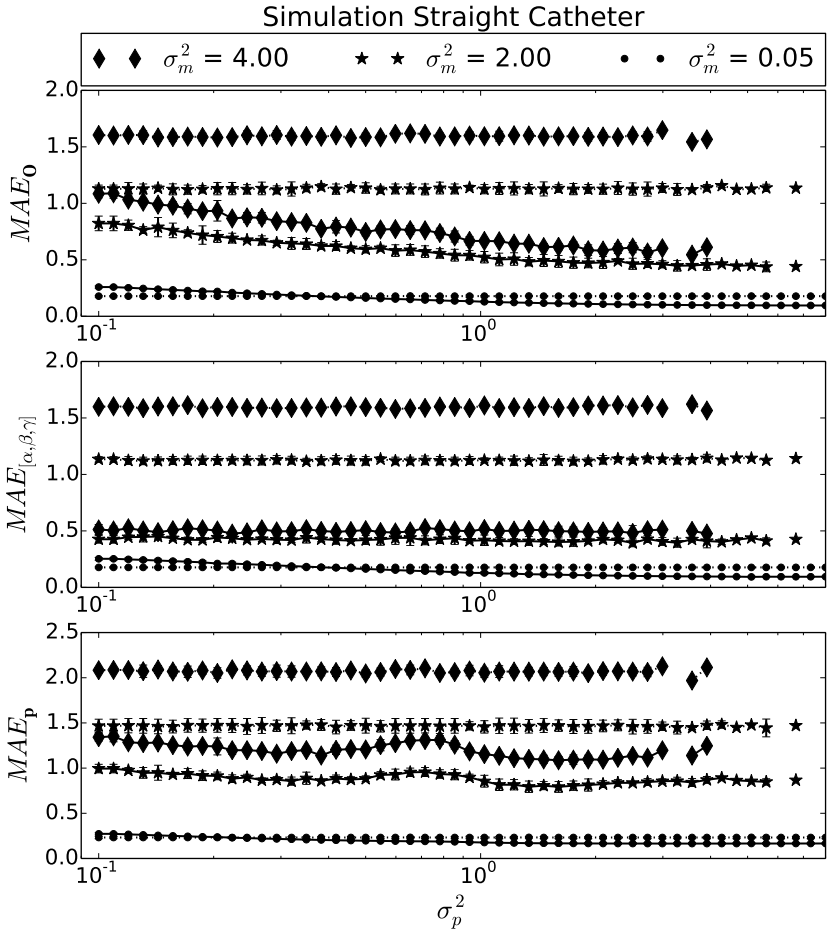

Figure 8.6: Optimization results for a simulated straight Catheter. The process noise (σ_p^2) is shown in a logarithmic scale. The dashed lines represent the noisy measurements and the solid lines the UKF estimates.

low measurement noise case ($\sigma_m^2 = 0.05$). The true positions are probably smoother than what we assume. We believe that the inherent noise of the GT is way higher than the added noise and that an unrealistic high process noise would be necessary

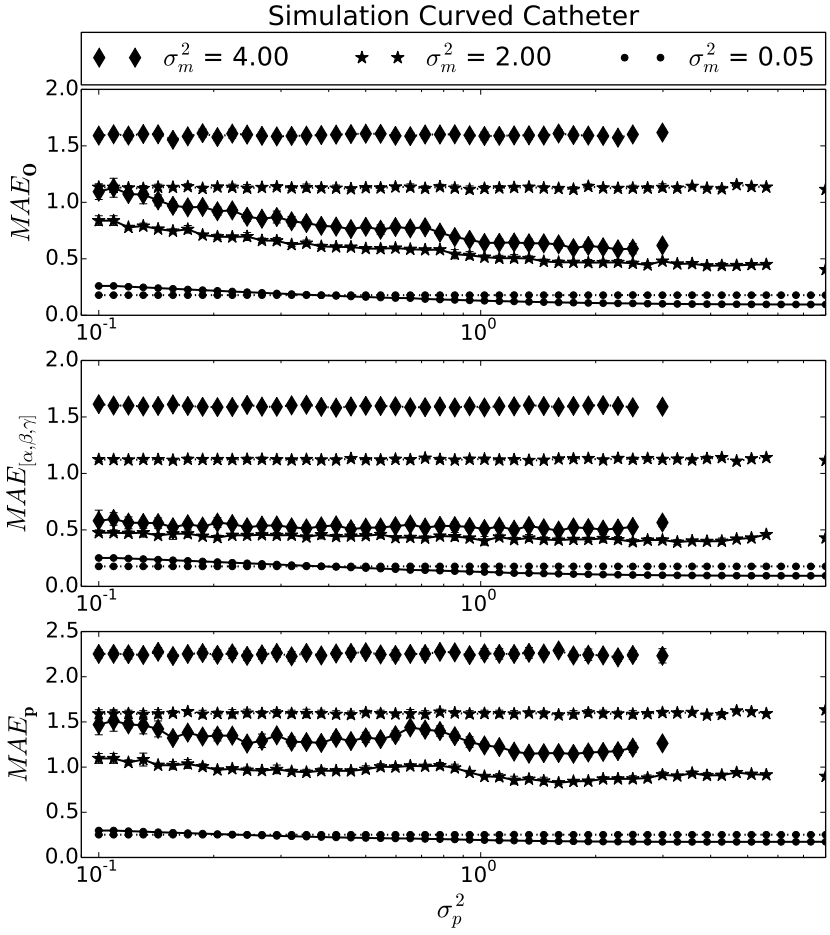

Figure 8.7: Optimization results for a simulated curved Catheter.

for the UKF to generate the same estimates as the noisy GT. However, if the added noise is raised then the UKF outperforms the measurement estimates and we obtain a similar range of optimal process noise.

Another interesting finding is that there is no apparent difference in the process noise between curved and straight catheters. For both the simulated (see Fig. 8.6 and

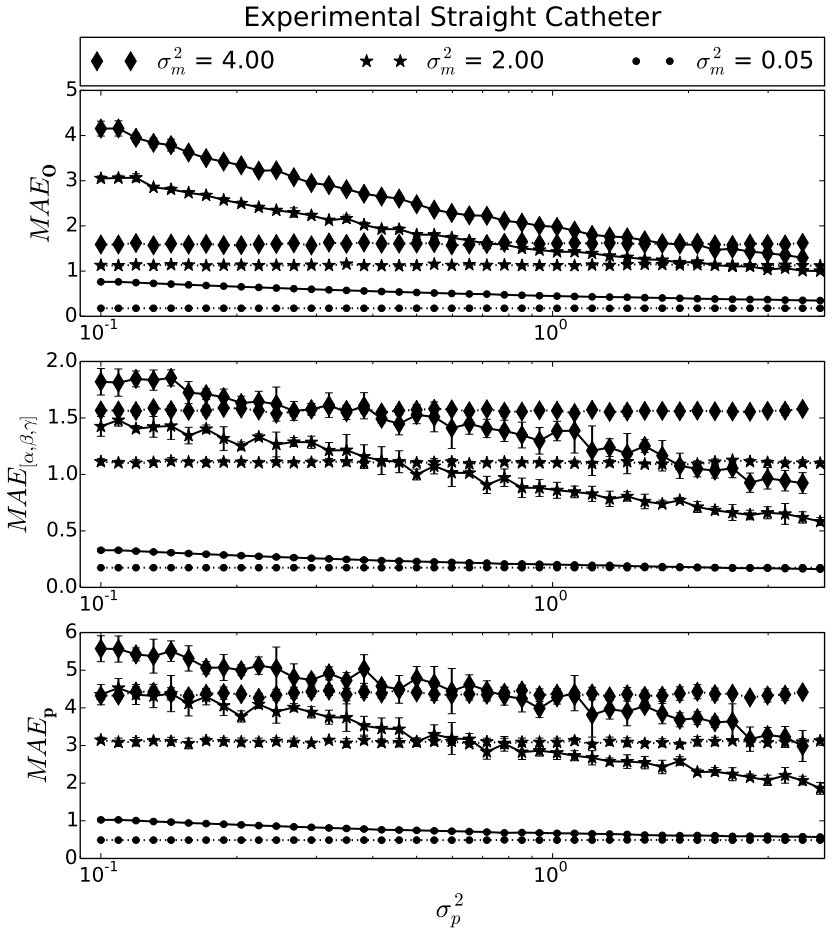

Figure 8.8: Optimization results of a scanned straight Catheter (experimental).

8.7) and scanned catheters (see Fig. 8.8 and 8.9) we did not find any differences in the influence of the process noise. The optimal process noise seems mostly dependent on the motion pattern of the image plane.

This raises also the question if a second order motion model may have been more appropriate to use. However, this is out of the scope of the manuscript and may be

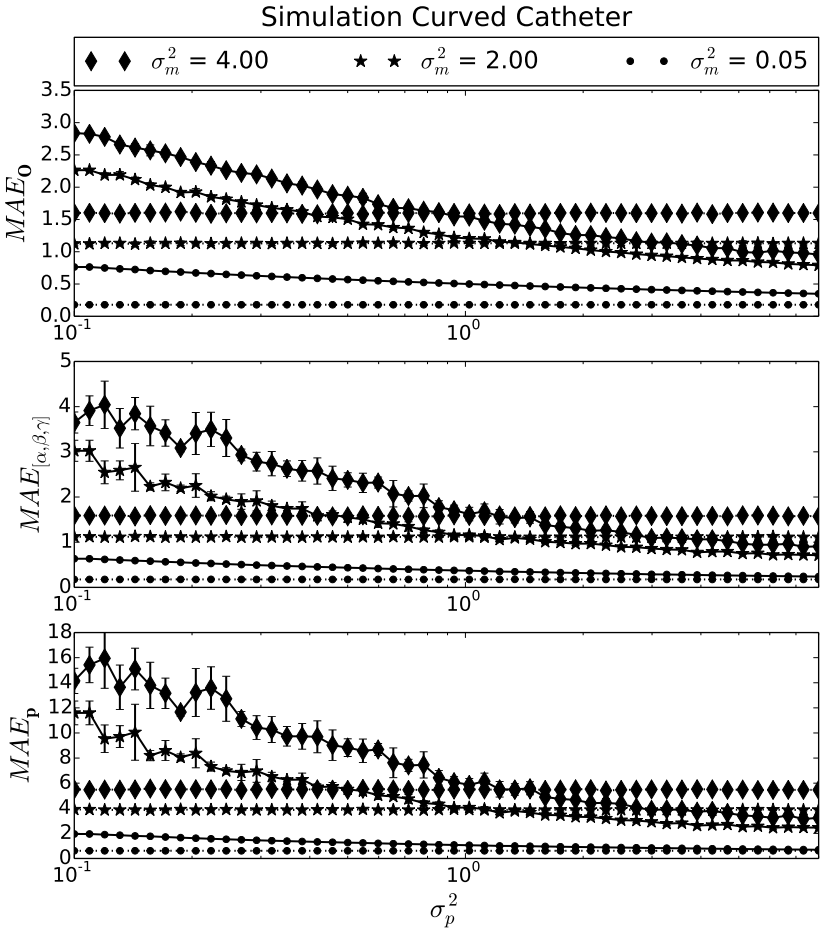

Figure 8.9: Optimization results for a scanned curved Catheter.

investigated in the future.

The biggest limitation of our method at this stage is that it assumes a static catheter. This is certainly not a realistic scenario in clinical practice since the catheter will move around due to the heartbeat and the manipulations of the operator. However, we chose our methods in such a way that extending it to dynamic catheters will be

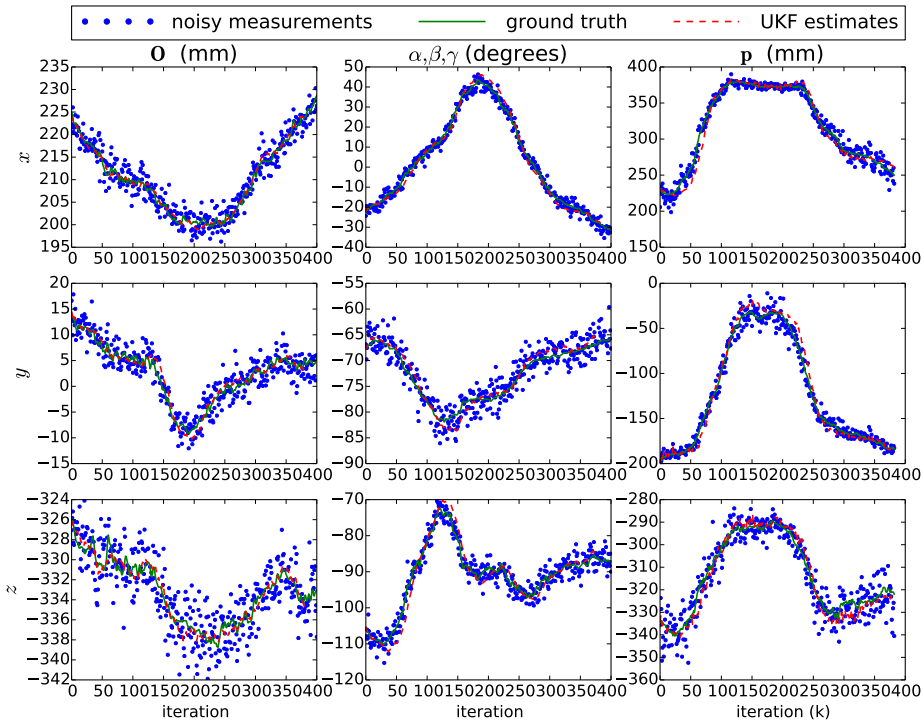

Figure 8.10: Experimental tracking results of the curved catheter scan in a water tank. To generate the noisy measurements we corrupted the ground truth with a additive Gaussian noise with a variance of $\sigma_m^2 = 4.0$. The UKF estimates follow the true plane position and orientation as well as the catheter intersection points well. In this example we used a process noise variance of $\sigma_p^2 = 4.0$. The catheter positions can be appreciated in 3D in Fig. 8.11.

possible.

We will address the catheter dynamics in future work. We envision to combine the information provided by the EAM system in our approach. Usually, the catheter tip location and orientation is provided with such systems and the repetitive temporal motion pattern can easily be derived. The measurements from the catheter tip position and orientation provided by a electromagnetic tracking system could be integrated into

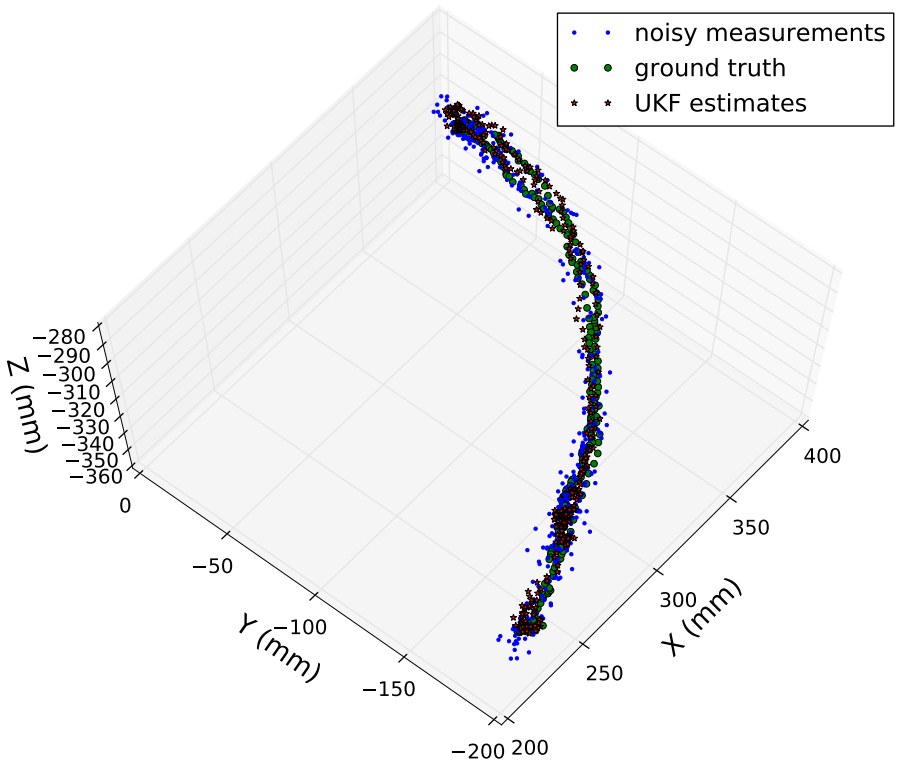

Figure 8.11: Tracked curved ablation catheter positions in 3D. It can be easily seen that the UKF estimates agree well with the true catheter positions.

state vector as described in equation 8.11 (e.g. first order approximation of position and orientation). The tip estimates can be propagated down the catheter to the current image plane and catheter intersection taking into account the mechanical properties of the catheter and its current shape. We believe that our UKF frame work is an

excellent way of integrating this information.

8.6 Conclusion

In this work we could show that using prior knowledge of the device (catheter) in conjunction with an UKF generates better estimates of the catheter location than using pure measurements. We developed a method which is easily extendable for tracking moving catheters.

Intersection Function

$$\mathbf{p}_{k-1} + \lambda \mathbf{v}_k = u \cdot \widehat{\mathbf{u}} + v \cdot \widehat{\mathbf{v}} + \mathbf{O}$$

Equation 8.7 can be rewritten as

$$\lambda \begin{bmatrix} v_1 \\ v_2 \\ v_3 \end{bmatrix} + \begin{bmatrix} p_1 \\ p_2 \\ p_3 \end{bmatrix} = u \cdot \begin{bmatrix} \widehat{u}_1 \\ \widehat{u}_2 \\ \widehat{u}_3 \end{bmatrix} + v \cdot \begin{bmatrix} \widehat{v}_1 \\ \widehat{v}_2 \\ \widehat{v}_3 \end{bmatrix} + \begin{bmatrix} O_1 \\ O_2 \\ O_3 \end{bmatrix}, \tag{8.20}$$

That can be rewritten in a matrix form as:

$$[\widehat{\mathbf{u}}, \widehat{\mathbf{v}}, \mathbf{v}_k] \begin{bmatrix} u \\ v \\ \lambda \end{bmatrix} = \mathbf{p}_0$$

with $\mathbf{p}_0 = [x_0, y_0, z_0]^T = \mathbf{p}_{k-1} - \mathbf{O}$. This linear system can be solved by applying the Cramer's rule as:

$$u = \frac{\begin{vmatrix} x_0, \widehat{v}_1, v_1 \\ y_0, \widehat{v}_2, v_2 \\ z_0, \widehat{v}_3, v_3 \end{vmatrix}}{\begin{vmatrix} \widehat{u}_1, \widehat{v}_1, v_1 \\ \widehat{u}_2, \widehat{v}_2, v_2 \\ \widehat{u}_3, \widehat{v}_3, v_3 \end{vmatrix}}, v = \frac{\begin{vmatrix} \widehat{u}_1, x_0, v_1 \\ \widehat{u}_2, y_0, v_2 \\ \widehat{u}_3, z_0, v_3 \end{vmatrix}}{\begin{vmatrix} \widehat{u}_1, \widehat{v}_1, v_1 \\ \widehat{u}_2, \widehat{v}_2, v_2 \\ \widehat{u}_3, \widehat{v}_3, v_3 \end{vmatrix}}, \lambda = \frac{\begin{vmatrix} \widehat{u}_1, \widehat{v}_1, x_0 \\ \widehat{u}_2, \widehat{v}_2, y_0 \\ \widehat{u}_3, \widehat{v}_3, z_0 \end{vmatrix}}{\begin{vmatrix} \widehat{u}_1, \widehat{v}_1, v_1 \\ \widehat{u}_2, \widehat{v}_2, v_2 \\ \widehat{u}_3, \widehat{v}_3, v_3 \end{vmatrix}} \tag{8.21}$$

thus,

$$u = \frac{x_0(\widehat{v}_2 v_3 - \widehat{v}_3 v_2) - y_0(\widehat{v}_1 v_3 - \widehat{v}_3 v_1) + z_0(\widehat{v}_1 v_2 - \widehat{v}_2 v_1)}{\widehat{u}_1(\widehat{v}_2 v_3 - \widehat{v}_3 v_2) - \widehat{u}_2(\widehat{v}_1 v_3 - \widehat{v}_3 v_1) + \widehat{u}_3(\widehat{v}_1 v_2 - \widehat{v}_2 v_1)}$$

$$v = \frac{-x_0(\widehat{u}_2 v_3 - \widehat{u}_3 v_2) + y_0(\widehat{u}_1 v_3 \widehat{u}_3 v_1) - z_0(\widehat{u}_1 v_2 - \widehat{u}_2 v_1)}{\widehat{u}_1(\widehat{v}_2 v_3 - \widehat{v}_3 v_2) - \widehat{u}_2(\widehat{v}_1 v_3 - \widehat{v}_3 v_1) + \widehat{u}_3(\widehat{v}_1 v_2 - \widehat{v}_2 v_1)}$$

$$\lambda = \frac{x_0(\widehat{u}_2 \widehat{v}_3 - \widehat{u}_3 \widehat{v}_2) - y_0(\widehat{u}_1 \widehat{v}_3 - \widehat{u}_3 \widehat{v}_1) + z_0(\widehat{u}_1 \widehat{v}_2 - \widehat{u}_2 \widehat{v}_1)}{\widehat{u}_1(\widehat{v}_2 v_3 - \widehat{v}_3 v_2) - \widehat{u}_2(\widehat{v}_1 v_3 - \widehat{v}_3 v_1) + \widehat{u}_3(\widehat{v}_1 v_2 - \widehat{v}_2 v_1)}$$

State Transition Matrix and Noise Models

The state transition matrix $\mathbf{F}$ is

$$\mathbf{F} = \begin{bmatrix} \mathbf{A} & \mathbf{0} \\ \mathbf{0} & \mathbf{A} \end{bmatrix} \tag{8.22}$$

with

$$\mathbf{A} = \begin{bmatrix} 1 & 0 & 0 & \Delta t & 0 & 0 \\ 0 & 1 & 0 & 0 & \Delta t & 0 \\ 0 & 0 & 1 & 0 & 0 & \Delta t \\ 0 & 0 & 0 & 1 & 0 & 0 \\ 0 & 0 & 0 & 0 & 1 & 0 \\ 0 & 0 & 0 & 0 & 0 & 1 \end{bmatrix} \tag{8.23}$$

and $\mathbf{0}$ indicating a matrix filled with zeros. and the Covariance of the stochastic process $\mathbf{Q}$ is

$$\mathbf{Q} = \begin{bmatrix} \mathbf{B} & \mathbf{0} \\ \mathbf{0} & \mathbf{B} \end{bmatrix} \tag{8.24}$$

with

$$\mathbf{B} = \begin{bmatrix} 0 & 0 & 0 & 0 & 0 & 0 \\ 0 & 0 & 0 & 0 & 0 & 0 \\ 0 & 0 & 0 & 0 & 0 & 0 \\ 0 & 0 & 0 & \Phi_s & 0 & 0 \\ 0 & 0 & 0 & 0 & \Phi_s & 0 \\ 0 & 0 & 0 & 0 & 0 & \Phi_s \end{bmatrix}, \tag{8.25}$$

where Φ_s is the spectral density of the Gaussian. The image plane process noise covariance $\mathbf{Q}^{\pi}$ computed with equation 8.15 is then

$$\mathbf{Q}^{\pi}(\Delta t) = \begin{bmatrix} \mathbf{C} & \mathbf{0} \\ \mathbf{0} & \mathbf{C} \end{bmatrix} \tag{8.26}$$

with

$$\mathbf{C} = \begin{bmatrix} \frac{\Delta t^3}{3} & 0 & 0 & \frac{\Delta t^2}{2} & 0 & 0 \\ 0 & \frac{\Delta t^3}{3} & 0 & 0 & \frac{\Delta t^2}{2} & 0 \\ 0 & 0 & \frac{\Delta t^3}{3} & 0 & 0 & \frac{\Delta t^2}{2} \\ \frac{\Delta t^2}{2} & 0 & 0 & \Delta t & 0 & 0 \\ 0 & \frac{\Delta t^2}{2} & 0 & 0 & \Delta t & 0 \\ 0 & 0 & \frac{\Delta t^2}{2} & 0 & 0 & \Delta t \end{bmatrix} \Phi_s. \tag{8.27}$$

Chapter 9

Discussion and Conclusion

9.1 Discussion

In this thesis we assess the possibility of using a TEE probe and advanced image processing to support AF ablations. We looked into several methods to generate information of the heart anatomy and the catheters in 3D. In chapter 2 we present how 3D+time reconstruction of the beating heart can be computed from a series of rotated 2D images acquired with the 2D TEE probe. In chapter 3 we show that segmentations of multiple cavities of the heart from single view 3D TEE are possible using a multi-cavity statistical shape model and lead to good segmentation accuracy. This segmentation scheme can be fully automated when combined with our automatic model initialization presented in chapter 4. We investigated the possibility of wide-view image fusion and established a clinical data acquisition protocol for 3D TEE (see chapter 5). In chapter 6, we investigated how well fused images agree with CTA images acquired from the same patients and evaluated if the anatomical landmarks of the LA can be reliably visualized with wide-view TEE images. The results of the heart segmentation using a statistical shape model from wide-view 3D TEE and comparison to single view were presented in chapter 7. A basic catheter tracking approach using swept 2D images based on Kalman filters and catheter models has been investigated in chapter 8 and the results are promising.

Benefits of TEE for EP interventions

TEE imaging is real time and can be used for intra-operative imaging to visualize catheter positions relative to the anatomy. In EP, TEE is routinely used preoperatively for diagnosing blood clots in the LA as well as for estimating the size and proper placement of left atrial appendage closure devices (to just name a few applications). Up to now matrix TEE probes are not well suited for monitoring EP interventions since the relative large size of the probe causes great discomfort for an awake patient. Therefore, these probes can only be used in patients under anesthesia.

The μTEE probe on the other hand, has a very small footprint which allows for transnasal insertion [160]. Patient comfort is better with such an procedure allowing the probe to remain inserted for up to 24 hours [137]. A miniaturized 3D probe would be ideal for monitoring EP interventions, enabling a more densely sampled volume and continuous 3D imaging without reconstructions. Although developments of such a device are in progress it is not available yet. However, we could show that with the μTEE , which was not intended for a fast scan plane rotation, we could still perform 4D image reconstruction at a

reasonable volume rate. Acquisition of rotational 2D images only took a few seconds to provide a sufficiently dense spatiotemporal distribution of frames. Therefore, we believe that already the μTEE may be suitable for monitoring AF ablations and other EP interventions such as placing appendage closure devices by performing quick 3D reconstructions intraoperatively.

Additionally, there is no ionizing radiation associated with diagnostic ultrasound. This would enable a broad use of ultrasound imaging for monitoring interventions without concerns about the patient being exposed to harmful radiation [76]. Furthermore, TEE and μTEE might be an alternative for preoperative CT/MRI since the patient anatomy is well captured with TEE imaging as we showed in chapter 6. This could potentially reduce the radiation exposure of the patient (in case of preoperative CT), reduce costs, and simplify the logistics of AF ablations.

One of the main advantages of TEE imaging compared to ICE is that TEE probes can be used multiple times. This would potentially lower the costs of EP interventions. Additionally, the TEE probes are more stable relative to the heart and do not move with the heart beat such as ICE probes do. Also, steering of the image plane can be controlled much better with TEE.

4D Reconstructions

In our image reconstruction work presented in chapter 2 we tested reconstruction quality of normalized convolution (NC) for a number of different sizes of 2D image sets and compared to nearest neighbor and linear interpolation. The data sets were derived from clinical 3D TEE acquisitions which served also as ground truth. From the 4D TEE set, randomly sampled rotational 2D slices were taken. We could show that NC already produces good quality 3D image reconstructions with only 600 2D images. This would be well in the range of the acquisition rate of the μTEE probe to allow reconstruction "updates" every 6 seconds.

We optimized the reconstruction kernel parameters σ_θ and σ_τ which improved reconstruction quality. However, we feel that there is also some potential to improve image reconstructions by using prior knowledge to adapt the reconstruction kernels [112]. Such prior knowledge could be derived from segmentations providing a map of the anatomy.

Faster computation times of the NC might be obtained by updating already existing reconstructions by new 2D images. We investigated this possibility in our lab and could show promising results on artificial data.

We tested the whole reconstruction pipeline in a lab experiment (see Fig.

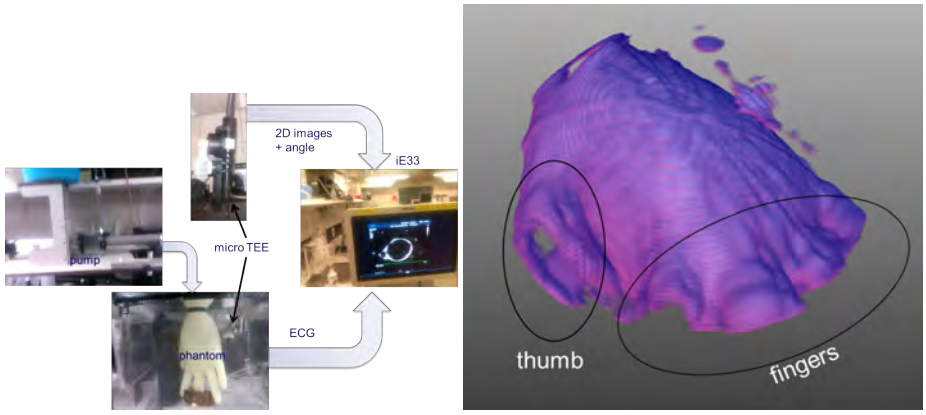

Figure 9.1: Lab experiment mimicking the whole μTEE image acquisition and reconstruction. We used a latex glove connected to a pump simulating a beating heart. An artificial ECG signal was generated and recorded with the ultrasound machine (iE33) as well as 2D images while rotating the scan plan with an actuator. Images were reconstructed using NC. In the reconstruction the base of the fingers and thumb can be appreciated.

9.1). We used a pump to actuate a moving phantom (latex glove) and imaged it with a μTEE probe. ECG signals were generated synchronous with the pump cycle and fed into an iE33 ultrasound machine. The μTEE probes image scan plane was rotated by a programmable actuator (Lego Mindstorms). A reconstruction of the glove phantom is shown in Fig.9.1.

Single-View Segmentation

In chapter 3 we showed that even a limited view of the heart is sufficient to segment five heart cavities if an appropriate anatomical model is used. We used a statistical shape model which was derived from 151 CTA images and we could show that such a model has good generalization and interpolation capabilities. This is a promising result since this means that an anatomical context can be provided even when the clinician's focus is at a narrow region.

Wide-View Image Fusion and Segmentation

In chapter 5 we presented an acquisition protocol aimed at acquiring several 3D TEE views covering the whole LA. We could show that image registration on such data is possible and that subsequent image fusion generates a broad view of the LA anatomy. We compared a total of 8 landmarks by indicating them manually in the wide-view TEEs of 22 patients and in co-registered CTAs of the same patients. We found that most of the landmarks were similarly accurately indicated in both modalities with an average Euclidean distance of 5 ± 3 mm. The left and right upper pulmonary veins which are of interest in AF ablations are visible in 64% and 77% of the wide-view TEE, respectively. The lower PV's however were visualized in just one of the 22 wide-view images. We speculate that the lower PVs are harder to image with TEE since they may be obscured by shadows generated from the lungs.

However, a patient specific anatomical model may help to interpolate such missing areas in the LA anatomy. Such a model could be a statistical shape model as used in chapter 3 or could be derived from rotational X-ray fluoroscopy images, where a tomographic 3D image reconstruction is derived from a series of rotated X-ray images. Additional preoperative MRI or CTA may be helpful as well.

Segmentations derived from wide-view images have improved accuracy of about 5-15% (see chapter 7). This result is expected since more complete data (coverage) should result into a more accurate segmentation. Furthermore, this also indicates that an improved rendering of the heart's anatomy is possible by successively including more and more TEE views. In such a scenario the TEE probe would be used similar to a flash light "illuminating" different parts of the heart while the model is fitted to the combined views to provide anatomical context.

This would combine well with the results from the automatic landmark detection presented in chapter 4. In this work we developed a method to detect three anatomical landmarks which are used to initialize our ASM. We can show that segmentation results for the automatically initialized ASM are as good as manually initialized ASMs. This tool would be of great help for successive segmentation by putting constraints on the detected landmarks to ensure convergence of the ASM model.

Catheter Tracking

In chapter 8 we show that even a simple catheter-image-plane model improves the tracking accuracy compared to tracking estimates only derived from measurements of the electromagnetic tracker. This shows the added value of incorporating prior knowledge into the problem at hand.

Our approach uses an unscented Kalman filter which is quite easily extendable in terms of the model and the measurements used. So far we only modeled static ablation catheters. Straight and curved catheter sections between consecutive image frames were approximated as straight line segments, which already generated good results. However, there are possibilities to extend this model, for instance by modeling the first few centimeters of the catheter by a poly line and incorporating a stiffness term between consecutive points allowing the catheter to be bent. After an initial scan of the catheter the 3D positions of the poly-line points could be initialized and updated in the following scans. The UKF implementation would automatically find the best estimates between the measurements and the model prediction.

Including more measurements (sensors and image based measurements) in the tracking algorithm would be a worthwhile extension of our proposed approach since there are already a multitude available in the EP lab. One has to realize, that in the Kalman framework, combining a measurement with another more noisy measurement can produce better estimates than using only the single low noise measurement. A first natural sensor choice would be the measurements of the catheter tip position and orientation from the tracking system such as the Ensite or Carto systems. These measurements provide a real-time tip position but lack estimates further away from the tip. Discretizing the catheter into a poly line and modeling the bending behavior between sample points as described above could be used to model the catheter dynamics from the tip down towards the handle. The μTEE images will be used to scan the catheter and provide measurement updates. Additionally, incorporating the information from the X-ray fluoroscopy could be useful for additional measurements of the catheter position and shape as well as the μTEE probe and position.

Future work

Even though we showed that different parts of our effort to provide augmented reality for AF interventions using TEE imaging works well, it still has to be shown that the outcome of AF interventions will improve. There are several

steps which could be taken:

- **Replacing preoperative CT/MRI:** A number of AF ablations are done under general anesthesia. For such interventions direct 3D imaging with the larger matrix TEE probe would be feasible and segmentations of the heart could be directly generated and replace the preoperative segmentations. We showed that reconstructions derived from the μTEE are suitable for replacing the matrix TEE. However, this needs still to be shown directly within a clinical study. There, it should also be investigated if segmentations derived from the 4D reconstructions or directly from the 2D image data are accurate enough for clinical practice.

- **Tracking of ablation catheters:** We showed that a simple catheter model combined with a Kalman filter generates better position and catheter shape estimates than using only the raw measurements. This scheme is robust and fast and could be tested relatively easily on clinical data. Furthermore, this scheme is quite easily extendable in terms of the catheter model and in terms of sensor and image derived measurements and also to include temporal motion patterns of the catheter due to the heartbeat. Extending the catheter model by incorporating the bending properties of the catheter as well as the input from the catheter steering could reflect the catheter more realistically. The catheter tip locations derived from the EP tracking systems could be integrated in such a model as well as location measurements derived from x-ray images.

- **Robotic control of μTEE probe:** The EP intervention room is already very crowded and adding a sonographer for controlling the TEE probe would be suboptimal. Additionally, this would increase costs and this extra person is also exposed to x-ray radiation. Therefore, it would be worthwhile to use a robot for steering the TEE probe during interventions similar as it is already done for catheter control [125]. Several modes of operations would be attractive. When using a μTEE probe, rotating the image plane for continuous 4D image reconstructions would be desirable. Further, sweeping the heart for wide-view image fusion and segmentation could be another mode of operation. Lastly, following the catheter during ablation showing the catheter in the 2D image or sampling a small subvolume including the catheter and the ablation region for enabling image reconstructions and realtime tracking. Such a approach would be similar to a torch illuminating only the region of interest and could help the clinician greatly.

9.2 Conclusion

In this thesis we could show that the μTEE probe offers possibilities for monitoring EP interventions and test all necessary software and image processing tools for generating an AF ablation augmentation showing the catheters in the anatomical context in a quasi real-time fashion. We showed that the 2D images of the μTEE probe can be used to reconstruct a time series of 3D images as well as to track catheters. NC handled the irregularly sampled data of the beating heart well and a relative small 2D image set was sufficient to generate good quality reconstructions. The majority of the LA can be imaged with TEE imaging and important LA anatomy can be reliably identified. Accurate anatomical augmentations can be generated by fitting statistical shape models to single and wide-view 3D TEE data. We developed a robust automatic model initialization which renders our segmentation approach fully automatic. Lastly, we showed a robust and simple way to track catheters and estimate there shape and position. With all these tools an augmented catheter and heart surface model can be created. This provides the EP physician with the navigational tools to generate potentially better outcomes of AF ablations. Furthermore, the improved visualization of catheters and ablation regions potentially decreases the demands on operator skill and reduces intervention times. Additionally, the TEE probes can be used multiple times with a cost advantage compared to single-use ICE. Preoperative CT/MRI may be replaced by 3D TEE, reducing costs, logistic complexity, and radiation dose for the patients. With this work we showed that a virtual reality of ablation catheters in anatomical context can be achieved based on μTEE images, which possibly improve the outcome of EP interventions.

Bibliography

[1] http://professional.sjm.com/products/ep/mapping-visualization/disposable-products/ensite-navx-navigation-visualization-technology.

[2] N. Abolhassani, R. Patel, and M. Moallem. Needle insertion into soft tissue: A survey. *Medical Engineering & Physics*, 29(4):413 – 431, 2007.

[3] Alyson Ames and William G. Stevenson. Catheter ablation of atrial fibrillation. *Circulation*, 113(13):e666–e668, 2006.

[4] E Artuso, B Stomaci, R Verlato, P Turrini, N Lafisca, M S Baccillieri, A Di Marco, and P Piovesana. Transesophageal echocardiographic follow-up of pulmonary veins in patients undergoing ostial radiofrequency catheter ablation for atrial fibrillation. *Ital Heart J*, 6(7):595–600, 2005.

[5] K. S. Arun, T. S. Huang, and S. D. Blostein. Least-squares fitting of two 3-d point sets. *IEEE Transactions on Pattern Analysis and Machine Intelligence*, PAMI-9(5):698 –700, sept. 1987.

[6] S. Arya, D. M. Mount, N. S. Netanyahu, R. Silverman, and A. Wu. An optimal algorithm for approximate nearest neighbor searching. *J. ACM*, 45:891–923, 1998.

[7] N. Baka, B.L. Kaptein, J.E. Giphart, M. Staring, M. de Bruijne, B.P.F. Lelieveldt, and E. R. Valstar. Evaluation of automated statistical shape model based knee kinematics from biplane fluoroscopy. *Journal of Biomechanics*, 2013.

[8] Dana H Ballard. Generalizing the hough transform to detect arbitrary shapes. *Pattern recognition*, 13(2):111–122, 1981.

[9] S Bangalore, S S Yao, and F A Chaudhry. Role of left atrial size in risk stratification and prognosis of patients undergoing stress echocardiography. *J Am Coll Cardiol*, 50(13):1254–1262, 2007.

[10] Daniel Barbosa, Thomas Dietenbeck, Brecht Heyde, Helene Houle, Denis Friboulet, Jan D'hooge, and Olivier Bernard. Fast and fully automatic 3-d echocardiographic segmentation using b-spline explicit active surfaces: Feasibility study and validation in a clinical setting. 39(1):89–101, 2013.

[11] P. J. Besl and H. D. Mckay. A method for registration of 3-d shapes. *IEEE Transactions on Pattern Analysis and Machine Intelligence*, 14(2):239–256, 1992.

[12] J. Martin Bland and DouglasG. Altman. Statistical methods for assessing agreement between two methods of clinical measurement. *The Lancet*, 327(8476):307 – 310, 1986.

[13] N. Bom, C. T. Lancee, J. Honkoop, and P. G. Hugenholtz. Ultrasonic viewer for cross-sectional analyses of moving cardiac structures. *Biomed Eng.*, 6(0006-2898 (Linking)):500–508, 1971.

[14] Johan G. Bosch, Marijn van Stralen, Marco M. Voormolen, Boudewijn J. Krenning, Charles T. Lancée, Johan H. C. Reiber, Anton F. W. van der Steen, and Nico de Jong. Novel spatiotemporal voxel interpolation with multibeat fusion for 3d echocardiography with irregular data distribution. In *Proc. SPIE 6147, 61470Q*, 2006.

[15] Boston Scientific. *The WATCHMAN Left Atrial Appendage Closure Device is a proven alternative to long-term warfarin therapy for stroke risk reduction in patients with atrial fibrillation.*

[16] G. Bradski. *Dr. Dobb's Journal of Software Tools*, 2000.

[17] Anthony G. Brooks, Martin K. Stiles, Julien Laborderie, Dennis H. Lau, Pawel Kuklik, Nicholas J. Shipp, Li-Fern Hsu, and Prashanthan Sanders. Outcomes of long-standing persistent atrial fibrillation ablation: A systematic review. *Heart Rhythm*, 7(6):835–846, 2010.

[18] R. G. Brown and P. Y. C. Hwang. *Introduction to Random Signals and Applied Kalman Fitlering.* John Wiley & Sons, 1997.

[19] E. Buonocore and G. J. Skipper. Steerable real-time sonographically guided needle biopsy. *American Journal of Roentgenology*, 136(2):387–392, February 1981.

[20] C.B. Burckhardt. Speckle in ultrasound b-mode scans. *Sonics and Ultrasonics, IEEE Transactions on*, 25(1):1–6, Jan 1978.

[21] P Burlina, C Sprouse, R Mukherjee, D DeMenthon, and T Abraham. Patient-specific mitral valve closure prediction using 3d echocardiography. 39(5):769–783, 2013.

[22] Philippe Burlina, Ryan Mukherjee, Radford Juang, and Chad Sprouse. Recovering endocardial walls from 3d tee. In *Functional Imaging and Modeling of the Heart*, pages 284–293, 2011.

[23] Hugh Calkins, Josep Brugada, Douglas L. Packer, Riccardo Cappato, Shih-Ann Chen, Harry J.G. Crijns, Ralph J. Damiano, D. Wyn Davies, David E. Haines, Michel Haissaguerre, Yoshito Iesaka, Warren Jackman, Pierre Jais, Hans Kottkamp, Karl Heinz Kuck, Bruce D. Lindsay, Francis E. Marchlinski, Patrick M. McCarthy, J. Lluis Mont, Fred Morady, Koonlawee Nademanee, Andrea Natale, Carlo Pappone, Eric Prystowsky, Antonio Raviele, Jeremy N. Ruskin, Richard J. Shemin, Hugh Calkins, Josep Brugada, , , Shih-Ann Chen, , Eric N. Prystowsky, , Karl Heinz Kuck, , Andrea Natale, , David E. Haines, , Francis E. Marchlinski, , Hugh Calkins, , D. Wyn Davies, , Bruce D. Lindsay, , Patrick M. McCarthy, , Douglas L. Packer, , Riccardo Cappato, Harry J.G. Crijns, Ralph J. Damiano, Michel Haissaguerre, Warren M. Jackman, Pierre Jais, Yoshito Iesaka, Hans Kottkamp, Lluis Mont, Fred Morady, Koonlawee Nademanee, Carlo Pappone, Antonio Raviele, Jeremy N. Ruskin, and Richard J. Shemin. Hrs/ehra/ecas expert consensus statement on catheter and surgical ablation of atrial fibrillation: Recommendations for personnel, policy, procedures and follow-up. *Europace*, 9(6):335–379, 2007.

[24] R. Cappato, H. Calkins, S. A. Chen, Y. Davies, W.and Iesaka, J. Kalman, Y. H. Kim, G. Klein, D. Packer, and A. Skanes. Worldwide survey on the methods, efficacy, and safety of catheter ablation for human atrial fibrillation. *Circulation*, 111(9):1100–1105, 2005.

[25] R. S. C. Cobbold. *Foundations of Biomedical Ultrasound*. Oxford University Press, 2006.

[26] T.F. Cootes, D. Cooper, C.J. Taylor, and J. Graham. Active shape models - their training and application. *Computer Vision and Image Understanding*, 61(1):38–59, 1995.

[27] T.F. Cootes, G.J. Edwards, and C.J. Taylor. Active appearance models. 23(6):681–685, 2001.

[28] T.F. Cootes, Andrew Hill, Christopher J Taylor, and Jane Haslam. Use of active shape models for locating structures in medical images. *Image and vision computing*, 12(6):355–365, 1994.

[29] T.F. Cootes, C.J. Taylor, D.H. Cooper, and J. Graham. Active shape models-their training and application. 61(1):38–59, 1995.

[30] Timothy F Cootes, Christopher J Taylor, David H Cooper, and Jim Graham. Training models of shape from sets of examples. In *Proc. British Machine Vision Conference*, pages 9–18. Springer London, 1992.

[31] J.L. Cox, R.B. Schuessler, H.J. D'Agostino Jr., C.M. Stone, B.-C. Chang, M.E. Cain, P.B. Corr, and J.P. Boineau. The surgical treatment of atrial fibrillation: Iii. development of a definitive surgical procedure. *Journal of Thoracic and Cardiovascular Surgery*, 101(4):569–583, 1991. cited By 667.

[32] Ariel H. Curiale, Alexander Haak, Gonzalo Vegas-Sánchez-Ferrero, Ben Ren, Santiago Aja-Fernández, and Johan G. Bosch. Fully automatic detection of salient features in 3-d transesophageal images. *Ultrasound in Medicine & Biology*, (0):(in press), 2014.

[33] Ariel Hernán Curiale, Gonzalo Vegas-Sánchez-Ferrero, and Santiago Aja-Fernández. Speckle tracking in interpolated echocardiography to estimate heart motion. volume 7945 of *Lecture Notes in Computer Science*, pages 325 – 333. Springer Berlin Heidelberg, 2013.

[34] Jeanne M. DeCara, Eran Toledo, Ivan S. Salgo, Georgeanne Lammertin, Lynn Weinert, and Roberto M. Lang. Evaluation of left ventricular systolic function using automated angle-independent motion tracking of mitral annular displacement. *Journal of the American Society of Echocardiography*, 18(12):1266 – 1269, 2005.

[35] Lee R. Dice. Measures of the amount of ecologic association between species. *Ecology*, 26(3):pp. 297–302, 1945.

[36] S.P. DiMaio and S.E. Salcudean. Needle insertion modeling and simulation. *Robotics and Automation, IEEE Transactions on*, 19(5):864–875, Oct 2003.

[37] J. Dong, H. Calkins, S. B. Solomon, S. Lai, D. Dalal, A. Lardo, E. Brem, A. Preiss, R. D. Berger, H. Halperin, and T. Dickfeld. Integrated electroanatomic mapping with three-dimensional computed tomographic images for real-time guided ablations. *Circulation*, 113(2):186–194, 2006.

[38] J Dong, T Dickfeld, D Dalal, A Cheema, C R Vasamreddy, C A Henrikson, J E Marine, H R Halperin, R D Berger, J A Lima, D A Bluemke, and H Calkins. Initial experience in the use of integrated electroanatomic mapping with three-dimensional MR/CT images to guide catheter ablation of atrial fibrillation. *J Cardiovasc Electrophysiol*, 17(5):459–466, 2006.

[39] P. F. Dubois, Konrad H., and James H. Numerical python. *Computers in Physics*, 10(3), May/June 1996.

[40] R. M. Dudley. *Uniform Central Limit Theorems*. Cambridge University Press, The Pitt Building, Trumpington Street, Cambridge CB2 IRP, 1st edition, 1999.

[41] F F Faletra, S Castro, N G Pandian, I Kronzon, H J Nesser, and S Y Ho. *Atlas of Real Time 3D Transesophageal Echocardiography*. Springer, London, 2010.

[42] F F Faletra, S Y Ho, F Regoli, M Acena, and A Auricchio. Real-time three dimensional transoesophageal echocardiography in imaging key anatomical structures of the left atrium: potential role during atrial fibrillation ablation. *Heart*, 99(2):133–142, 2013.

[43] William M. Feinberg, Joseph L. Blackshear, Andreas Laupacis, Richard Kronmal, and Robert G. Hart. Prevalence, age distribution, and gender of patients with atrial fibrillation: Analysis and implications. *Arch Intern Med*, 155(5):469–473, 1995.

[44] F.A. Flachskampf, L. Badano, W.G. Daniel, R.O. Feneck, K.F. Fox, Alan G. Fraser, Agnes Pasquet, M. Pepi, L. Perez de Isla, J.L. Zamorano, Document Reviewers:, J.R.T.C. Roelandt, and L. Piérard. Recommendations for transoesophageal echocardiography: update 2010. 11(7):557–576, 2010.

[45] Gang Gao, Graeme P. Penney, YingLiang Ma, Nicolas Gogin, Pascal Cathier, Aruna Arujuna, Geraint Morton, Dennis Caulfield, Jaswinder S. Gill, C. Aldo Rinaldi, Jane Hancock, Simon Redwood, Martyn Thomas, Reza Razavi, Geert Gijsbers, and Kawal S. Rhode. Registration of 3d trans-esophageal echocardiography to x-ray fluoroscopy using image-based probe tracking. *Medical Image Analysis*, 16(1):38–49, 2012.

[46] Rocío García-Orta, Eduardo Moreno, Matilde Vidal, Fuensanta Ruiz-López, José M. Oyonarte, Juan Lara, Teodoro Moreno, Miguel A. García-Fernándezd, and José Azpitarte. Three-dimensional versus two-dimensional transesophageal echocardiography in mitral valve repair. 20(1):4–12, 2007.

[47] Lior Gepstein, Gal Hayam, and Shlomo A. Ben-Haim. A novel method for nonfluoroscopic catheter-based electroanatomical mapping of the heart: In vitro and in vivo accuracy results. *Circulation*, 95(6):1611–1622, 1997.

[48] Benoit Ghaye, David Szapiro, Jean-Nicolas Dacher, Luz-Maria Rodriguez, Carl Timmermans, David Devillers, and Robert F. Dondelinger. Percutaneous ablation for atrial fibrillation: The role of cross-sectional imaging. *Radiographics*, 23(1):19–33, 2003.

[49] Alan S. Go, Elaine M. Hylek, Kathleen A. Phillips, YuChiao Chang, Lori E. Henault, Joe V. Selby, and Daniel E. Singer. Prevalence of diagnosed atrial fibrillation in adults. *JAMA: The Journal of the American Medical Association*, 285(18):2370–2375, 2001.

[50] Julia Grapsa, Declan P. O'Regan, Harry Pavlopoulos, Giuliana Durighel, David Dawson, and Petros Nihoyannopoulos. Right ventricular remodelling in pulmonary arterial hypertension with three-dimensional echocardiography: comparison with cardiac magnetic resonance imaging. 11(1):64–73, 2010.

[51] A. Haak, M. van Stralen, G. van Burken, S. Klein, J.P.W. Pluim, N. de Jong, A.F.W. van der Steen, and J.G. Bosch. Spatiotemporal interpolation by normalized convolution for 4d transesophageal echocardiography. In *International Ultrasonics Symposium - IUS2011*, 2011.

[52] Alexander Haak, Gonzalo Vegas-Sanchez-Ferrero, Harriët H. Mulder, Hortense H. Kirişli, Nora Baka, Coert Metz, Stefan Klein, Ben Ren, Gerard van Burken, Antonius F.W. van der Steen, Josien P.W. Pluim, Theo

van Walsum, and Johan G. Bosch. Simultaneous segmentation of multiple heart cavities in 3d transesophageal echocardiograms. In *2013 Joint UFFC, EFTF and PFM Symposium*, 2013.

[53] Alexander Haak, Gonzalo Vegas-Sanchez-Ferrero, Harriët H Mulder, Hortense A Kirisli, Nora Baka, Coert Metz, Stefan Klein, Ben Ren, Gerard van Burken, Antonius FW van der Steen, J.P.W. Pluim, T. van Walsum, and J.G. Bosch. Segmentation of 3d transesophageal echocardiograms by multi-cavity active shape model and gamma mixture model. In Hongen Liao, CristianA. Linte, Ken Masamune, TerryM. Peters, and Guoyan Zheng, editors, *Augmented Reality Environments for Medical Imaging and Computer-Assisted Interventions*, volume 8090 of *Lecture Notes in Computer Science*, pages 19–26. Springer Berlin Heidelberg, 2013.

[54] Robert M Haralick, Layne T Watson, and Thomas J Laffey. The topographic primal sketch. *The International Journal of Robotics Research*, 2(1):50–72, 1983.

[55] John A Hartigan and Manchek A Wong. Algorithm as 136: A k-means clustering algorithm. *Applied statistics*, pages 100–108, 1979.

[56] Sébastien Hascoët, Gilles Brierre, Guillaume Caudron, Christelle Cardin, Vanina Bongard, and Philippe Acar. Assessment of left ventricular volumes and function by real time three-dimensional echocardiography in a pediatric population: A tomtec versus qlab comparison. *Echocardiography*, 27(10):1263–1273, 2010.

[57] M Hastenteufel, M Vetter, HP Meinzer, and I Wolf. Effect of 3d ultrasound probes on the accuracy of electromagnetic tracking systems. *Ultrasound in medicine & biology*, 32(0301-5629 (Linking)):1359–68, 2006.

[58] Jan Heeringa, Deirdre A.M. van der Kuip, Albert Hofman, Jan A. Kors, Gerard van Herpen, Bruno H.Ch. Stricker, Theo Stijnen, Gregory Y.H. Lip, and Jacqueline C.M. Witteman. Prevalence, incidence and lifetime risk of atrial fibrillation: the rotterdam study. *European Heart Journal*, 27(8):949–953, April 2006.

[59] Tobias Heimann and Hans-Peter Meinzer. Statistical shape models for 3d medical image segmentation: A review. *Medical Image Analysis*, 13(4):543 – 563, 2009.

[60] E K Heist, F Perna, F Chalhoub, S Danik, C Barrett, C Houghtaling, C Tondo, S Mahapatra, J Ruskin, and M Mansour. Comparison of electroanatomical mapping systems: accuracy in left atrial mapping. *Pacing Clin Electrophysiol*, 36(5):626–631, 2013.

[61] W L Henry, J Morganroth, A S Pearlman, C E Clark, D R Redwood, S B Itscoitz, and S E Epstein. Relation between echocardiographically determined left atrial size and atrial fibrillation. *Circulation*, 53(2):273–279, 1976.

[62] Ziyad M Hijazi, Kalyanam Shivkumar, and David J Sahn. Intracardiac echocardiography (ice) during interventional & electrophysiological cardiac catheterization. *Circulation*, 119(4):587–596, February 2009.

[63] S Y Ho, K P McCarthy, and F F Faletra. Anatomy of the left atrium for interventional echocardiography. *Eur J Echocardiogr*, 12(10):i11–5, 2011.

[64] Siew Yen Ho. Structure and anatomy of the aortic root. 10(1):i3–i10, 2009.

[65] Berthold K. P. Horn, H.M. Hilden, and Shariar Negahdaripour. Closed-form solution of absolute orientation using orthonormal matrices. *Journal of the Optical Society America*, 5(7):1127–1135, 1988.

[66] R.I. Ionasec, I. Voigt, B. Georgescu, Yang Wang, H. Houle, F. Vega-Higuera, N. Navab, and D. Comaniciu. Patient-specific modeling and quantification of the aortic and mitral valves from 4-d cardiac ct and tee. *IEEE Transactions on Medical Imaging*, 29(9):1636–1651, 2010.

[67] Anil K Jain, Yu Zhong, and Marie-Pierre Dubuisson-Jolly. Deformable template models: A review. 71(2):109 – 129, 1998.

[68] S. J. Julier and J. K. Uhlmann. New extension of the kalman filter to nonlinear systems. In I. Kadar, editor, *Signal Processing, Sensor Fusion, and Target Recognition VI*, volume 3068 of *Society of Photo-Optical Instrumentation Engineers (SPIE) Conference Series*, July 1997.

[69] R. E. Kalman. A new approach to linear filtering and prediction problems. *J. Basic Engineering*, 82(1):35, 1960.

[70] Michael Kass, Andrew Witkin, and Demetri Terzopoulos. Snakes: Active contour models. 1(4):321–331, 1998.

[71] R Kato, L Lickfett, G Meininger, T Dickfeld, R Wu, G Juang, P Angkeow, J LaCorte, D Bluemke, R Berger, H R Halperin, and H Calkins. Pulmonary vein anatomy in patients undergoing catheter ablation of atrial fibrillation: lessons learned by use of magnetic resonance imaging. *Circulation*, 107(15):2004–2010, 2003.

[72] D. R. Kaye, D. Stoianovici, and M. Han. Robotic ultrasound and needle guidance for prostate cancer management: Review of the contemporary literature. *Current opinion in urology*, 24(1):75–80, January 2014.

[73] H.A. Kirişli, M. Schaap, S. Klein, S.L. Papadopoulou, M. Bonardi, C.H. Chen, A.C. Weustink, N.R.A. Mollet, E. P. A. Vonken, R.J. van der Geest, T. van Walsum, and W.J. Niessen. Evaluation of a multi-atlas based method for segmentation of cardiac cta data: a large-scale, multi-center and multi-vendor study. *Medical Physics*, 37(12):6279–6292, 2010.

[74] S. Klein, M. Staring, K. Murphy, M.A. Viergever, and J.P.W. Pluim. elastix: A toolbox for intensity-based medical image registration. *Medical Imaging, IEEE Transactions on*, 29(1):196–205, Jan 2010.

[75] Hans Knutsson and Carl-Fredrik Westin. Normalized and differential convolution: methods for interpolation and filtering of incomplete and uncertain data. In *IEEE Computer Society Conf. Computer Vision and Pattern Recognition*, pages 515–523, 1993.

[76] Pramesh Kovoor, Michelle Ricciardello, Lee Collins, John B. Uther, and David L. Ross. Risk to patients from radiation associated with radiofrequency ablation for supraventricular tachycardia. *Circulation*, 98(15):1534–1540, 1998.

[77] R M Lang, L P Badano, W Tsang, D H Adams, E Agricola, T Buck, F F Faletra, A Franke, J Hung, L P de Isla, O Kamp, J D Kasprzak, P Lancellotti, T H Marwick, M L McCulloch, M J Monaghan, P Nihoyannopoulos, N G Pandian, P A Pellikka, M Pepi, D A Roberson, S K Shernan, G S Shirali, L Sugeng, F J Ten Cate, M A Vannan, J L Zamorano, and W A Zoghbi. EAE/ASE recommendations for image acquisition and display using three-dimensional echocardiography. *J Am Soc Echocardiogr*, 25(1):3–46, 2012.

[78] Roberto M. Lang, Michelle Bierig, Richard B. Devereux, Frank A. Flachskampf, Elyse Foster, Patricia A. Pellikka, Michael H. Picard, Mary J.

Roman, James Seward, Jack S. Shanewise, Scott D. Solomon, Kirk T. Spencer, Martin St John Sutton, and William J. Stewart. Recommendations for chamber quantification: A report from the american society of echocardiography's guidelines and standards committee and the chamber quantification writing group, developed in conjunction with the european association of echocardiography, a branch of the european society of cardiology. *Journal of the American Society of Echocardiography*, 18(12):1440 – 1463, 2005.

[79] S. LaScalza, J. Arico, and R. Hughes. Effect of metal and sampling rate on accuracy of flock of birds electromagnetic tracking system. *Journal of biomechanics*, 36(1):141–4, Jan 2003.

[80] A. Lasso, T Heffter, A. Rankin, C. Pinter, T. Ungi, and G. Fichtinger. Plus: Open-source toolkit for ultrasound-guided intervention systems. *IEEE Transactions on Biomedical Engineering*, (10):2527–2537, Oct 2014.

[81] K.Y. Esther Leung and Johan G. Bosch. Automated border detection in three-dimensional echocardiography: principles and promises. *European Journal of Echocardiography*, 11(2):97–108, 2010.

[82] Marius George Linguraru, Nikolay V. Vasilyev, Pedro J. Del Nido, and Robert D. Howe. Statistical segmentation of surgical instruments in 3-d ultrasound images. 33(9):1428 – 1437, 2007.

[83] D. C. Liu and J. Nocedal. On the limited memory bfgs method for large scale optimization. *Math. Program.*, 45(3):503–528, December 1989.

[84] William E. Lorensen and Harvey E. Cline. Marching cubes: A high resolution 3d surface construction algorithm. *Computer Graphics*, 21(4):163–169, 1987.

[85] ZACHARY J. Malchano, PETR Neuzil, Ricardo C. Cury, GODTFRED Holmvag, JIRI Weichelt, EHUD J. Schmidt, JEREMY N. Ruskin, and VIVEK Y. Reddy. Integration of cardiac CT/MR imaging with three-dimensional electroanatomical mapping to guide catheter manipulation in the left atrium: Implications for catheter ablation of atrial fibrillation. *Journal of Cardiovascular Electrophysiology*, 17(11):1221–1229, 2006.

[86] J F Malouf, W D Edwards, A Jamil Tajik, and J B Seward. Function anatomy of the heart. In V Fuster, R Wayne Alexander, and R A

O'Rourke, editors, *Hurst's the Heart. 10th Edition*, pages 49–51. McGraw-Hill, McGraw-Hill, 2001.

[87] Jonathan Mamou and Michael L. Oelze, editors. *Quantitative Ultrasound in Soft Tissues*. Springer, 2013.

[88] N F Marrouche, D O Martin, O Wazni, A M Gillinov, A Klein, M Bhargava, E Saad, D Bash, H Yamada, W Jaber, R Schweikert, P Tchou, A Abdul-Karim, W Saliba, and A Natale. Phased-array intracardiac echocardiography monitoring during pulmonary vein isolation in patients with atrial fibrillation: impact on outcome and complications. *Circulation*, 107(21):2710–2716, 2003.

[89] B. A. McElhoe. An assessment of the navigation and course corrections for a manned flyby of mars or venus. *Aerospace and Electronic Systems, IEEE Transactions on*, AES-2(4):613–623, July 1966.

[90] I Melgarejo, D Orozco, F Nunez, C M Rubio, and R Lang. The role of real time 3D TEE in defining the anatomy of atrial septal defects and modifying the therapeutic approach. *Eur Heart J Cardiovasc Imaging*, 13(3):270, 2012.

[91] C.T. Metz, N. Baka, H.A. Kirisli, M. Schaap, S. Klein, L. Neefjes, N.R.A. Mollet, B.P.F. Lelieveldt, M. de Bruijne, W.J. Niessen, and T. van Walsum. Regression-based cardiac motion prediction from single-phase cta. *IEEE Transactions on Medical Imaging*, 31(6):1311–1325, 2012.

[92] A. D. Milne, D. G. Chess, J. A. Johnson, and G. J. King. Accuracy of an electromagnetic tracking device: a study of the optimal range and metal interference. *Journal of biomechanics*, 30(0021-9290 (Linking)):857–9, 1997.

[93] S.C. Mitchell, B.P.F. Lelieveldt, R.J. van der Geest, H.G. Bosch, J.H.C. Reiver, and M. Sonka. Multistage hybrid active appearance model matching: segmentation of left and right ventricles in cardiac mr images. 20(5):415–423, 2001.

[94] M J Monaghan. *Practical echocardiography and doppler*. John Wiley & Sons Ltd., West Sussex, 1990.

[95] T.K. Moon. The expectation-maximization algorithm. *Signal Processing Magazine, IEEE*, 13(6):47–60, Nov 1996.

[96] H.W. Mulder, M. van Stralen, H.B. van der Zwaan, K.Y.E. Leung, J.G. Bosch, and J.P.W. Pluim. Multi-frame registration of realtime 3d echocardiography time series. *Journal of Medical Imaging*, 2014.

[97] Denisa Muraru, Luigi P. Badano, Gianluca Piccoli, Pasquale Gianfagna, Lorenzo Del Mestre, Davide Ermacora, and Alessandro Proclemer. Validation of a novel automated border-detection algorithm for rapid and accurate quantitation of left ventricular volumes based on three-dimensional echocardiography. 11(4):359–368, 2010.

[98] K. Nathanail, M. van Stralen, C. Prins, F. van den Adel, P.J. French, N. de Jong, A.F.W. Van der Steen, and J.G. Bosch. Rapid 3d transesophageal echocardiography using a fast-rotating multiplane transducer. In *Ultrasonics Symposium IEEE*, 2008.

[99] Ka Wei Ng, Jin Quan Goh, Soo Leong Foo, Poh Hua Ting, Teck Kheng Lee, Kesavan Esuvaranathan, Qing Hui Wu, and Edmund Chiong. Needle deflection studies for optimal insertion modeling. *International Journal of Bioscience, Biochemistry and Bioinformatics*, 3(6):570–574, November 2013.

[100] Maartje M. Nillesen, Richard G.P. Lopata, H.J. Huisman, Johan M. Thijssen, Livia Kapusta, and Chris L. de Korte. Correlation based 3-d segmentation of the left ventricle in pediatric echocardiographic images using radio-frequency data. *Ultrasound in Medicine & Biology*, 37:1409–1420, 2011.

[101] M.M. Nillesen, R.G.P. Lopata, I.H. Gerrits, L. Kapusta, J.M. Thijssen, and C.L. de Korte. Modeling envelope statistics of blood and myocardium for segmentation of echocardiographic images. *Ultrasound in Medicine & Biology*, 34(4):674–80, 2008.

[102] J Alison Noble and Djamal Boukerroui. Ultrasound image segmentation: a survey. *IEEE Transactions on Medical Imaging*, 25(8):987–1010, August 2006.

[103] Travis E. Oliphant. *Guide to NumPy*. Provo, UT, March 2006.

[104] F. Orderud. *Real-time segmentation of 3D echocardiograms using a state estimation approach with deformable models*. PhD thesis, NTNU, 2010.

[105] M V Orlov, P Hoffmeister, G M Chaudhry, I Almasry, G H Gijsbers, T Swack, and C I Haffajee. Three-dimensional rotational angiography of the left atrium and esophagus–A virtual computed tomography scan in the electrophysiology lab? *Heart Rhythm*, 4(1):37–43, 2007.

[106] Stanley Osher and James A Sethian. Fronts propagating with curvature-dependent speed: Algorithms based on hamilton-jacobi formulations. *Journal of Computational Physics*, 79(1):12 – 49, 1988.

[107] C Pappone, G Oreto, S Rosanio, G Vicedomini, F Gugliotta, A Salvati, C Dicandia, M P Calabro, P Mazzone, E Ficarra, C Di Gioia, S Gulletta, S Nardi, V Santinelli, S Benussi, and O Alfieri. Atrial electroanatomic remodeling after circumferential radiofrequency pulmonary vein ablation: efficacy of an anatomic approach in a large cohort of patients with atrial fibrillation. *Circulation*, 104:2539–2544, 2001.

[108] C Pappone, S Rosanio, G Oreto, M Tocchi, F Gugliotta, G Vicedomini, A Salvati, C Dicandia, P Mazzone, V Santinelli, S Gulletta, and S Chierchia. Circumferential radiofrequency ablation of pulmonary vein ostia: A new anatomic approach for curing atrial fibrillation. *Circulation*, 21:2619–28, 2000.

[109] K Perisinakis, J Damilakis, N Theocharopoulos, E Manios, P Vardas, and N Gourtsoyiannis. Accurate assessment of patient effective radiation dose and associated detriment risk from radiofrequency catheter ablation procedures. *Circulation*, 104(1):58–62, 2001.

[110] Caroline Petitjean and Jean-Nicolas Dacher. A review of segmentation methods in short axis cardiac MR images. 15(2):169–184, dec 2010.

[111] Dzung L. Pham, Chenyang Xu, and Jerry L. Prince. Current methods in medical image segmentation. 2(1):315–337, 2000. PMID: 11701515.

[112] Tuan Q. Pham, Lucas J. van Vliet, and Klamer Schutte. Robust fusion of irregularly sampled data using adaptive normalized convolution. *EURASIP Journal on Applied Signal Processing*, 2006:1–12, 2006.

[113] K.P. Philip, E.L. Dove, D.D. McPherson, N. L. Gotteiner, W. Stanford, and K.B. Chandran. The fuzzy hough transform-feature extraction in medical images. 13(2):235–240, 1994.

[114] AM Pouch, H Wang, M Takabe, BM Jackson, JH Gorman III, RC Gorman, PA Yushkevich, and CM Sehgal. Fully automatic segmentation of the mitral leaflets in 3d transesophageal echocardiographic images using multi-atlas joint label fusion and deformable medial modeling. 18(1):118–129, 2013.

[115] Sunil M Prasad, Hersh S Maniar, Cindy J Camillo, Richard B Schuessler, John P Boineau, Thoralf M Sundt III, James L Cox, and Ralph J Damiano Jr. The cox maze {III} procedure for atrial fibrillation: long-term efficacy in patients undergoing lone versus concomitant procedures. *The Journal of Thoracic and Cardiovascular Surgery*, 126(6):1822 – 1827, 2003.

[116] Kashif Rajpoot, Vicente Grau, J. Alison Noble, Cezary Szmigielski, and Harald Becher. Multiview fusion 3-d echocardiography: Improving the information and quality of real-time 3-d echocardiography. *Ultrasound in Medicine & Biology*, 37(7):1056 – 1072, 2011.

[117] O. Raungratanaamporn, K. Bhurippanyo, C. Chotinaiwattarakul, S. Suksap, A. Chirapastan, N. Ninmaneechot, and M. Numee. Lasso catheter guided ablation for paroxysmal atrial fibrillation: the first experience in thailand. *J. Med. Assoc. Thai.*, 86(0125-2208 (Linking)):96–104, 2003.

[118] James G. Ravenel and H. Page McAdams. Pulmonary venous infarction after radiofrequency ablation for atrial fibrillation. *American Journal of Roentgenology*, 178(3):664–666, March 2002.

[119] B. Ren, H.W. Mulder, A. Haak, J. McGhie, T. Szili-Torok, K. Nieman, M. van Stralen, J.P.W. Pluim, M.L. Geleijnse, and J.G. Bosch. *Advanced Three-Dimensional Echocardiography*, chapter 4.2, pages 147–161. 2014.

[120] B. Ren, H.W. Mulder, A. Haak, M. van Stralen, T. Szili-Torok, J.P.W. Pluim, M.L. Geleijnse, and J.G. Bosch. A transoesophageal echocardiographic image acquisition protocol for wide-view fusion of three-dimensional datasets to support atrial fibrillation catheter ablation. *Journal of Interventional Cardiac Electrophysiology*, 37(1):21–26, June 2013.

[121] Jian-Fang Ren, David Schwartzman, David J Callans, Susan E Brode, Charles D Gottlieb, and Francis E Marchlinski. Intracardiac echocardiography (9 mhz) in humans: methods, imaging views and clinical utility. *Ultrasound in Medicine & Biology*, 25(7):1077 – 1086, 1999.

[122] M. W. Rich. Epidemiology of atrial fibrillation. *J Interv Card Electrophysiol*, 25:3–8, 2009.

[123] L S Rosenthal, T J Beck, J Williams, M Mahesh, M G Herman, J L Dinerman, H Calkins, and J H Lawrence. Acute radiation dermatitis following radiofrequency catheter ablation of atrioventricular nodal reentrant tachycardia. *Pacing Clin Electrophysiol*, 20(7):1834–1839, 1997.

[124] Yongyuth Sahasakul, William D. Edwards, James M. Naessens, and A.Jamil Tajik. Age-related changes in aortic and mitral valve thickness: Implications for two-dimensional echocardiography based on an autopsy study of 200 normal human hearts. 62(7):424 – 430, 1988.

[125] Walid Saliba, Vivek Y. Reddy, Oussama Wazni, Jennifer E. Cummings, J. David Burkhardt, Michel Haissaguerre, Josef Kautzner, Petr Peichl, Petr Neuzil, Volker Schibgilla, Georg Noelker, Johannes Brachmann, Luigi Di Biase, Conor Barrett, Pierre Jais, and Andrea Natale. Atrial fibrillation ablation using a robotic catheter remote control systeminitial human experience and long-term follow-up results. *Journal of the American College of Cardiology*, 51(25):2407–2411, 2008.

[126] Alessandro Salustri, Anton E. Becker, Lex van Herwerden, Wim B. Vletter, Folkert J. Ten Cate, and Jos R.T.C. Roelandt. Three-dimensional echocardiography of normal and pathologic mitral valve: A comparison with two-dimensional transesophageal echocardiography. 27(6):1502 – 1510, 1996.

[127] Y. Sato, C. F Westin, A. Bhalerao, S. Nakajima, N. Shiraga, S. Tamura, and R. Kikinis. Tissue classification based on 3d local intensity structures for volume rendering. 6(2):160–180, 2000.

[128] Yoshinobu Sato, Shin Nakajima, Nobuyuki Shiraga, Hideki Atsumi, Shigeyuki Yoshida, Thomas Koller, Guido Gerig, and Ron Kikinis. Three-dimensional multi-scale line filter for segmentation and visualization of curvilinear structures in medical images. 2(2):143 – 168, 1998.

[129] Robert J. Schneider, D.P. Perrin, Nikolay V. Vasilyev, G.R. Marx, P.J. del Nido, and R.D. Howe. Mitral annulus segmentation from 3d ultrasound using graph cuts. 29(9):1676–1687, 2010.

[130] J S Shanewise, A T Cheung, S Aronson, W J Stewart, R L Weiss, J B Mark, R M Savage, P Sears-Rogan, J P Mathew, M A Quinones, M K Cahalan, and J S Savino. ASE/SCA guidelines for performing a comprehensive intraoperative multiplane transesophageal echocardiography examination: recommendations of the American Society of Echocardiography Council for Intraoperative Echocardiography and the Society of Cardiovascular Anesthesiologists Task Force for Certification in Perioperative Transesophageal Echocardiography. *J Am Soc Echocardiogr*, 12(10):884–900, 1999.

[131] Julie B. Shea and Samuel F. Sears. A patient's guide to living with atrial fibrillation. *Circulation*, 117(20):340–343, 2008.

[132] Yuichi J. Shimada and Takahiro Shiota. A meta-analysis and investigation for the source of bias of left ventricular volumes and function by three-dimensional echocardiography in comparison with magnetic resonance imaging. 107(1):126 – 138, 2011.

[133] Shlomo Shpun, Lior Gepstein, Gal Hayam, and Shlomo A. Ben-Haim. Guidance of radiofrequency endocardial ablation with real-time three-dimensional magnetic navigation system. *Circulation*, 96(6):2016–2021, 1997.

[134] G.L. Smith, S.F. Schmidt, and L.A. McGee. Application of statistical filter theory to the optimal estimation of position and velocity on board a circumlunar vehicle. Technical report, National Aeronautics and Space Administration, 1962.

[135] Osama I.I. Soliman, Boudewijn J. Krenning, Marcel L. Geleijnse, Attila Nemes, Robert-Jan van Geuns, Timo Baks, Ashraf M. Anwar, Tjebbe W. Galema, Wim B. Vletter, and Folkert J. Ten Cate. A comparison between qlab and tomtec full volume reconstruction for real time three-dimensional echocardiographic quantification of left ventricular volumes. *Echocardiography*, 24(9):967–974, 2007.

[136] Carolin Sonne, Lissa Sugeng, Nozomi Watanabe, Lynn Weinert, Ken Saito, Miwako Tsukiji, Kiyoshi Yoshida, Masaaki Takeuchi, Victor Mor-Avi, and Roberto M. Lang. Age and body surface area dependency of mitral valve and papillary apparatus parameters: assessment by real-time three-dimensional echocardiography. 10(2):287–294, 2009.

[137] Tamas Szili-Torok and Johan G. Bosch. Transnasal transoesophageal ultrasound: the end of the intracardiac echocardiography age? *Europace*, 13(1):7–8, 2011.

[138] Zhong Tao, H.D. Tagare, and J.D. Beaty. Evaluation of four probability distribution models for speckle in clinical cardiac ultrasound images. *IEEE Transactions on Medical Imaging*, 25(11):1483–1491, Nov 2006.

[139] Mehmet Üzümcü, Rob J van der Geest, Cory Swingen, Johan HC Reiber, and Boudewijn PF Lelieveldt. Time continuous tracking and segmentation of cardiovascular magnetic resonance images using multidimensional dynamic programming. *Investigative radiology*, 41(1):52–62, 2006.

[140] A E van den Bosch, D J Ten Harkel, J S McGhie, J W Roos-Hesselink, M L Simoons, A J Bogers, and F J Meijboom. Characterization of atrial septal defect assessed by real-time 3-dimensional echocardiography. *J Am Soc Echocardiogr*, 19(6):815–821, 2006.

[141] Annemien E. van den Bosch, Danielle Robbers-Visser, Boudewijn J. Krenning, Marco M. Voormolen, Jackie S. McGhie, Wim A. Helbing, Jolien W. Roos-Hesselink, Maarten L. Simoons, and Folkert J. Meijboom. Real-time transthoracic three-dimensional echocardiographic assessment of left ventricular volume and ejection fraction in congenital heart disease. 19(1):1 – 6, 2006.

[142] Rob J van der Geest, Vincent GM Buller, Eric Jansen, Hildo J Lamb, Leo HB Baur, Ernst E van der Wall, Albert de Roos, and Johan HC Reiber. Comparison between manual and semiautomated analysis of left ventricular volume parameters from short-axis mr images. 21(5):756–765, 1997.

[143] B. van Ginneken, A.F. Frangi, J.J. Staal, B.M. ter Haar Romeny, and M.A. Viergever. Active shape model segmentation with optimal features. *IEEE Transactions on Medical Imaging*, 21(8):924–933, aug. 2002.

[144] M. Van Stralen, K.Y.E. Leung, M.M. Voormolen, N. de Jong, A.F.W. van der Steen, J.H.C. Reiber, and J.G. Bosch. Time continuous detection of the left ventricular long axis and the mitral valve plane in 3-d echocardiography. 34(2):196 – 207, 2008.

[145] A Vegas, M Meineri, and A Jerath. *Real-Time Three-Dimensional Transesophageal Echocardiography: A Step-by-Step Guide*. Springer, New York, 2012.

[146] G. Vegas-Sanchez-Ferrero, S. Aja-Fernandez, M. Martin-Fernandez, A.F. Frangi, and C. Palencia. Probabilistic-driven oriented speckle reducing anisotropic diffusion with application to cardiac ultrasonic images. volume 6361 of *Lecture Notes in Computer Science*, pages 518–525. Springer Berlin Heidelberg, 2010.

[147] G. Vegas-Sanchez-Ferrero, S. Aja-Fernandez, C. Palencia, and M. Martin-Fernandez. A generalized gamma mixture model for ultrasonic tissue characterization. 2012(Article ID 481923):1–25, 2012.

[148] G. Vegas-Sánchez-Ferrero, M. Martín-Martinez, and J.Miguel Sanches. A gamma mixture model for ivus imaging. In Luca Saba, João Miguel Sanches, Luís Mendes Pedro, and Jasjit S. Suri, editors, *Multi-Modality Atherosclerosis Imaging and Diagnosis*, pages 155–171. Springer New York, 2014.

[149] Gonzalo Vegas-Sánchez-Ferrero, Marcos Martin-Fernandez, and Joao Miguel-Sanches. *Multi-Modality Atherosclerosis Imaging and Diagnosis*, chapter A Gamma Mixture Model for IVUS Imaging, pages 155–171. Springer Verlag.

[150] Gonzalo Vegas-Sánchez-Ferrero, Jose Seabra, Oriol Rodriguez-Leor, Angel Serrano-Vida, Santiago Aja-Fernández, Cesar Palencia, , Marcos Martin-Fernandez, and Joao Sanches. Gamma mixture classifier for plaque detection in intravascular ultrasonic images. *IEEE Transactions on Ultrasonics Ferroelectrics and Frequency Control*, page In press, 2014.

[151] Gonzalo Vegas-Sanchez-Ferrero, Jose Seabra, Oriol Rodriguez-Leor, Angel Serrano-Vida, Santiago Aja-Fernandez, Cesar Palencia, Marcos Martin-Fernandez, and Joao Sanches. Gamma mixture classifier for plaque detection in intravascular ultrasonic images. 61(1):44–61, 2014.

[152] Gonzalo Vegas-Sánchez-Ferrero, Antonio Tristán-Vega, Santiago Aja-Fernández, Marcos Martín-Fernández, Cesar Palencia, and Rachid Deriche. Anisotropic LMMSE denoising of MRI based on statistical tissue models. In *International Symposium on Biomedical Imaging*, pages 1519–1522, 2012.

[153] M.M. Voormolen, B.J. Krenning, C.T. Lancee, F.J. ten Cate, J.R.T.C. Roelandt, A.F.W. van der Steen, and N. de Jong. Harmonic 3-d echocardiography with a fast-rotating ultrasound transducer. *IEEE Trans Ultrason Ferroelectr Freq Control*, 539(10):1739 – 1748, 2006.

[154] R.F. Wagner, S.W. Smith, J.M. Sandrik, and H. Lopez. Statistics of speckle in ultrasound b-scans. *IEEE Transactions on Sonics and Ultrasonics*, 30(3):156 –163, may 1983.

[155] Johan E.P. Waktare. Atrial fibrillation. *Circulation*, 106(1):14–16, 2002.

[156] E.A. Wan and R. Van Der Merwe. The unscented kalman filter for nonlinear estimation. In *Adaptive Systems for Signal Processing, Communications, and Control Symposium 2000. AS-SPCC. The IEEE 2000*, pages 153–158, 2000.

[157] Nozomi Watanabe, Yasuo Ogasawara, Yasuko Yamaura, Takahiro Kawamoto, Eiji Toyota, Takashi Akasaka, and Kiyoshi Yoshida. Quantitation of mitral valve tenting in ischemic mitral regurgitation by transthoracic real-time three-dimensional echocardiography. 45(5):763–769, mar 2005.

[158] T.S. Yoo, M. J. Ackerman, W. E. Lorensen, W. Schroeder, V. Chalana, S. Aylward, D. Metaxes, and R. Whitaker. Engineering and algorithm design for an image processing api: A technical report on itk - the insight toolkit. In *Proc. of Medicine Meets Virtual Reality, J. Westwood, ed., IOS Press Amsterdam pp 586-592*, 2002.

[159] ZobairM. Younossi, J.Carlos Teran, TheodoreG. Ganiats, and WilliamD. Carey. Ultrasound-guided liver biopsy for parenchymal liver disease (an economic analysis). *Digestive Diseases and Sciences*, 43(1):46–50, 1998.

[160] Peter Zimmermann, Clemens Greim, Herbert Trautner, Ulrich Sagmeister, Katharina Kraemer, and Norbert Roewer. Echocardiographic monitoring during induction of general anesthesia with a miniaturized esophageal probe. *Anest Analg*, 96:21–27, 2003.

Summary

Atrial fibrillation is the most common heart rhythm disorder in the western world affecting millions of people. The heart is a bio-mechanical pump which is activated by electrical signals propagating through the heart tissue in a specific way. If this electrical activation is disturbed the heart cannot contract efficiently leading to a range of symptoms including life threatening ones. Atrial fibrillation by itself is not directly life threatening but mortality rises in patient with atrial fibrillation due to the increased risk of stroke and finally from heart failure, after remodeling of the heart due to the reduced filling of the ventricles. Furthermore, there is a substantial decrease in quality of life for these patients.

Electrophysiology (EP) deals with the treatment of abnormalities with the electro-mechanical functioning of the heart. Atrial fibrillation can be treated pharmacologically with arrhythmia drugs and anticoagulants but in some patients this does not lead to successful outcomes. Isolating erroneous conduction sites in the heart is another way of curing atrial fibrillations. Open heart surgical procedures, where the atrium is compartmentalized through incisions, have good success rates but they are not applicable for a large portion of patients because of the involved risks.

Isolation can also be created in a minimally invasive fashion where catheters in the heart are used to diagnose conduction abnormalities and lesions are created with RF-ablation catheters to establish correct electrical conduction in the tissue. These type of procedures are done under X-ray fluoroscopy guidance and catheter tip locations are measured with special tracking equipment. Preoperative images, such as CT and MRI, can be used to establish a 3D anatomical context but the anatomical situation may have already been changed at the time of intervention.

Unfortunately, these minimally invasive interventions have a significantly lower success rate than the open heart surgery. There is also a large variance of the procedure outcome between patients, hospitals and even between clinicians.

One of the major causes of the poor performance of these minimally invasive procedures may be the insufficient visualization of the catheters during the intervention in real-time within the 3D anatomical context.

Transesophageal echocardiography (TEE) is an excellent modality to visualize catheters and the heart's anatomy in 3D during the interventions. However, the conventional 3D TEE probes are rather large and cannot be tolerated by an awake patient over an extended period of time. Many of the ablation procedures are done only in non-anesthetized patients. Miniaturized TEE probes (μTEE) which are suitable for transnasal insertion may be an alternative since patient discomfort is significantly lower. However, such small probes currently produce only 2D images. The image plane can be rotated within a conical volume, and might be used to do 3D image reconstruction.

This thesis deals with the use of 3D TEE (by conventional 3D TEE and by rotated 2D μTEE) to support EP interventions, such as minimally invasive catheter ablations.

The first aspect is 3D/4D image reconstruction from sparse and irregularly sampled 2D images acquired with the TEE probe. In **chapter 2** we tested several image interpolation methods and showed that normalized convolution yields the best reconstruction results. We optimized the reconstructions and developed a model to predict optimal reconstruction parameters. We also showed that already a relative low number of 600 2D images (which can be acquired within a few seconds) yields acceptable 3D images over the full heart cycle.

In **chapter 3** we show that a patient specific surface model of the heart anatomy can be created by segmenting 3D TEE images. The field of view of a 3D TEE probe is limited and it is not possible to image the entire heart at once. We demonstrated that an active shape model can overcome this shortcoming and has good extrapolation properties into regions which are not covered by the ultrasound image. We also show in **chapter 4** that automatic model initialization is possible by detecting anatomical landmarks in the TEE image.

The left atrium is of special interest for catheter ablations but suffers the most from the limited TEE field of view. We therefore established an imaging protocol to acquire several 3D TEE views to compose a panoramic wide-view of the left atrium. In **chapter 5** we present details to the acquisition protocol and generated wide-view images. In **chapter 6** we evaluate the visibility and the accuracy of indicated left atrial landmarks by comparing them to CT images of the same patient. We could successfully show that landmarks are accurately detected with an error comparable to the intra-observer variability.

Wide-view TEE images were segmented with an active shape model and we could show that these segmentations are more accurate than the ones de¬rived

from single-view TEE (see **chapter 7**). Fusion artifacts did not seem to deteriorate image segmentation.

The detection and tracking of the catheters in live 2D TEE images is another aspect of improving catheter ablations. In **chapter 8** we show that catheter shape and position can accurately be estimated with tracked 2D ultrasound and a catheter model. We are using a so called Kalman filter which is fast and robust to noisy data. Furthermore, our approach allows to integrate several sensors to localize the catheter more accurately. This is especially promising since during catheter ablations several imaging and tracking modalities are available which could be used.

With this thesis we demonstrated that catheter ablation procedures may be improved by using 3D TEE imaging and a miniaturized TEE probe. We successfully showed that 3D image reconstruction, wide-view image recording and fusion, image segmentation and catheter tracking is possible. This could greatly improve the visualization and outcome of these procedures.

Samenvatting

Atriumfibrilleren (AF) of boezemfibrilleren is de meest voorkomende hartritmestoornis in de westerse wereld en treft miljoenen mensen. Het hart is een biomechanische pomp die wordt geactiveerd door electrische signalen die zich in een bepaald patroon over het hartspierweefsel verspreiden. Als dat patroon is verstoord kan het hart niet efficiënt samentrekken. Dit leidt tot een scala van symptomen, waarvan sommige levensbedreigend zijn. AF zelf is niet direct levensbedreigend, maar in patiënten met AF stijgt de mortaliteit door een verhoogd risico op een herseninfarct en uiteindelijk door hartfalen, na remodellering van het hart vanwege de verminderde vulling van de hartkamers. Verder wordt de kwaliteit van leven van deze patiënten ernstig beperkt.

De electrofysiologie (EP) richt zich op de behandeling van afwijkingen in het electromechanisch functioneren van het hart. AF wordt doorgaans medicinaal behandeld (met antiaritmica en anticoagulantia) maar dit werkt onvoldoende in sommige patiënten. AF kan ook behandeld worden door stukjes hartspier met afwijkende geleiding te isoleren. Dit kan met een open-hartoperatie, waarbij de linkerboezem in compartimenten wordt verdeeld door de wand door te snijden en weer te hechten. Deze ingrepen hebben een hoge successcore maar zijn vanwege de risico's ongeschikt voor een groot deel van de patiëntenpopulatie.

De gewenste isolatie kan ook worden bereikt met een minimaal-invasieve ingreep, waarbij catheters in het hart worden gebracht om de geleidingsafwijking in kaart te brengen en vervolgens te corrigeren door met RF-ablatiecatheters gericht laesies in de wand te branden. Deze procedures worden normaal uitgevoerd onder fluoroscopie en de catheterposities worden gevolgd met speciale tracking- apparatuur. Preoperatieve beelden zoals CT en MR kunnen worden gebruikt om een 3D anatomische context te genereren, maar de anatomische situatie kan al aanzienlijk veranderd zijn op het moment van de interventie.

Helaas hebben deze minimaal-invasieve interventies een aanzienlijk lagere

successcore dan de open-hartchirurgie. Het succes varieert ook aanzienlijk tussen patienten, ziekenhuizen en zelfs tussen verschillende artsen. Een belangrijke mogelijke oorzaak van de matige scores vormt de beperkte realtime visualisatie van de catheters binnen de 3D anatomische context.

Transoesofagale echocardiografie (TEE) is een uitstekende modaliteit voor de visualisatie van catheters in de 3D anatomie van het hart tijdens een interventie. Helaas zijn de conventionele 3D TEE probes nogal omvangrijk, en een wakkere patient kan deze niet gedurende lange ingrepen verdragen. Veel ablatieingrepen worden namelijk uitsluitend zonder anesthesie uitgevoerd. Sterk verkleinde TEE-probes (zogenaamde μTEE s, die zelfs via de neus kunnen worden ingebracht) kunnen een alternatief vormen, omdat het ongemak voor de patient veel kleiner is. Tot nu toe produceren degelijke probes slechts 2D beelden, maar het beeldvlak kan in een kegelvormig volume worden rondgedraaid, en dit kan gebruikt worden om driedimensionale beelden te reconstrueren.

Dit proefschrift behandelt het gebruik van 3D TEE (zowel van conventionele 3D TEE probes als van geroteerde 2D μTEE) ter ondersteuning van EP interventies, zoals minimaal-invasieve catheterablaties.

Het eerste aspect hiervan is de reconstructie van tijdseries van 3D beelden, uit de 2D TEE beelden die het hart spaarzaam en onregelmatig bemonsteren. In **Hoofdstuk 2** hebben wij verschillende beeldinterpolatiemethodes getest en aangetoond dat genormaliseerde convolutie de beste resultaten oplevert. We hebben de reconstructies geoptimaliseerd en een methode ontwikkeld om de optimale reconstructieparameters te voorspellen. We hebben ook aangetoond dat uit een relatief klein aantal 2D beelden (600 beelden, binnen een paar seconden opgenomen) een acceptabele 3D reconstructie van het hart kan worden gemaakt over de gehele hartcyclus.

In **Hoofdstuk 3** laten we zien dat een patient-specifiek oppervlaktemodel van de hartkamers kan worden verkregen door de 3D TEE beelden te segmenteren. Het blikveld van een 3D TEE probe is beperkt en het is niet mogelijk het gehele hart in één opname te af te beelden.We laten zien dat een active shape model met deze beperking overweg kan en een goede extrapolatie oplevert in gebieden die buiten het echobeeld vallen. Ook laten we in **Hoofdstuk 4** zien dat het active shape model automatisch geïnitialiseerd kan worden door anatomische herkenningspunten in het 3D TEE beeld te detecteren.

Voor catheterablaties is vooral de linkerboezem zeer belangrijk, maar juist deze lijdt onder het beperkte blikveld van TEE probes. Daarom hebben we een opnameprotocol vastgelegd met verschillende 3D TEE opnames om een panoramische breedbeeld-opname van de linkerboezem samen te kunnen stellen. In **Hoofdstuk 5** behandelen we dit protocol en de gefuseerde beelden in de-

tail. **Hoofdstuk 6** evalueert de zichtbaarheid van diverse anatomische herkenningspunten en de nauwkeurigheid waarmee deze kunnen worden aangegeven in de fusiebeelden, door vergelijking met CT-beelden van dezelfde patiënten. We konden aantonen dat deze herkenningspunten nauwkeurig konden worden aangegeven, met een fout die vergelijkbaar is met de intraobserver-variabiliteit.

De breedbeeld-TEE beelden werden gesegmenteerd met een active shape model en we konden aantonen dat deze segmentaties preciezer waren dan die op afzonderlijke 3D TEE beelden (**Hoofdstuk 7**). Fusie-artefacten verslechterden de segmentatie niet noemenswaardig.

Catheterablaties kunnen ook worden verbeterd door het detecteren en tracken van de catheters in live 2D TEE beelden. In **Hoofdstuk 8** laten we zien dat vorm en positie van een catheter nauwkeurig geschat kunnen worden met getrackte 2D TEE en een cathetermodel. Het gebruikte zogenaamde Kalman filter is snel en robuust wanneer gegevens door ruis zijn verstoord. Bovendien kunnen in onze benadering de gegevens van meerdere positiesensors worden meegenomen om de catheter nauwkeuriger te localiseren. Dit is extra aantrekkelijk omdat bij catheterablaties verschillende soorten tracking en verschillende beeldmodaliteiten gebruikt worden, waarvan de informatie gecombineerd kan worden.

In dit proefschrift hebben we laten zien dat catheterablatieprocedures verbeterd kunnen worden door het gebruik van 3D TEE en een geminiaturiseerde TEE-probe. We hebben met succes aangetoond dat 3D beeldreconstructie, generatie van breedbeeldopnames en cathetertracking mogelijk zijn. Dit zou de visualisatie en resultaten van catheterablaties aanzienlijk kunnen verbeteren.

Curriculum Vitae

Alexander Haak was born December 1978 in Halle, East Germany. In 1995, after secondary school, he began his vocational training to become an electrician, which he completed successfully 1999. He applied this training while working for a year at the power utility company of his home town. In the year 2000, Alexander received a scholarship to study English abroad in Australia. In 2002, Alexander began his collegiate studies in Applied Physics and Information Science at Merseburg University. He finished his undergraduate thesis in 2006 on Cavitation Detection of Ultrasound Contrast Agents, which he conducted in the Bioacoustic Research Laboratory at the University of Illinois at Urbana-Champaign (UIUC). He received his Master's degree in Electrical Engineering and Computer Science from UIUC in 2010 focusing on Quantitative Ultrasound. That same year, Alexander joined the department of Biomedical Engineering at Easmus University Medical Center working on his PhD degree. There he focuses on supporting Electrophysiology Interventions using advanced 3D Transesophageal Ultrasound under the supervision of Johan G. Bosch and Antonius F.W. van der Steen.

Publications

Journal papers

- M.D. Santin, D.A. King, J. Foiret, **A. Haak**, W.D. O'Brien Jr., S.L. Bridal, Encapsulated contrast microbubble radial oscillation associated with postexcitation pressure peaks, *The Journal of the Acoustical Society of America* **127**(2) (2010), pp. 1156-1164.

- D.A. King, M.J. Malloy, A.C. Roberts, **A. Haak**, C.C. Yoder, W.D. O'Brien Jr., Determination of postexcitation thresholds for single ultrasound contrast agent microbubbles using double passive cavitation detection, *The Journal of the Acoustical Society of America* **127**(6) (2010), pp. 3449-3455.

- J.J. Anderson, M.-T. Herd, M.R. King, **A. Haak**, Z.T. Hafez, J. Song, M.L. Oelze, E.L. Madsen, J.A. Zagzebski, W.D. O'Brien Jr., T.J. Hall, Interlaboratory comparison of backscatter coefficient estimates for tissue-mimicking phantoms, *Ultrasonic imaging* **32**(1) (2010), pp. 48-64.

- L.A. Wirtzfeld, G. Ghoshal, Z.T. Hafez, K. Nam, Y. Labyed, J.J. Anderson, M.-T. Herd, **A. Haak**, Z. He, R.J. Miller, S. Sarwate, D.G. Simpson, J.A. Zagzebski, T.A. Bigelow, M.L. Oelze, T.J. Hall, W.D. O'Brien Jr., Cross-imaging platform comparison of ultrasonic backscatter coefficient measurements of live rat tumors, *Journal of Ultrasound in Medicine* **29**(7) (2010), pp. 1117-1123.

- M.R. King, J.J. Anderson, M.-T. Herd, D. Ma, **A. Haak**, L.A. Wirtzfeld, E.L. Madsen, J.A. Zagzebski, M.L. Oelze, T.J. Hall, W.D. O'Brien Jr., Ultrasonic backscatter coefficients for weakly scattering, agar spheres in agar phantoms, *The Journal of the Acoustical Society of America* **128**(2) (2010), pp. 903-908.

- B.W. Smith, D.G. Simpson, S. Sarwate, R.J. Miller, J.P. Blue, **A. Haak**, W.D. O'Brien Jr., J.W. Erdman, Contrast ultrasound imaging of the aorta alters vascular morphology and circulating von Willebrand Factor in hypercholesterolemic rabbits, *Journal of Ultrasound in Medicine* **31**(5) (2012), PP. 711-712.

- L.A. Wirtzfeld, K. Nam, Y. Labyed, G. Ghoshal, **A. Haak**, E. Sen-Gupta, H. Zhi, N.R. Hirtz, R.J. Miller, S. Sarwate, D.G. Simpson, J.A. Zagzebski, T.A. Bigelow, M.L. Oelze, T.J. Hall, W.D. O'Brien Jr., Techniques and evaluation from a cross-platform imaging comparison of quantitative ultrasound parameters in an in vivo rodent fibroadenoma model, *IEEE Transaction on Ultrasonics, Ferroelectrics, and Frequency Control* **60**(7) (2013), pp. 1386-1400.

- B. Ren, H. W. Mulder, **A. Haak**, M. van Stralen, T. Szili-Torok, J. P. W. Pluim, M. L. Geleijnse, J. G. Bosch, A transoesophageal echocardiographic image acquisition protocol for wide-view fusion of three-dimensional datasets to support atrial fibrillation catheter ablation. *Journal of Interventional Cardiac Electrophysiology* **37**(1) (2013), pp. 21–26.

- A. H. Curiale, **A. Haak**, G. Vegas-Sánchez-Ferrero, B. Ren, S. Aja-Fernández, and J. G. Bosch, Fully automatic detection of salient features in 3D transesophageal images, *Ultrasound in Medicine and Biology* **40**(12) (2014), pp. 1-17.

- B. Ren, H.W. Mulder, **A. Haak**, J. McGhie, T. Szili-Torok, K. Nieman, M. van Stralen, J.P.W. Pluim, M.L. Geleijnse, and J.G. Bosch, *Advanced Three-Dimensional Echocardiography*, chapter 4.2, pages 147-161, (2014).

- **A. Haak**, G. Vegas-Sánchez-Ferrero, H.W. Mulder, B. Ren, H.A. Kirişli, C. Metz, G. van Burken, M. van Stralen, J.P.W. Pluim, A.F.W. van der Steen , T. van Walsum and J.G. Bosch, Segmentation of multiple heart cavities in 3D transesophageal ultrasound images, *IEEE Transaction on Ultrasonics, Ferroelectrics, and Frequency Control* accepted (2015).

- **A. Haak**, B. Ren, H.W. Mulder, G. Vegas-Sánchez-Ferrero, G. van Burken, A.F.W. van der Steen, M. van Stralen, J.P.W. Pluim, T. van Walsum and J. G. Bosch, Improved segmentation of multiple cavities of the heart in wide-view 3D transesophageal echocardiograms, *Ultrasound in Medicine and Biology* **41** (2015), pp. 1991-2000.

- **A. Haak**, G. Vegas-Sánchez-Ferrero, and J. G. Bosch, Catheter Catheter shape estimation using tracked ultrasound imaging and Kalman filters, (submitted).

Proceedings

- **A. Haak**, B. Castañeda, R. Lavarello, W.D. O'Brien Jr., Semiautomatic detection of microbubble ultrasound contrast agent destruction applied to Definity using support vector machines, *in Proceedings of the IEEE Ultrasonics Symposium*, pp. 660–663, 2007.

- **A. Haak**, Z. Hafez, J. Anderson, M. Herd, K. Nam, E. Madesn, T. Bigelow, T. Hall, W. O'Brien, Jr., "Algorithm for estimating the attenuation slope from backscattered ultrasonic signals," in Proceedings of the IEEE Ultrasonics Symposium, pp. 1946 – 1949, 2009.

- **A. Haak**, S. Klein, M. van Stralen, G. van Burken, J.P.W. Pluim, N. de Jong, A.F.W. van der Steen, and J.G. Bosch. Optimal kernel sizes for 4d image reconstruction using normalized convolution from sparse fast-rotating transesophageal 2d ultrasound images. In *Ultrasonics Symposium* (IUS), 2012 IEEE International, 2012.

- **A. Haak**, M. van Stralen, G. van Burken, S. Klein, J.P.W. Pluim, N. de Jong, A.F.W. van der Steen, and J.G. Bosch. Spatiotemporal interpolation by normalized convolution for 4d transesophageal echocardiography. In *Ultrasonics Symposium* (IUS), 2011 IEEE International, pp 152-155, 2011.

- **A. Haak**, G. Vegas-Sanchez-Ferrero, H.H. Mulder, H..H. Kirisli, N. Baka, C. Metz, S. Klein, B. Ren, G. van Burken, N. de Jong, A.F.W. van der Steen, J.P.W. Pluim, T. van Walsum, and J.G. Bosch. Simultaneous segmentation of multiple heart cavities in 3d transesophageal echocardiograms. In *Ultrasonics Symposium* (IUS), 2013 IEEE International, 2013.

- **A. Haak**, M. van Stralen, G. van Burken, S. Klein, J. P. W. Pluim, N. de Jong, A. F. W. van der Steen, and J. G. Bosch. Comparison of spatiotemporal interpolators for 4d image reconstruction from 2d transesophageal ultrasound. Proc. *SPIE* 8320, Medical Imaging 2012, pages 832007-832007-11, 2012.

- **A. Haak**, G. Vegas-Sánchez-Ferrero, H.W. Mulder, H. A. Kirisli, N. Baka, C. Metz, S. Klein, B. Ren, G. Burken, A. F.W. Steen, J.P.W. Pluim, T. van Walsum, and J. G. Bosch. Segmentation of 3d transesophageal echocardiograms by multi-cavity active shape model and gamma mixture model. In H. Liao, C.A. Linte, K. Masamune, T.M. Peters, and G. Zheng, editors, Augmented Reality Environments for Medical Imaging and Computer-Assisted Interventions, volume 8090 of Lecture Notes in Computer Science, pages 19-26. Springer Berlin Heidelberg, 2013.

- **A. Haak**, H. W. Mulder, B. Ren, G. Vegas-Sánchez-Ferrero, G. van Burken, A. F.W. van der Steen, M. van Stralen, J. P.W. Pluim, T. van Walsum, J. G. Bosch, Segmentation of multiple heart cavities in wide-view fused 3D transesophageal echocardiograms, In *Ultrasonics Symposium* (IUS), in press, 2014.

PhD Portfolio

International conference attendance	Year	**ECTs**
17th Ultrasound Contrast Imaging symposium, Rotterdam, Netherlands	2011	0.6
IEEE International Ultrasonics Symposium, Orlando, USA	2011	1.2
18th Ultrasound Contrast Imaging symposium, Rotterdam, Netherlands	2012	0.6
SPIE Medical Imaging, San Diego, USA	2012	1.2
IEEE International Ultrasonics Symposium, Dresden, Germany	2012	1.2
19th Ultrasound Contrast Imaging symposium, Rotterdam, Netherlands	2013	0.6
IEEE International Ultrasonics Symposium, Prague , Czech	2013	1.2
6th International Workshop on Medical Imaging and Augmented Reality, Nagoya, Japan	2013	0.6
16th International Conference on Medical Image Computing and Computer Assisted Intervention, Nagoya, Japan	2013	1.5
IEEE International Ultrasonics Symposium, Chicago, USA	2014	1.2

Conference presentations		
Oral presentation - IEEE International Ultrasonics Symposium	2011	1.0
Oral presentation - SPIE Medical Imaging	2012	1.0
Poster presentation - IEEE International Ultrasonics Symposium	2012	0.5

Oral presentation - IEEE International Ultrasonics Symposium	2013	1.0
Oral presentation - 6th International Workshop on Medical Imaging and Augmented Reality	2013	0.5
Oral presentation - IEEE International Ultrasonics Symposium	2014	1.0

Teaching

Supervising MS student	2010	4.0
Supervising MS student	2011	4.0
Supervising MS student	2012	4.0
Supervising BS student	2013	4.0

Courses

English biomedical writing and communication	2012	4.0
Introduction to MeVisLab	2010	1.5
Introduction to C++	2010	1.5
Knowledge driven Image Segmentation (ASCI)	2012	1.5
Advanced Pattern Recognition (ASCI)	2012	1.5
Animal imaging workshop (AMIE)	2011	0.9
Arrhythmia Research Methodology (COEUR)	2015	1.5
Cardiovascular Imaging and Diagnostics	2011	1.5

Total: 44.8

Acknowledgment

I began my PhD research about four years ago at Erasmus MC, University Medical Center Rotterdam. During that time I became a member of the close-knit BME family. Coming from my studies in the USA I was very happy to do research in a country next to Germany. In my naive ways, I was expecting that there would be descent bread, sausages and that I could finally escape this sweet Belgium beer. What shall I say, all of these rather silly expectations were disappointed, but the amazing work environment with great people and minds that I found at Erasmus made me forget about all that in an instant. I would like to thank all the members of this department for making my days more pleasant.

I want to acknowledge Ton, for giving me a PhD position in the most amazing environment, surrounded by knowledge, support and fantastic colleagues. The lab has done and is doing so much amazing research, that I am very happy and proud to be part of it.

Thank you to Nico and Gijs, who I was fortunate to have as supporters. Your knowledge and expertise made me feel honored to be a part of your team these past years. Nico, you even taught me some proper dialect from my home town, which is really amazing.

I want to thank Hans for being the best adviser you could wish for. Your patience and attention to detail is unmatched. Thank you so much for all the support, revisions, and hard work that you have put in especially in a time of need. It felt amazing to know that you always had my back. It was a pleasure to get to know you outside of work as well on our climbing trips, in particular, at Joshua Tree. I could have truly never asked for a better mentor.

Robert, Deine Hilfsbereitschaft ist nicht zu toppen und *"Nicht verzagen Robert fragen"* trifft es wohl am besten. Vielen Dank für alles und deine Witze werden unvergessen bleiben.

To my office mate, Gerard, thank you for fixing all my C++ build and

computer problems, which would have taken me days to solve. It was great to have you sitting across from me every day and a lot of fun growing a jungle with you.

Frits, Charles and Jan, it was always amazing to listen and learn from you guys. I felt like almost any idea or problem I discussed with you, you had already dealt with in one way or the other and were able to help me.

Telli, David, Krista thank you for taking me under your wings when I started here as a baby PhD. Your support and advise helped me tremendously to settle into the BME family.

To my friends, Verya, Guillaume and Zeynettin, my experience would not have been the same without you. You expanded my knowledge of music, Rotterdam, and fitness. Thank you for all the barbecues, concerts, and especially climbing competitions and excursions. Verya, I have to especially thank you for not giving up on making a proper German out of me. Thank you so much for the endless patients you had teaching me climbing and bringing me up amazing mountains. Your worry free, but very determined, way of life left quite an impression on me. I also will never forget your lessons on being on time.

Ilya and Jacopo, thank you for being such good colleagues and roommates. I will not forget all the delicious pancakes, Borscht, and risotto breakfasts and dinners we shared.

The work atmosphere would have been a very different without Klazina, Ying, Tom van Roij, Tom Kokhuis, Pieter, Muthu, Min, Tianshi, and Rik who made each day more enjoyable with their smiles and upbeat attitudes.

Mieke, Gracia and Rita, thank you so much for helping me with all the administrative paperwork. Gracia, I really appreciated your help to get me back into the 'system' after a glitch in H&R decided to fire me.

Deep, Jason, Reza, Sophinese and Jovana, I am very happy to have shared time with you guys. Thank you for the many dinners and beers that we had together. You are great researchers and you will certainly leave your footprint in the labs reputation and history. Good luck with your PhD's!

Geert and Michiel,thank you very much for the worry free designs and production of any experimental setup I needed. I always loved to come down to the machine shop to brain storm designs and to admire the amazing machinery you have down there. Having such great minds and tools at my disposal is certainly a unique and valuable thing for research, which I absolutely appreciate.

Hans Verdos, thank you for setting up all my Erasmus accounts and for getting me a special keyboard and mouse so quickly when I strained my tendons from too much typing.

I would also like to thank the Biomechanic group. It was a lot of fun during the labuitjes and I learned a lot about mechanics and biology during the presentations. With Lambert and Jelle, I certainly had the most interactions. Thank you for the discussions on mechanical problems.

I would like to thank Dion Koeze, for his work on the fast normalized convolution update scheme and the adaptive reconstruction scheme. I did enjoy a lot our math and philosophy discussions and I wish you all the best in your new path.

I also would like to thank Stefan Klein and Theo van Walsum from the BIGR group for their contribution to my research and fruitful discussions.

I especially want to thank my family for their unconditional love and support in everything I do. Doreen, I could have never asked for a more amazing sister. You made my Undergraduate thesis research possible, you are the most amazing California road trip partner, and you always remind me to enjoy life. Vati, thank you for giving me your brains and love for engineering and letting me pursue anything I wanted to. Without this trust and freedom I would not have come this far. Rebecca, thank you for your constant encouragement, putting up with me and making our incredibly long-distance relationship work. Even thousands of miles apart I could literately feel your love and support. I love you and can not wait to get married to spend the rest of my life with you. Finally, Mutsch, to whom this thesis is dedicated, you give me strength everyday. I love and miss you.

Sponsoring